

Supplementary Information to

Self-Assembly-Assisted Dynamic Placement of Noble Metals Selectively on Multifunctional Carbide Supports for Alkaline Hydrogen Electrocatalysis

Seongbeen Kim,^{a,†} Seung-Jae Shin,^{c,†} Hoyoung Kim,^{a,h,†} Bupmo Kim,^d Namgyu Noh,^e Kug-Seung Lee,^f Jinkyu Park,^a Hyunwoo Jun,^a Jiwon Kim,^a Jaeho Byeon,^a Seonggyu Lee,^g Huawei Huang,^a Sunghyun Noh,^d Han Beom Jeong,^e Jong Hyun Jang,^h Jong Min Yuk,^e Wooyul Kim,^d Hyungjun Kim,^{*b} and Jinwoo Lee^{*a}

^aDepartment of Chemical and Biomolecular Engineering, Korea Advanced Institute of Science and Technology (KAIST), Daejeon 34141, Republic of Korea. E-mail: jwlee1@kaist.ac.kr.

^bSchool of Energy and Chemical Engineering, Ulsan National Institute of Science and Technology (UNIST), Ulsan 44919, Korea

^cCenter for Hydrogen and Fuel Cells, Korea Institute of Science and Technology (KIST); Seoul 02792, Korea

^dDepartment of Energy Engineering, Korea Institute of Energy Technology (KENTECH), Naju 58330, Korea.

^eDepartment of Materials Science and Engineering, Korea Advanced Institute of Science and Technology (KAIST), Daejeon 34141, Korea.

^fPohang Accelerator Laboratory; Pohang 37673, Korea.

^gDepartment of Chemical Engineering/Department of Energy Engineering Convergence, Kumoh National Institute of Technology (KIT), Gumi 39177, Korea.

^hDepartment of Chemistry, Korea Advanced Institute of Science and Technology (KAIST), Daejeon 34141, Republic of Korea. Email: linus16@kaist.ac.kr

† These authors contributed equally to this work.

Correspondence to: linus16@kaist.ac.kr (H.K.); jwlee1@kaist.ac.kr (J.L.)

This PDF file includes:

- Supplementary Notes 1 to 9
- Supplementary Figures 1 to 84
- Supplementary Tables 1 to 17
- Captions for Supplementary Movies 1 to 4
- Supplementary References

Other Supplementary Materials for this manuscript include the following:

- Supplementary Movies 1 to 4

Supplementary Notes

Note S1. Design of heterostructured supports to inhibit NM nanoparticle (NP) sintering.¹

Theoretical calculations suggested that the dominance of the sintering mechanisms above the Tammann temperature T (T_{tam}) is affected by the metal-support interaction (MSI): strong MSI favors the Ostwald mechanism involving the formation and diffusion of metal atoms, while weak MSI favors the particle migration and coalescence (PMC) mechanism.¹

The proposed heterostructured supports consist of two chemical species: one with strong MSI and the other with weak MSI. The surface of heterostructured supports comprises small areas of the first support surrounded by large areas of the second support. NM NPs are selectively loaded and covered onto the first support regions. Above T_{tam} of NM ($T_{\text{tam-NM}}$), the NM NPs on the first support favor the Ostwald mechanism. However, the surface of the first support is unavailable due to NM nanoparticles (NPs) covering all small regions of the first support through strong MSI. In addition, the PMC mechanism is inhibited by the preference of the Ostwald mechanism on the first support with strong MSI. In the surrounding area, the surfaces of the second support remained available for NM NP sintering. However, the second support favors the PMC mechanism, which limits the Ostwald mechanism involving atomic detachment on its surface. In other words, NM NPs on designed heterostructured supports can successfully prevent NM NP from sintering above the $T_{\text{tam-NM}}$.

Note S2. Synthesis approaches for NM atomically dispersed catalysts (ADCs). Kinetic approach and thermodynamic approach for stabilizing the atom-dimension structure of NM ADCs (Fig. S1a).²

The development of a synthesis route for NM ADCs is one of the main challenges because the high surface energy of NM ADCs makes it difficult to retain atom-dimension structures during synthesis or catalysis. Two main directions were applied to prevent the sintering of NM ADCs: a kinetic or a thermodynamic approach. The main difference between them is whether NM ADCs have thermodynamically favorable structures compared to the agglomerated form. When NM agglomerates are thermodynamically favorable, the kinetic approach is applied. First, NM precursors are atomically loaded on the support (for the atomic loading of NM precursors, a low loading of NM is required). Since the sintering of NM species is thermodynamically favorable, it is important not to exceed the activation barrier that enables thermal migration of atomically dispersed NM species. To not exceed the activation barrier, the synthesis conditions (T and the gas atmosphere for thermal treatment) are restricted, or physical barriers are applied. However, the catalysis of NM ADCs under oxidizing or reducing conditions can trigger the exceeding of the activation barrier, which limits catalyst stability by sintering.

On the other hand, the thermodynamic approach is applied when the NM ADCs are thermodynamically more favorable than the agglomerated form. During the thermal decomposition of NM precursors, NM agglomerates form at the beginning. The key difference between the thermodynamic approach and the kinetic approach is the support with a strong

affinity for NM, which stabilizes the atom-dimension structure of NM on the support. Compared to the activation barrier for the sintering of NMs in the kinetic approach, the value of the activation barrier enabling the formation of strong MSI and disintegration of NM NPs is high. Therefore, when the T reaches a certain point (above $T_{\text{tam-NM}}$) that lets it exceed the activation barrier, NM agglomerates spontaneously disintegrate and atomically disperse on the support by forming SMSI. Since the NM ADCs from the thermodynamic approach have a more favorable structure than NM agglomerates, they can feature higher stability than the NM ADCs from the kinetic approach during the catalysis. However, $T_{\text{tam-NM}}$ strongly depends on the size of the NM NPs.¹ Consequently, if the size of the NM NPs exceeds a critical point, the disintegration of large NM agglomerates is inhibited due to the higher activation barrier than the NM NPs. Therefore, the additional strategy to reduce NM NP size and disperse NM NP homogeneously is required to apply the thermodynamic approach.

Note S3. Dynamic placement mechanism. The mechanism for dynamic placement of NM selectively on Mo_xC surfaces involves the PMC mechanism and the Ostwald mechanism.^{1,3}

We chose the T of 1,373 K for the dynamic placement of NM for the following reasons: 1) The NM begins to be mobile for $T_{\text{tam-NM}}$ ($\sim T_m/2$, where T_m denotes the bulk melting point [K]). 2) NM NPs have a lower $T_{\text{tam-NM}}$ than bulk NM,¹ because NM NPs have a lower melting point than bulk NM.⁴

The sintering of NM NPs occurs through the migration of mobile NM species under high T . Two mechanisms have been proposed to explain this phenomenon (Fig. S1b);^{1,3} 1) Entire particles migrate on the support, collide, and coalesce. This mechanism is known as the PMC mechanism. 2) Atomic species separate from smaller particles, diffuse on the support surface and coalesce into larger particles. This mechanism is known as the Ostwald mechanism (atomic migration). Which of the two mechanisms is favored is determined by the free energy of the catalyst system.^{1,3} The Ostwald mechanism is generally preferred when the affinity of the support for NM is sufficiently strong or the energy barrier to atomic detachment is low enough. The properties of the support are considered pivotal factors because they directly affect the free energy of atomic detachment and the diffusion of monomers on the support. In our catalyst system, most of the environmental factors near NM NPs are similar except for the type of support (Mo_xC or carbon surface) where NM NPs are located. Hence, we can conclude that the most critical factor is the MSI between NM and support.

We propose a synthesis mechanism for the dynamic placement of NM selectively on Mo_xC at a sufficiently high T based on different migration behaviors with different types of support (Fig. S1). We would apply theoretical expectation in reverse.¹ The theoretical calculation suggests that the designed heterostructured supports can effectively inhibit NM NP sintering even at T exceeding $T_{\text{tam-NM}}$ (Note S1). This is because the PMC mechanism is inhibited in the first support region with strong MSI, where the NM NPs are loaded, and the Ostwald mechanism is inhibited in the second support region with weak MSI, which surrounds the first support region. In contrast, our objective was to induce the PMC mechanism in the second support region and the Ostwald mechanism in the first support region. This approach aimed to selectively load

NM ADCs onto the first support regions of heterostructured support by elevating T above $T_{\text{tam-NM}}$. At $T > T_{\text{tam-NM}}$, NM NPs in the second support regions would migrate across the support surface via the PMC mechanism, eventually reaching the first support regions. NM NPs in the first support regions would be disintegrated into NM ADCs via the Ostwald mechanism on the support surface. Consequently, NM NPs spontaneously disintegrated, and the NM ADCs selectively loaded in the first support region, which is thermodynamically favorable.

From our experimental design, evaporation-induced self-assembly (EISA) enables the preparation of sufficiently small NM NPs uniformly dispersed on heterostructured $\text{Mo}_x\text{C-C}$ nanocomposite supports.⁵ Prior to the final carburization process at 1,373 K, NM NPs (~5 nm size) were uniformly distributed on mesoporous $\text{Mo}_x\text{C-C}$ nanocomposite. The Mo_xC has a similar or even greater affinity for NM than between NMs, but carbon does not. Thus, NM NPs exhibit different migration behaviors depending on their location on the support. When NM NPs are located on a carbon surface, the weak affinity of carbon for NM makes the PMC mechanism more favorable than the Ostwald mechanism.

Consequently, on carbon the NM NPs migrate via the Brownian motion of whole particles and then reach the Mo_xC surface. When NM NPs are located on the Mo_xC surface, the strong affinity of Mo_xC for NM makes the Ostwald mechanism more favorable than the PMC mechanism. Consequently, atomic species of NM separate from NM NPs, diffuse on the Mo_xC surface, and become trapped on anchoring sites of Mo_xC . To summarize, the PMC mechanism enables the migration of NM NPs from carbon to the Mo_xC surface. Then the Ostwald mechanism enables the disintegration of NM NPs to NM ADCs on the Mo_xC surface. Subsequently, the NM is dynamically and selectively placed on the Mo_xC surface.

Note S4. Synthesis strategy. The method to synthesize aNM/ Mo_xC is assisted by interaction mediator assisted EISA (IM-EISA),⁵ and the design strategy for mesoporous heterostructured $\text{Mo}_x\text{C-C}$ nanocomposite.

To realize the dynamic placement of NM, several requirements should be satisfied: 1) The NM NPs should be small enough that they have sufficiently low $T_{\text{tam-NM}}$ and be homogeneously distributed on support surfaces with sufficient spatial spacing to prevent a further increase in particle size via the PMC mechanism. 2) The density of the anchoring site for NM ADCs should be high enough that numerous NMs can be loaded and retained during the dynamic placement process under high T . 3) The Mo_xC supports with small sizes should be uniformly dispersed on the carbon scaffold to enhance the probability of NM NPs encountering the Mo_xC surface during the PMC mechanism.

To meet these requirements, we designed a synthesis route (Fig. S4) that uses the IM-EISA process to synthesize aNM/ Mo_xC . As the solvent evaporates, microphase separation into hydrophilic and hydrophobic domains occurs to form mesoporous structure throughout the framework. During the IM-EISA process, the molecular interaction between precursors and amphiphilic block copolymer facilitates the homogeneous distribution of metal species on hydrophilic domains by partially offsetting precursor interactions. IM-EISA can sufficiently

reduce the NM particle size and achieve uniform distributions of NM and Mo_xC supports on mesoporous Mo_xC-C nanocomposite, because the hydrophilic domains that are composed of PEO moiety, PF-resin, and MF-resin stabilize the Mo and NM precursor via molecular interactions with the aim to distribute them homogeneously among hydrophilic domains. The first thermal treatment converts the PF resin to a mesoporous carbon scaffold, which the Mo precursor reacts with to form Mo_xC supports. The homogeneously distributed NM precursors are reduced to yield NM NPs with small size of only ~5 nm. Consequently, NM NPs form on both the carbon and Mo_xC surfaces of mesoporous heterostructured Mo_xC-C nanocomposite after the first thermal treatment. The second thermal treatment (air activation) improves the hydrogen evolution activity of Mo_xC.⁵

To obtain a high density of anchoring sites of Mo_xC and prevent further sintering of NM NPs even above $T_{\text{tam-NM}}$, we designed mesoporous heterostructured Mo_xC and carbon nanocomposite supports. A high content (~50 wt%) of Mo_xC supports are uniformly composited using a mesoporous carbon scaffold. Above $T_{\text{tam-NM}}$, the high thermal stability of the carbon scaffold prevents a decrease in anchoring site density on Mo_xC by retaining the mesoporous structure and inhibiting the thermal collapse of the Mo_xC nanostructure. In this way, the Mo_xC supports supply a high specific surface area and numerous defective sites, and the mesoporous carbon scaffold helps to retain the nanostructure of Mo_xC even at a high T of 1,373 K. Furthermore, the mesoporous structure offers sufficient spacing between NM NPs, which serves as a physical barrier. The high content of Mo_xC in the heterostructured supports increases the chance that NM NPs meet the Mo_xC surface before colliding with other NM NPs during the PMC mechanism. Consequently, the sintering of NM NPs via the PMC mechanism is prevented effectively. Overall, by designing heterostructured supports, the Mo_xC-C nanocomposite support can meet all requirements for NM ADCs: high thermal stability, ease of nanostructuring, weak MSI of carbon, favorable *OH binding, high electrochemical stability, high electrical conductivity, and high MSI of Mo_xC.

Note S5. Exclusion of the atom-trapping mechanism and Pt loss on carbon supports. Synthesis route utilizing volatile NM species and support with strong MSI.

Previously, it was reported that NM ADCs can be prepared using atom-trapping. In this approach, supports with strong MSI trap volatile NM species (*e.g.*, NM·O_x, NM·(NH₃)_x) during thermal treatment under specific conditions such as O₂ and NH₃.^{6,7} To confirm that the dynamic placement induces the formation of NM ADCs and not the atom-trapping mechanism, *in situ* transmission electron microscopy (TEM) was conducted in a vacuum during annealing to 1,373 K (final carburization process). During the thermal treatment, two single-crystalline Pt NPs loaded on Mo_xC-C were disappeared (Fig. 1i-k, Fig. S9-10), and Pt ADCs selectively loaded on Mo_xC supports after annealing (Fig. 1g, Fig. S1). Since volatile Pt species cannot form under vacuum due to the absence of gaseous ligands such as CO, NH₃, and O_x, the atom-trapping mechanism can be excluded. Therefore, the dynamic placement of Pt ADCs selectively on Mo_xC supports occurred spontaneously in both inert gas and vacuum atmospheres.

The selective positioning of the NM ADCs on the Mo_xC supports is attributed to the PMC

mechanism for Pt NPs initially present on carbon supports. However, weak Pt-carbon interactions could cause the Pt species on carbon supports to be removed via melting or vaporization during the final carburization process. To exclude this possibility, ICP-MS measurements were conducted on aPt/Mo_xC before and after carburization. If there is a loss of the Pt species on carbon during carburization, the Pt-to-Mo molar ratio would decrease after carburization. During the carburization process in our study, the total sample mass decreased from 1.571 to 1.204 g (**Fig. S7**), primarily because of the decomposition of the oxygenated carbon group or the reduction of the oxygenated metal species by carbon.⁸ This total mass reduction caused the Pt content to increase from 3.942 to 5.071 wt% and the Mo content to increase from 44.05 to 54.56 wt% (**Table S1**). Notably, the Pt-to-Mo molar ratio remained nearly unchanged, with only a slight shift from 5.502 before carburization to 5.715 afterward. Consequently, we were able to multiply the reduction ratio of the total mass during carburization (0.766) by measured contents to calculate the corrected metal contents, which accounted for carbon mass loss. The corrected Pt content after carburization was determined to be 3.884 wt%, which closely matches the initial value of 3.942 wt%. This finding confirms that the Pt content remained intact throughout the process without being lost via melting or vaporization.

Note S6. Dynamic placement of various NM species. The affinity of Mo_xC for NM types determines the atom-dimension structure of NM and whether dynamic placement occurs.

From the theoretical calculation (Fig. 2a-b), Ir, Pd, and Rh, which have similar relative E_b , were expected to undergo dynamic placement during the high- T carburization (1,373 K). However, Ag and Au expected that dynamic placement would be somewhat difficult for them due to their low relative E_b .

To identify the theoretical expectation experimentally, we used EISA to prepare comparison groups with different NM precursors (aNM/Mo_xC, NM: Ag, Au, Pt, Ir, Pd, Rh; and No without NM). N₂ physisorption, small angle X-ray scattering (SAXS), and scanning electron microscopy (SEM) indicate that mesoporous heterostructure developed, regardless of the type of NM precursor (Fig. S15-19). N₂ isotherms for aNM/Mo_xC exhibit type-IV curve and H₁-type hysteresis, which indicates that aNM/Mo_xC has three-dimensional pore networks composed of large mesopores inside the particles (intraparticle pore) and a narrow distribution of pore size.⁹ The peak intensity of SAXS can be changed by many factors, including the beam exposure time and the amount of sample. Peak intensity was normalized to enable the comparison of geometric structure data. These results indicate that mesoporous structures developed for whole particles and they shared similar structural characteristics.¹⁰

In addition, the absence of NM peaks in XRD of aNM/Mo_xC except for aAg/Mo_xC suggests that any crystalline NM was present below the detection limit of XRD except for Ag (Fig. S20). The auto-catalytic effect of NM stabilizes certain phases of Mo_xC according the NM species, so the ratio of α -MoC to β -Mo₂C changes according to the type of NM.¹¹

Note S7. Effects of synthesis conditions to prevent Pt agglomeration. Effects of thermal treatment condition for NM reduction, porous structure of supports, and the presence of Mo_xC supports.

To identify the function of the thermal treatment condition, the porous structure of supports (as a physical barrier), and the presence of Mo_xC supports, Pt precursor was loaded (with similar loading of aPt/ Mo_xC , ~5.2 wt%) onto various supports using IWI (incipient wetness impregnation); commercial carbon (Vulcan XC 72R, CC), mesoporous carbon (mesocellular carbon foam (MSUF-C), MC), and mesoporous heterostructured Mo_xC -C (aNo/ Mo_xC). Two thermal treatments were used: 1) Thermal reduction under 10v/v% of H_2/Ar with low- T (373 K, the kinetic approach), which is indicated by appending H_2 . 2) Thermal treatment under Ar with high- T carburization (1,373 K, the thermodynamic approach), which is indicated by appending Ar .

N_2 physisorption, SAXS, and SEM reveal that thermal treatment conditions did not affect the structural characteristics of the supports (Fig. S27-31). STEM revealed the presence of large Pt agglomerates for samples prepared by IWI (Pt/CC H_2 , Pt/CC Ar , Pt/MC H_2 , and Pt/MC Ar), which indicates that IWI cannot achieve uniform loading of Pt precursor on supports (Fig. S32-33). STEM and XRD results suggest that porosity and low- T reduction alleviate the thermal sintering of Pt (Fig. S32-34). However, carbon supports have weak MSI for Pt, so the atom-dimension structure of Pt is difficult to retain, and dynamic placement of Pt cannot occur.

Furthermore, SEM and STEM images of Pt/CC H_2 , Pt/CC Ar , Pt/MC H_2 , and Pt/MC Ar (Fig. S30-33) revealed several large Pt agglomerates, which were not observed in similar images of PtNP/ Mo_xC -C (Fig. S5). This difference indicates that IM-EISA is more beneficial than IWI for uniform loading of Pt species on supports, because Pt precursors are selectively incorporated and homogeneously distributed by molecular interaction with PEO-b-PS, which offsets precursor interactions. In contrast, IWI cannot adequately mitigate precursor interactions, which leads to the formation of large Pt agglomerations. In addition, carbon supports have low MSI and only a low density of anchoring sites that have adequate affinity for Pt. Therefore, carbon supports do not have sufficient capacity to disperse high loading (~5 wt%) of Pt species. During low- T reduction, Pt agglomerates show an irregular morphology with similar crystallite size regardless of porosity, and Pt with atom-dimension structure (single-atom Pt: red circle, Pt atomic cluster: orange circle) was plentiful (Fig. S32, S34). This result means that the low- T process kinetically impedes thermal migration or crystallization of Pt species, thereby helping to maintain the atom-dimension structure of Pt. In contrast, high- T carburization (1,373 K) promotes thermal migration or crystallization of Pt species, so Pt with atom-dimension structure disappears and Pt agglomerates grow to form spherical crystallites (Fig. S33-34). Compared with Pt of Pt/CC Ar , Pt of Pt/MC Ar has more and smaller NPs (< ~5 nm) in STEM images and features a smaller average crystallite size (Fig. S33-34); these differences confirm that porosity functions as a physical barrier that can prevent thermal sintering of Pt.

Note S8. Change of geometric structure of NM during dynamic placement. The dynamic placement constructs the distinct structures (interfacial active systems) between NM ADCs and Mo_xC supports, which are distinguished from other NM ADCs on carbon- or oxide-based supports.

The X-ray absorption near-edge structure (XANES) of aNM/ Mo_xC is distinct from those of NM foil or NM oxide. These differences imply that NM ADCs have different coordination environments with them (Fig. 3c, Fig. S51).¹² In the XANES region, aNM/ Mo_xC exhibited a white line intensity (for the L_3 -edge) or edge shift (for the K-edge) similar to those of the NM foil, indicating that the NM ADCs possessed metallic characteristics (Figs. 3c-d, Fig. S51). These metallic characteristics were attributed to the electronic MSIs between the NM ADCs and the metallic Mo_xC supports. Similarly, the white line intensity of both Pt/ Mo_xC _H₂ and Pt/ Mo_xC _Ar was comparable to that of the NM foil, implying that the average oxidation state of Pt species in these samples was metallic (Fig. S51). These results suggest that the observed metallic characteristics were likely due to either the electronic MSI between the Pt species and Mo_xC supports or the presence of large Pt agglomerates (owing to their higher proportion of internal Pt atoms relative to surface Pt atoms).

The Pt 4f XPS spectra of Pt/ Mo_xC _Ar also revealed metallic characteristics, which is consistent with the XANES results (Fig. 3b). However, the Pt 4f XPS data for Pt/ Mo_xC _H₂ indicated cationic characteristics, which does not align with the metallic features observed in the XANES results (Fig. 3b). STEM imaging of Pt/ Mo_xC _H₂ revealed that Pt species were present as atomically dispersed catalysts, sub-nano clusters, or large agglomerates (Fig. S36). Additionally, the low-*T* reduction (373 K) was insufficient to induce an electronic MSI between the Pt species and supports, leading to cationic characteristics for the Pt ADCs or Pt nanoclusters in Pt/ Mo_xC _H₂, which is consistent with previous findings for single-atom Pt catalysts.^{13,14} Furthermore, the low-*T* reduction resulted in low crystallinity and incomplete ligand removal (Table S6), which contributed to the cationic characteristics of the surfaces of the large Pt agglomerates. In conclusion, the oxidation state and EXAFS fitting results (Tables S5-6) for both Pt/ Mo_xC _H₂ and Pt/ Mo_xC _Ar confirmed the presence of large Pt agglomerates, which were absent in aNM/ Mo_xC .

Fourier transforms of extended X-ray absorption fine structure (FT-EXAFS) with corresponding fitting results and wavelet transform of EXAFS (WT-EXAFS) suggest the change of structural parameters of samples, which explains the synthesis mechanism and differences from the synthesis strategy (EISA vs. IWI). Before final carburization (Fig. 3g, Table S6), Pt/ Mo_xC -C at 873 K, Pt/ Mo_xC -C at 1,123 K, and Pt/ Mo_xC -C at 403 K (Pt/ Mo_xC -Cs) has ~8 of Pt-Pt coordination, but after final carburization aPt/ Mo_xC has no Pt-Pt coordination with ~1 Pt-Mo coordination. This indicates that Pt NPs were disintegrated into Pt ADCs, and Pt ADCs were selectively loaded on Mo species (Mo_xC supports) after the final carburization. In addition, the bond length of Pt-sMo was changed during the final carburization from ~2.72 Å (Pt/ Mo_xC -Cs) to ~2.84 Å (aPt/ Mo_xC). Based on Vegard's law, the Pt species in Pt/ Mo_xC -C were likely in an alloy form with dilute Mo content, as evidenced by the bond lengths of Pt-Pt (~2.70 Å) and Pt-Mo (~2.72 Å) being comparable to the Pt-Pt bond length in bulk Pt (~2.76 Å).^{15,16} However, the bond length of Pt-Mo (~2.84 Å) in aPt/ Mo_xC

showed a large difference compared to those in Pt/Mo_xC-Cs, indicating that Pt species in aPt/Mo_xC were not alloyed with Mo species but forms Pt ADCs on Mo_xC supports. In addition, samples obtained by IWI showed ~6 Pt-Pt coordination, indicating the inevitable formation of large Pt agglomerates. This result indicates that IWI is insufficient for mitigating precursor interaction which is necessary for homogeneous loading of NM precursor onto supports.

Unlike aPt/Mo_xC, Pt/Mo_xC_Ar exhibited a prominent second-shell magnitude in its FT-EXAFS graph, whereas Pt/Mo_xC_H₂ exhibited a similar magnitude to that of aPt/Mo_xC (**Figs. S52a, e, f**). To further elucidate the coordination environment, EXAFS fitting was performed. Specifically, aPt/Mo_xC was observed to have no Pt-Pt coordination. However, the IWI-prepared samples had Pt-Pt coordination numbers of 6, that is, 6.14 for Pt/Mo_xC_H₂ and 6.35 for Pt/Mo_xC_Ar (**Table S6**). These results confirm that molecular interactions between the block copolymers and NM precursors effectively mitigated the interaction between the NM precursors, leading to atomically dispersed Pt after high-*T* annealing. In contrast, the absence of such interaction mitigation in the IWI-prepared samples resulted in the formation of large NM agglomerates.

Since WT-EXAFS can distinguish the *k*-dependence of EXAFS (WT-EXAFS can distinguish the relative atomic number *Z* value by *k* resolution), it is effective to distinguish the *Z* of the coordinating atom at a similar distance *R*.¹⁷ WT-EXAFS of Pt, PtO₂, Pt/Mo_xC-Cs, and Pt/Mo_xC_H₂ has an intensity maximum in the *k* region 8.5 to 9.5 Å, but that of aPt/Mo_xC has an intensity maximum at *k* of ~7.7 Å (Fig. 3i-j). These results suggest differences of coordinating atoms in the second shell: Pt-Pt for Pt, PtO₂, Pt/Mo_xC-Cs, and Pt/Mo_xC_H₂; Pt-Mo for aPt/Mo_xC. For Pt/Mo_xC_Ar, its WT-EXAFS has an intensity maximum at *k* of ~8.2 Å due to the coexistence of Pt-Pt (~6.35 coordination number) and Pt-Mo (~1.82 coordination number) (Table S6). These results indicated that the coordinating atoms (Mo) of Pt in aPt/Mo_xC have lower *Z* values than those (Pt) of others in the second shell of FT-EXAFS.

The WT-EXAFS of PtO₂, Pt/Mo_xC-Cs, and Pt/Mo_xC_Ar show an intensity maximum in the *k* region 5.5 to 6 Å, but that of aPt/Mo_xC has an intensity maximum at *k* of ~5.2 Å (Fig. 3i-j). These results imply that coordinating atoms of Pt in aPt/Mo_xC have a lower *Z* value than others (O) in the first shell of FT-EXAFS. The presence of Pt-O coordination in Pt/Mo_xC-Cs and Pt/Mo_xC_Ar originated from the surficial Pt-O coordination for Pt NPs. Distinguishing the coordinating atom of the first shell in FT-EXAFS is somewhat difficult due to the limited resolution of *Z* in EXAFS fitting ($Z \approx \pm 2$).¹⁷ The imaginary part of FT-EXAFS is highly sensitive to coordinating environments (type of neighboring atoms, bond lengths, *etc.*), so it can supply information about changes in coordinating environments.^{18,19} The imaginary part of aPt/Mo_xC at the first shell of FT-EXAFS showed differences from that of others, indicating that there existed differences for coordinating environment (Fig. S53-55). The EXAFS fitting shows that Pt in aPt/Mo_xC was stabilized by ~3 of Pt-C coordination with a bond length of ~2.11 Å, which was quite longer than that (~1.95 Å) of the Pt-O coordination of Pt NPs (Pt/Mo_xC-Cs and Pt/Mo_xC_Ar) (Fig. 3h, Table S6). Compared to others, aPt/Mo_xC has large differences in bond length from EXAFS fitting and maximum intensity from WT-EXAFS. These suggested that the coordinating atom has a lower *Z* value than O, indicating that the coordinating atom might be C. The WT-EXAFS of Pt/Mo_xC_H₂ has intensity maximum at *k* of

~6.4 Å, which has higher value than that of Pt/Mo_xC-C, indicating that the coordinating atom of Pt/Mo_xC-H₂ has a higher *Z* value than O (Fig. 3j). The EXAFS fitting results indicates that ~1.73 Pt-Cl coordination with bond length of ~2.31 Å contributes to this intensity maximum (Table S6). The presence of Pt-Cl coordination resulted from the incomplete removal of the Cl ligand of Pt precursor (H₂PtCl₆) by the low-*T* reduction under 10v/v% H₂/Ar at 373 K (kinetic approach) which was generally employed for the preparation of Pt ADCs.^{20,21}

Note S9. Alkaline hydrogen oxidation reaction (HOR) activity and CO tolerance. Samples obtained by dynamic placement exhibited increased kinetics and CO tolerance in alkaline HOR due to the advantages of an intimate interfacial active system between NM ADCs and Mo_xC supports. According to studies on AEMFCs, a 1 M KOH electrolyte better reflects the actual OH⁻ concentration (1-2 M) typically encountered in AEMFCs.²²⁻²⁴ For the same reason, several durability tests for AEMs have been conducted using high OH⁻ concentrations.²⁴⁻²⁶ The effect of Mo_xC supports on adjusting the interfacial water structure for reversible HER and HOR should also be evaluated under identical electrolyte conditions. Therefore, the HOR experiments were initially conducted in 1 M KOH.

The alkaline HOR activity of samples obtained via dynamic placement (aPt/Mo_xC, aRh/Mo_xC, and Pt/Mo_xC-Ar) surpassed those of commercial Pt/C, and Pt/Mo_xC-H₂ obtained by kinetic approaches (Fig. 4e, Fig. S70, Table S11). In addition, they reliably retained the current density until 0.4 V without oxidative degradation. To assess the kinetics of alkaline HOR, exchange current density *j*₀ and kinetic current density at 25 mV (*j*_{k at 25 mV}) per NM moles (molar kinetic activity) were calculated (Fig. 4f, Fig. S71-72, Table S11). aNM/Mo_xC had 2-fold higher *j*₀ and 5-fold higher molar kinetic activity than those of Pt/C and Pt/Mo_xC-H₂. Also, the molar kinetic activity of Pt/Mo_xC-Ar was about twice that of Pt/C and Pt/Mo_xC-H₂, due to interfacial active systems between Pt ADCs and Mo_xC supports through dynamic placement. However, the efficiency for NM utilization is lower than that of aPt/Mo_xC because large Pt agglomerates formed by IWI cannot be disintegrated into Pt ADCs to form interfacial active systems. These results indicate that the intimate interfacial active system optimizes the absorbate *E*_b by electronic MSI to improve the alkaline hydrogen adsorption-desorption kinetics. In addition, the intimate interfacial active system can place a favorable *OH binding site of Mo_xC adjacent to NM ADCs to enhance the alkaline HOR kinetics by optimizing the interfacial water structure.

To demonstrate the superiority of the catalysts obtained via dynamic placement, HOR tests were also performed under the conventional condition of 0.1 M KOH. Notably, aPt/Mo_xC had 2.0-fold higher *j*₀ and 3.3-fold higher *j*_{k at 25 mV} per NM moles compared to commercial Pt/C (Fig. S73, Table S12). These results confirm that Mo_xC supports improve the alkaline HOR kinetics even under dilute 0.1 M KOH conditions.

To demonstrate that the superior activity of aPt/Mo_xC is attributable to its design strategy rather than its reduced NM loading, we conducted additional alkaline HER and HOR tests on Pt/C with the same Pt loading (31 μg cm⁻²) as aPt/Mo_xC. The results revealed that aPt/Mo_xC exhibited better performance than Pt/C, even with the same Pt loading. In the alkaline HER, aPt/Mo_xC demonstrated 1.4-fold higher *j*₀ and 5.2-fold higher *j*_{at 40 mV} per NM moles than Pt/C

(Table S10, Figs. S74 a, b). In the alkaline HOR in 1 M KOH, aPt/Mo_xC demonstrated 1.7-fold higher j_0 and 4.5-fold higher j_k at 25 mV per NM moles than Pt/C (Table S11, Figs. S74 c, d). In the alkaline HOR in 0.1 M KOH, aPt/Mo_xC demonstrated 1.8-fold higher j_0 and 3.5-fold higher j_k at 25 mV per NM moles than Pt/C (Fig. S73, Table S12). These results confirm that the enhanced catalytic performance of aPt/Mo_xC stems from its design strategy rather than its Pt loading.

Electrochemical characterization was performed in 1,000 ppm CO/H₂-purged 1 M KOH to assess the CO tolerance in alkaline HOR. At an overpotential of 100 mV, aPt/Mo_xC (14.0 %) and Pt/Mo_xC_Ar (15.3 %) have a slight decrease of j in the presence of CO than Pt/C (29.8 %) or Pt/Mo_xC_H₂ (47.8 %). Surprisingly, aRh/Mo_xC (1.6 %) rarely suffered from CO poisoning (Fig. 4g-h, Fig. S75). In addition, samples prepared by dynamic placement had higher j_0 and j_k at 25 mV compared with Pt/C and Pt/Mo_xC_H₂ (Fig. S76). To assess the kinetics of CO removal, we performed CO stripping. However, aNM/Mo_xC showed no CO stripping j , possibly because *CO binding is too weak (Fig. S66). *In situ* ATR-SEIRAS results supported that this is because the absence of strongly adsorbed CO on NM ADCs, which is different with Pt/C (Fig. S82).

Therefore, we performed electrochemical CO oxidation with CO purged 1 M KOH (Fig. S77). To enable ideal electrochemical CO oxidation, two requirements must be met: 1) appropriate strength of *CO binding (neither too strong nor too weak, Sabatier's principle). 2) easy OH_x supply to *CO binding site.^{27,28} Samples obtained by dynamic placement had superior CO oxidation kinetics compared with Pt/C and Pt/Mo_xC_H₂, and CO oxidation efficiency decreased with a similar trend of CO tolerance. aNM/Mo_xC has lower onset potential than both Pt/C and Pt/Mo_xC_H₂ (Fig. S77b). Pt/C suffers from CO poisoning due to the strong *CO binding. Therefore, a decrease in onset potential for aNM/Mo_xC implies a weakening of the CO adsorption as a consequence of the alteration in the geometric and electronic structure of NM by dynamic placement (Fig. S66). In addition, a fast increase of current density indicates a fast reaction kinetics, as a consequence of easy *OH supply to NM sites where *CO is located. Samples with an intimate interfacial active system between NM and Mo_xC exhibit a faster increase in current density than NM on carbon. *OH binding is more appropriate with Mo_xC supports than carbon so that Mo_xC supports can supply *OH species more easily than the carbon support can. This indicates that increased CO oxidation kinetics improves the CO tolerance of aNM/Mo_xC through easier removal of CO on NM sites. For chronoamperometry at 100 mV (Fig. S78a), samples prepared by dynamic placement showed better stability than Pt/C and Pt/Mo_xC_H₂. With the presence of CO (Fig. S78b), samples obtained by dynamic placement are more stable than Pt/C and Pt/Mo_xC_H₂. These results indicate that dynamic placement constructed an intimate interfacial active system between NM ADCs and Mo_xC supports, so the strong MSI and high CO tolerance together increase the long-term stability of NM even in the presence of CO.

Supplementary Figures

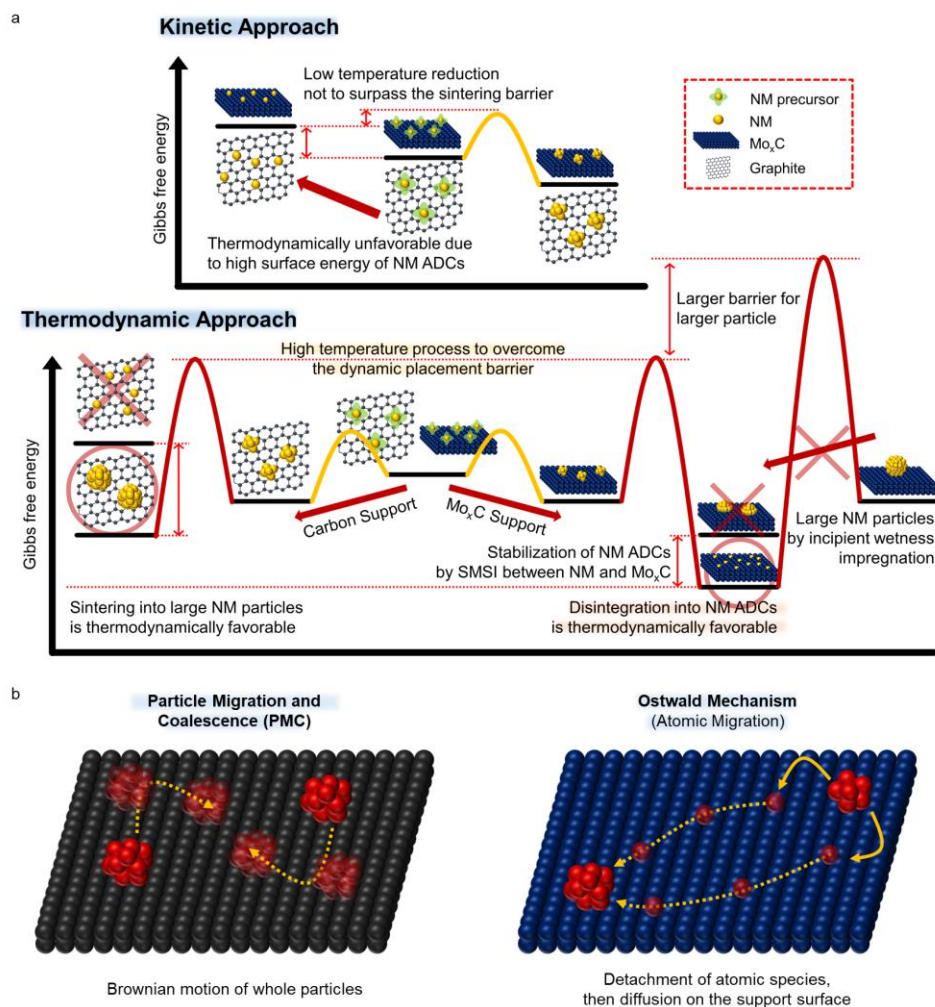


Fig. S1 Synthesis strategy and mechanism. (a) Kinetic approach and thermodynamic approach in synthesis strategy. (b) PMC mechanism and Ostwald mechanism to sinter NM NPs. (c) Strategy to synthesize aNM/Mo_xC by using IM-EISA and dynamic placement of NM selectively on Mo_xC surface.

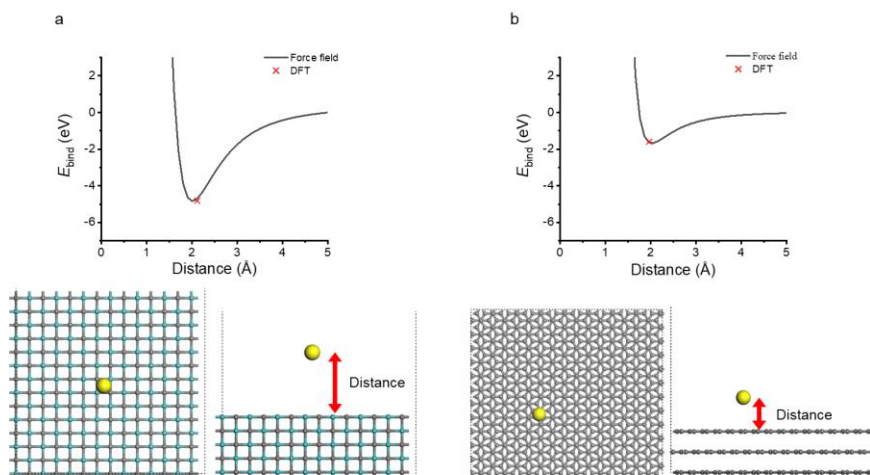


Fig. S2 Theoretical models for binding energy of Pt on support. (a) The binding energy (E_{bind}) of Pt on **a**, α -MoC (100) and (b) graphite. E_{bind} is shown with respect to the distance. The FF parameters for the Lennard-Jones pairwise potential were set to reproduce the optimal binding energy and at a position comparable to the DFT value.

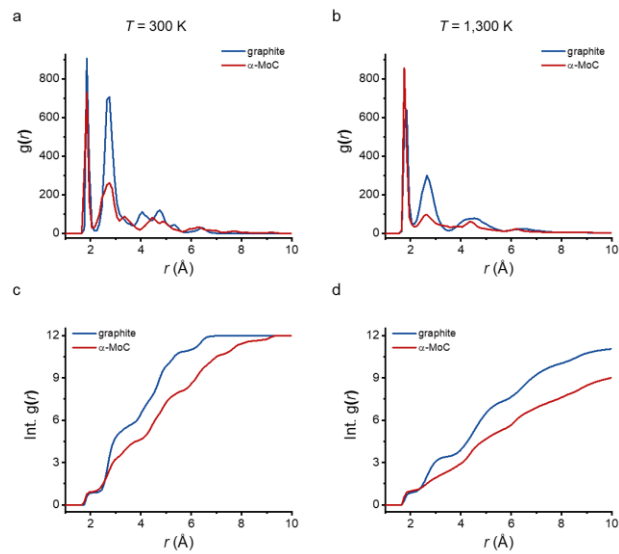


Fig. S3 Radial distribution for Pt-Pt. Pt-Pt radial distribution function, $g(r)$ and its integrated (Int.) value, $\int_0^r 4\pi r'^2 g(r') dr'$, for the distance r between Pt atoms of the cluster (a) at 300 and (b) 1,300 K for the graphite support (blue) and $\alpha\text{-MoC}$ (100) support (red). The coordination number is read at $r = 3.05 \text{ \AA}$.

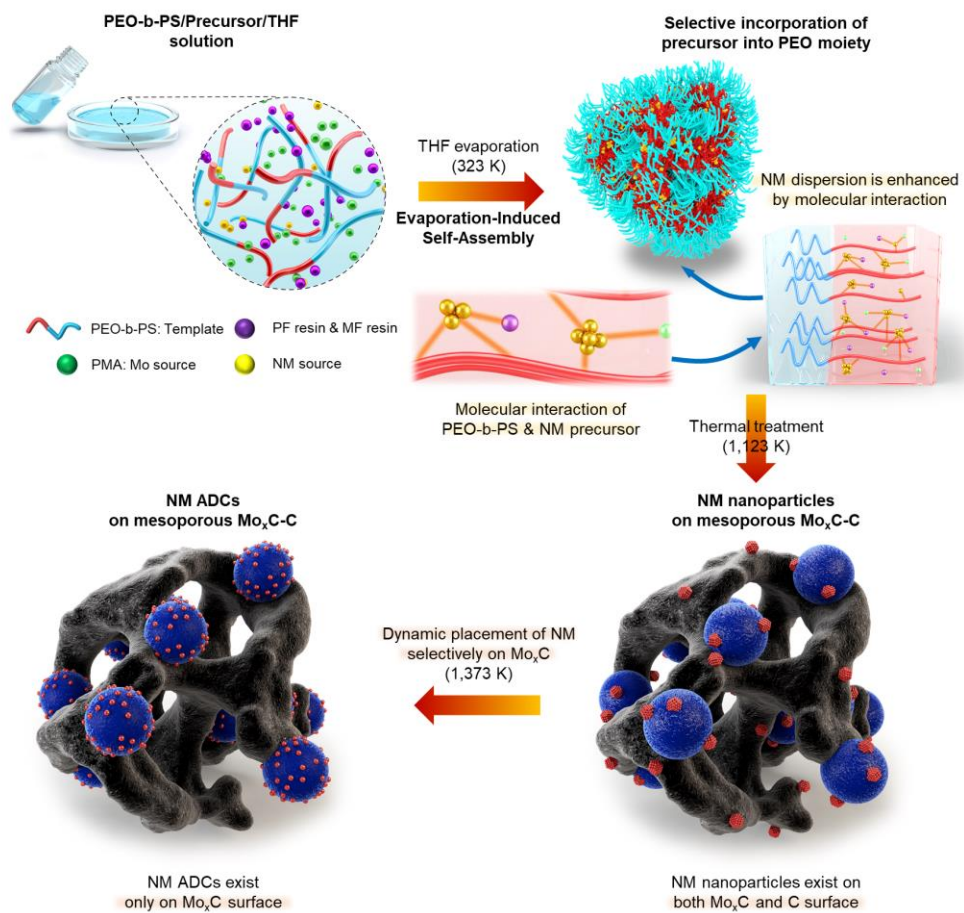


Fig. S4 Self-assembly-assisted dynamic placement. (a) Strategy to synthesize aNM/ Mo_xC by using IM-EISA and dynamic placement of NM selectively on Mo_xC surface.

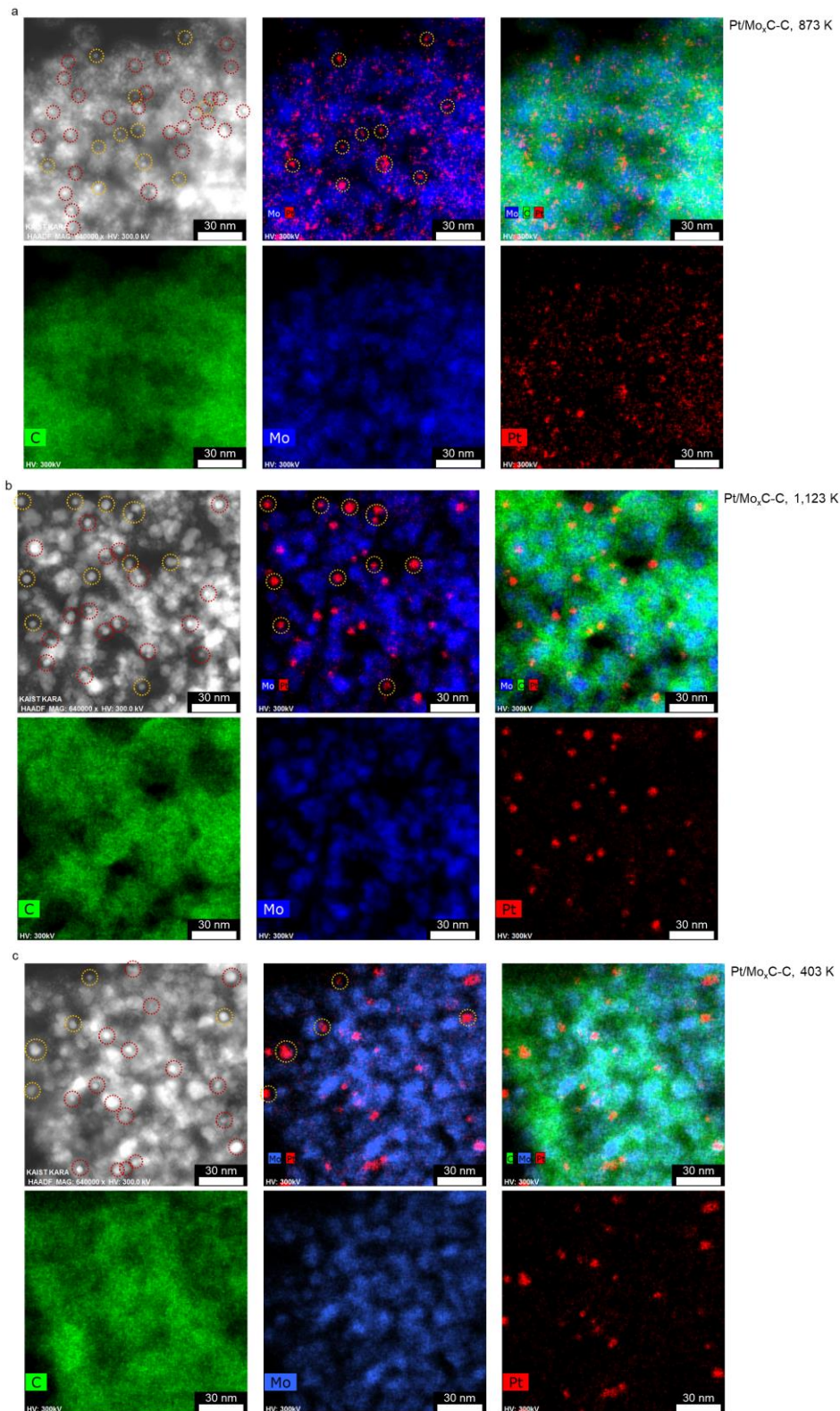


Fig. S5 STEM analysis of Pt/Mo_xC-C for each thermal treatment step. HAADF-STEM images and EDS mappings of Pt/Mo_xC-C during synthesis for the first thermal treatment under Ar (a) at 873 K and (b) at 1,123 K, and for air activation under O₂/Ar (c) at 403 K (red: Pt, blue: Mo, green: C). Orange circles: Pt NPs on carbon, red circles: Pt NPs on Mo_xC [overlapped with Mo EDS mapping].

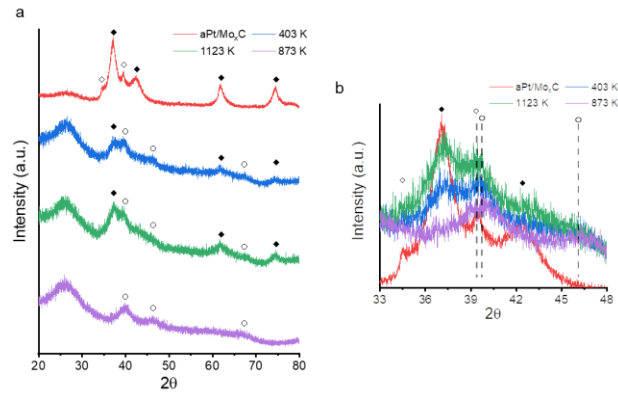


Fig. S6 XRD analysis of Pt/Mo_xC-C for each thermal treatment step. (a) XRD patterns for Pt/Mo_xC-C during synthesis for first thermal treatment under Ar at 873 K (violet) and 1,123 K (green), and for air activation under O₂/Ar at 403 K (blue), and for final carburization under Ar at 1,373 K (red) resulting in the synthesis of aPt/Mo_xC. (b) Enlarged XRD patterns to distinguish the crystalline Pt species. (◆: α-MoC [JCPDS 01-089-2868], ◇: β-Mo₂C [JCPDS 00-011-0608], ○: Pt [JCPDS 04-0802])

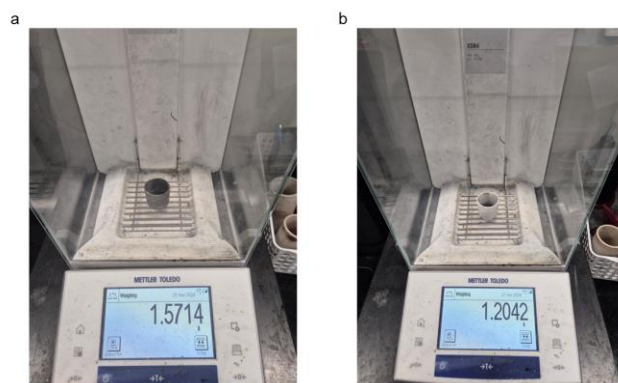


Fig. S7 Change in total mass before and after final carburization. Optical photographs of (a) Pt/Mo_xC-C at 403 K and (b) aPt/Mo_xC.



Fig. S8 Gram-scale synthesis of aPt/Mo_xC. The optical photograph for the gram-scale production of aPt/Mo_xC.

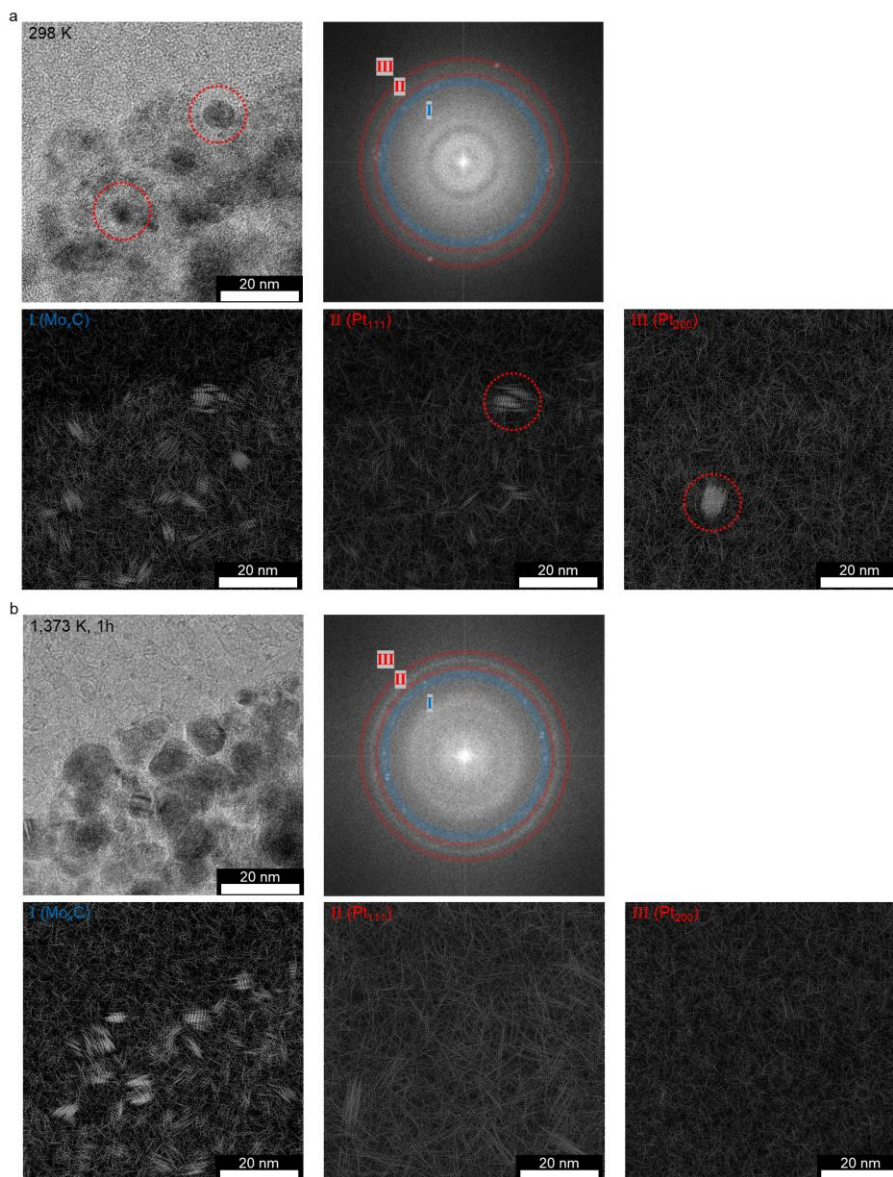


Fig. S9 *In situ* TEM analysis at 298 and 1,373 K with fixed T . *In situ* TEM results, corresponding HR-TEM images, FFT pattern, and inverse FFT images at (a) 298 K and (b) 1,373 K with retaining T (Red circles: crystalline Pt). In the FFT pattern, red: Pt, blue: α -MoC & β -Mo₂C. Bandwidth for inverse FFT: I - Mo_xC: 2.50 – 2.28 Å (α -MoC & β -Mo₂C), II - Pt₁₁₁: 2.28 – 2.20 Å, III - Pt₂₀₀: 2.00 – 1.90 Å]. Scale bar: 20 nm.

Inverse FFT images showed the position of crystalline species with selected lattice spacing. Area I (blue) includes the (111) plane of crystalline α -MoC, and the (101) and (002) planes of crystalline β -Mo₂C. Area II (red) includes the (111) plane of crystalline Pt, and Area III (red) includes the (200) plane of crystalline Pt. The Pt NPs on the right include both crystalline Mo_xC and Pt; this observation indicates that Pt might be placed on Mo_xC. However, the Pt NPs on the left side, include only crystalline Pt; this observation indicates that Pt might be placed on carbon. At 1,373 K, no inverse FFT patterns of Pt were observed; this result indicates that final carburization eliminated crystalline Pt.

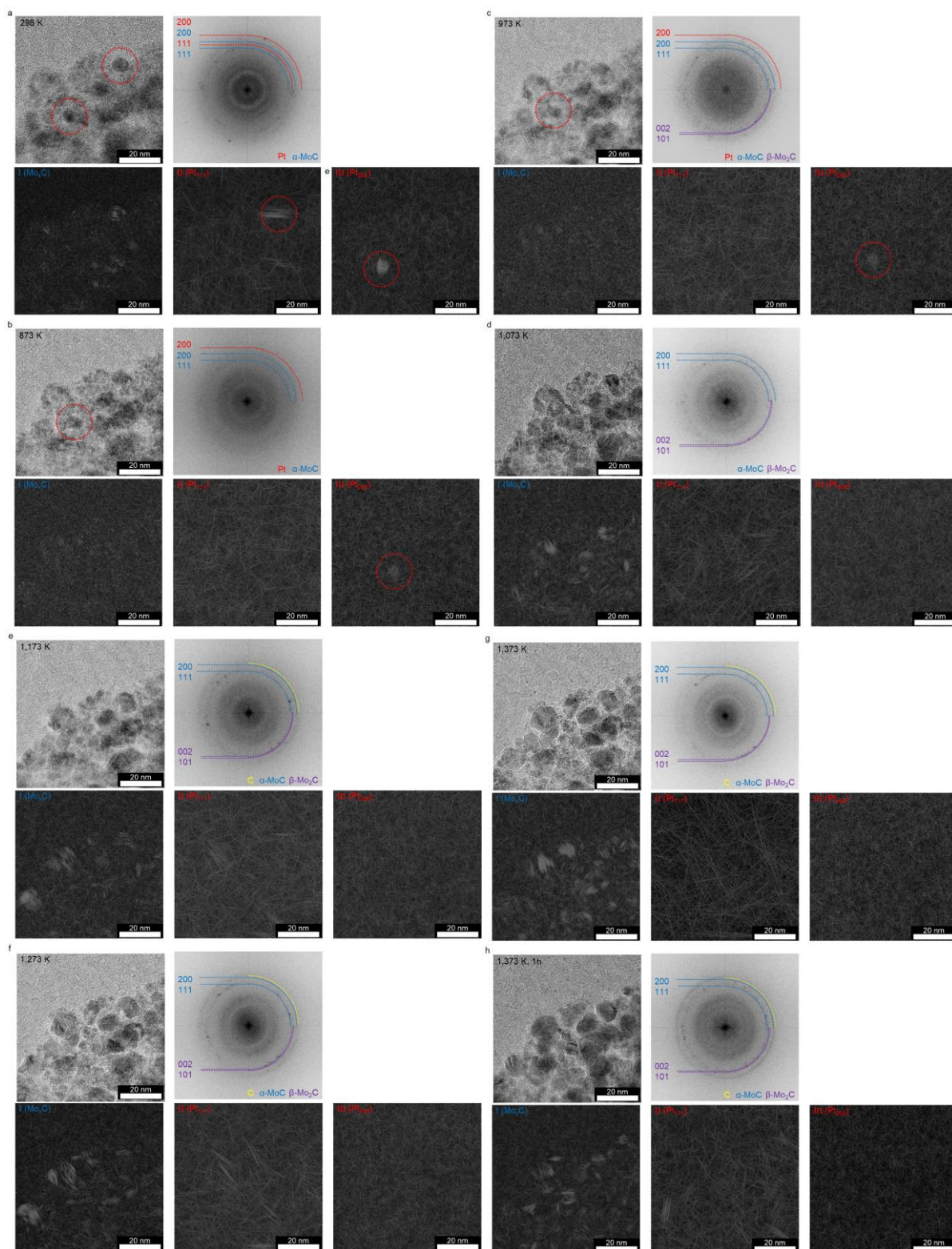


Fig. S10 *In situ* TEM analysis with increasing T under vacuum. *In situ* TEM results, corresponding HR-TEM images, FFT pattern, and inverse FFT images at (a) 298 K, (b) 873 K, (c) 973 K, (d) 1,073 K, (e) 1,173 K, (f) 1,273 K, (g) 1,373 K, and (h) 1,373 K after 1hr, with increasing T from 298 to 1,373 K during the final carburization process. Red circles: crystalline Pt. In FFT pattern, red: Pt, blue: α -MoC, purple: β -Mo₂C, and yellow: carbon. Bandwidth for inverse FFT: [I - Mo_xC: 2.50 – 2.28 Å (α -MoC & β -Mo₂C), II - Pt₁₁₁: 2.28 – 2.20 Å, III - Pt₂₀₀: 2.00 – 1.90 Å]. Scale bar: 20 nm.

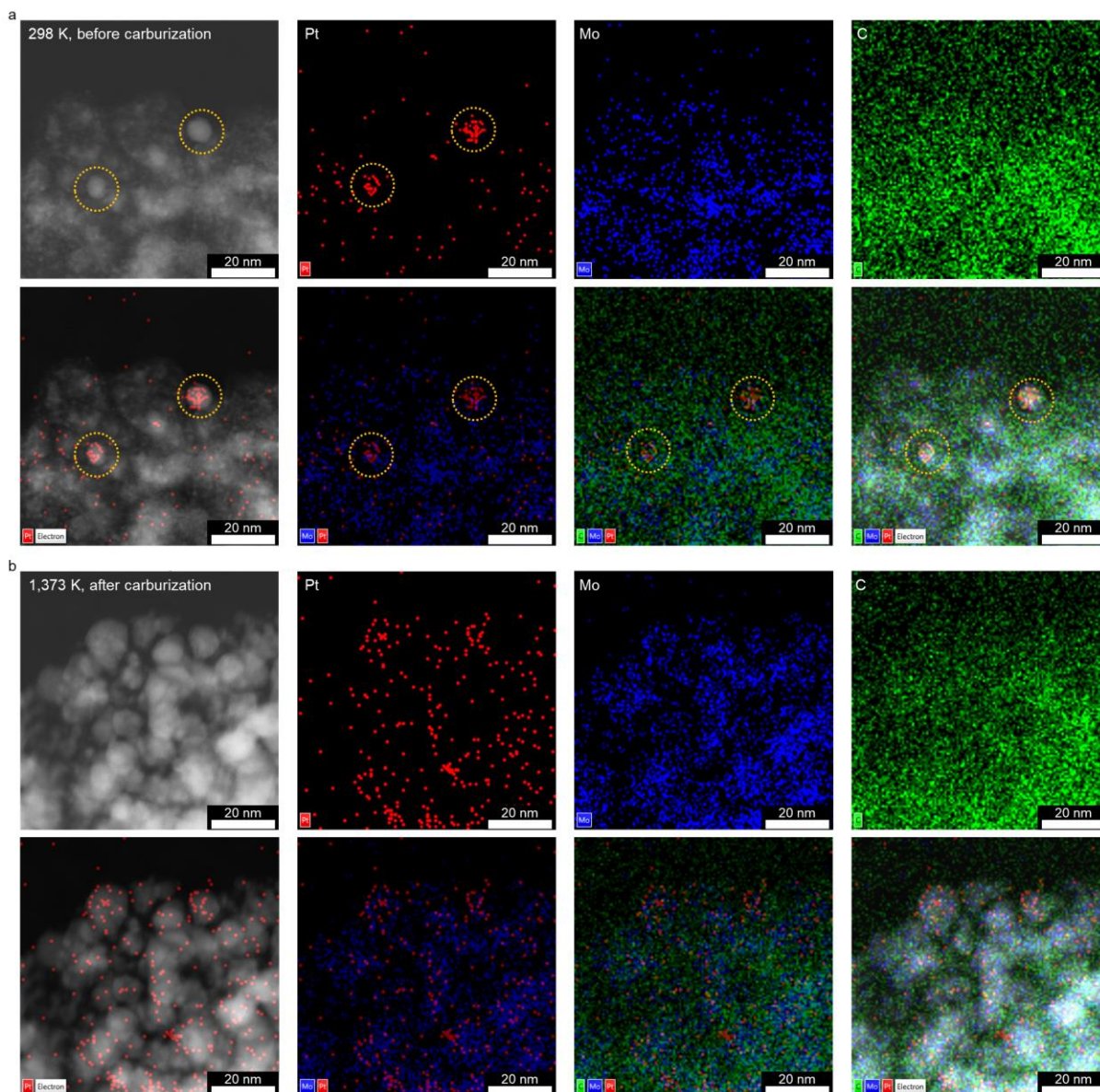


Fig. S11 STEM analysis at identical position before and after annealing under vacuum. STEM images and corresponding EDS mappings (a) before (298 K) and (b) after (1,373 K) annealing at identical position (Red: Pt, Green: Mo, Blue: C, Orange circle: crystalline Pt species).

At 298 K, for Pt NPs on the right side, the EDS signals of Mo overlapped those of Pt; this result indicates that Pt was placed on Mo_xC , but for Pt NPs on the left, only the EDS signal for Pt existed; this result indicates that Pt was placed on carbon. At 1,373 K, no Pt agglomerates were observed, but the EDS signal of Pt was homogeneously and selectively overlapped on Mo EDS signal; this result indicates selective dynamic placement of Pt ADCs on Mo_xC supports.

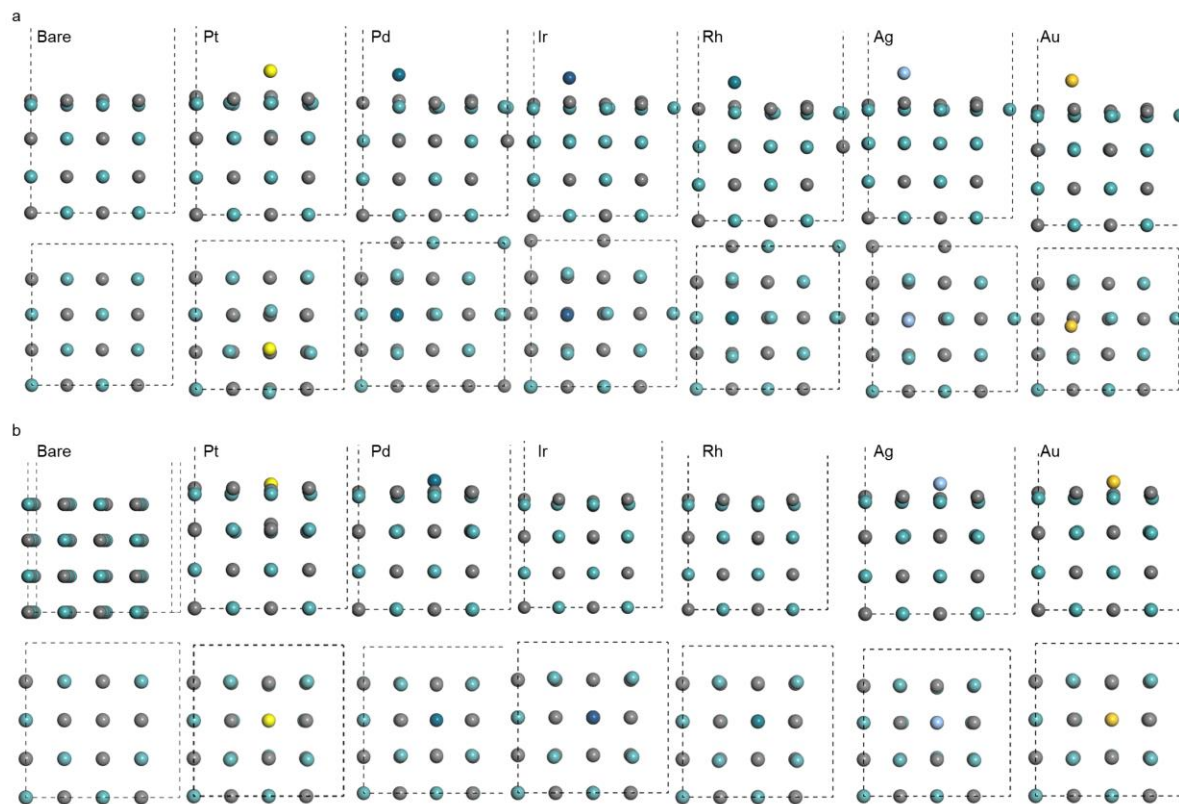


Fig. S12 DFT models for binding energy of NM on α -MoC (100). DFT models for calculating the binding energy of NM on α -MoC (100) (a) without and (b) with Mo-vacancy.

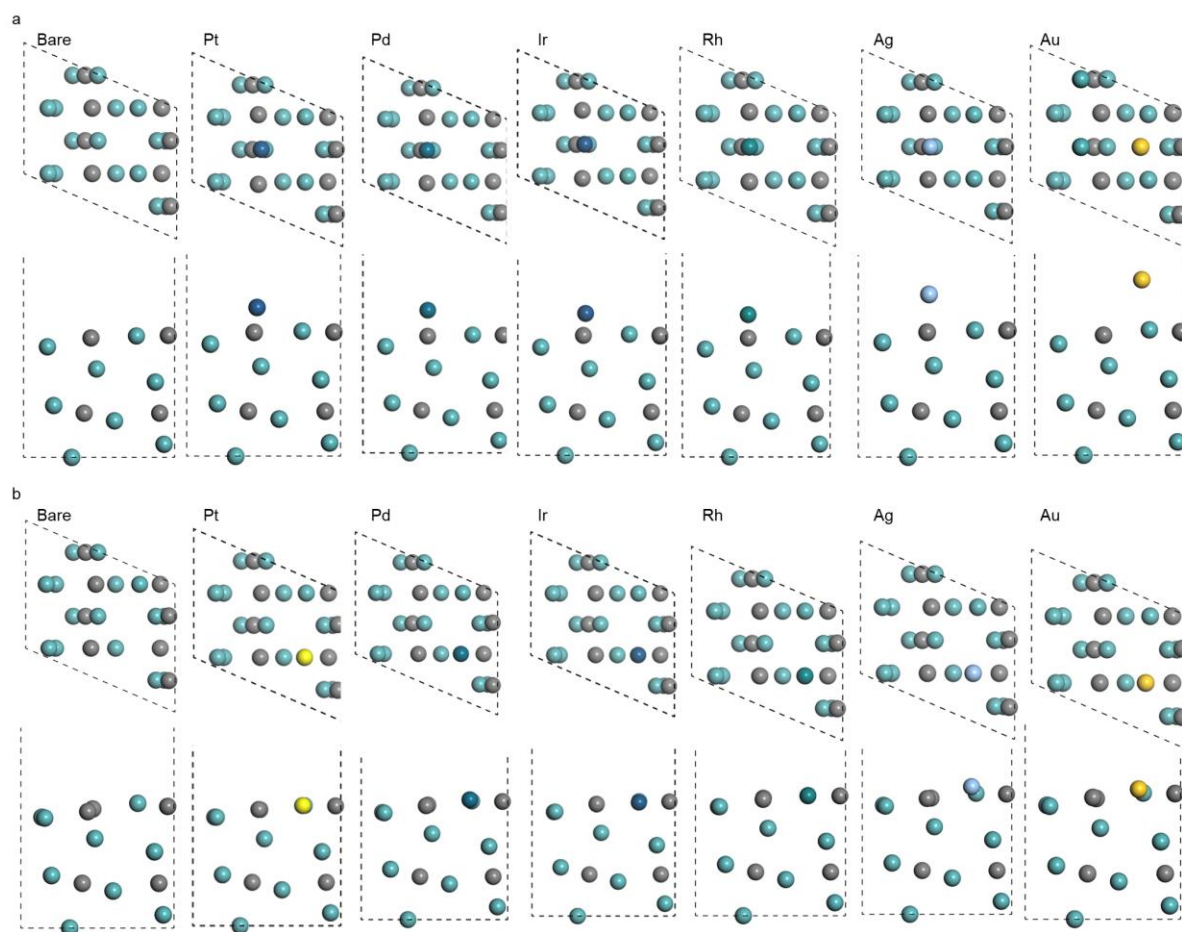


Fig. S13 DFT models for binding energy of NM on β -Mo₂C. DFT models for calculating the binding energy of NM on β -Mo₂C (101) (a) without and (b) with Mo-vacancy.

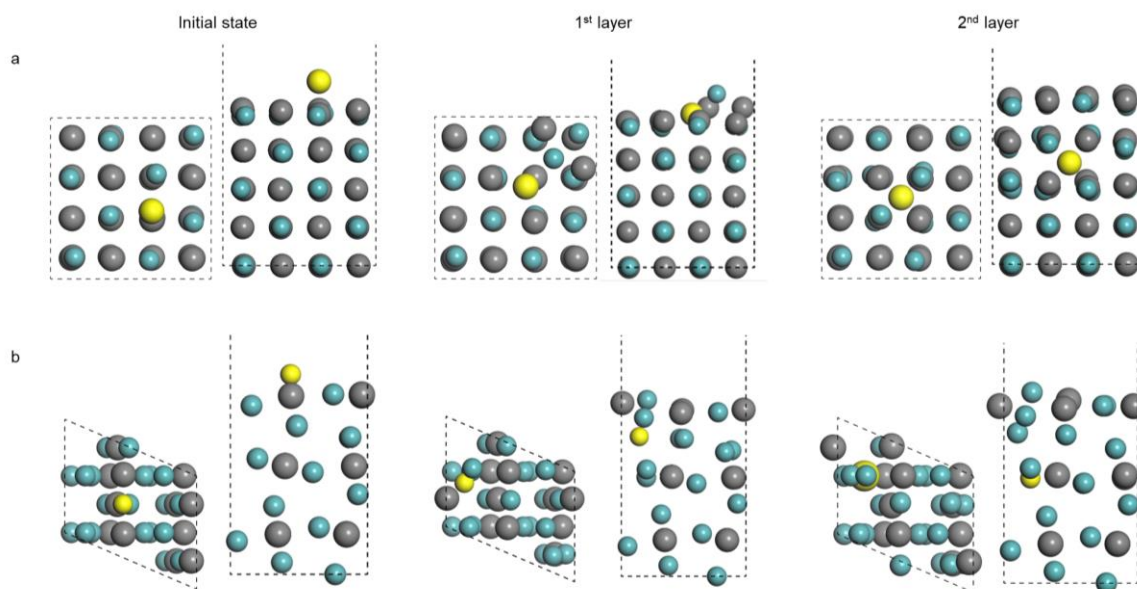


Fig. S14 DFT models for the diffusion barrier. DFT models for calculating the diffusion barrier of Pt from topmost surface into bottom layers; (a) α -MoC (001) and (b) β -Mo₂C (101) cases. Other models for calculating the diffusion barrier of NMs (Pd, Rh, and Ir) have the similar geometries.

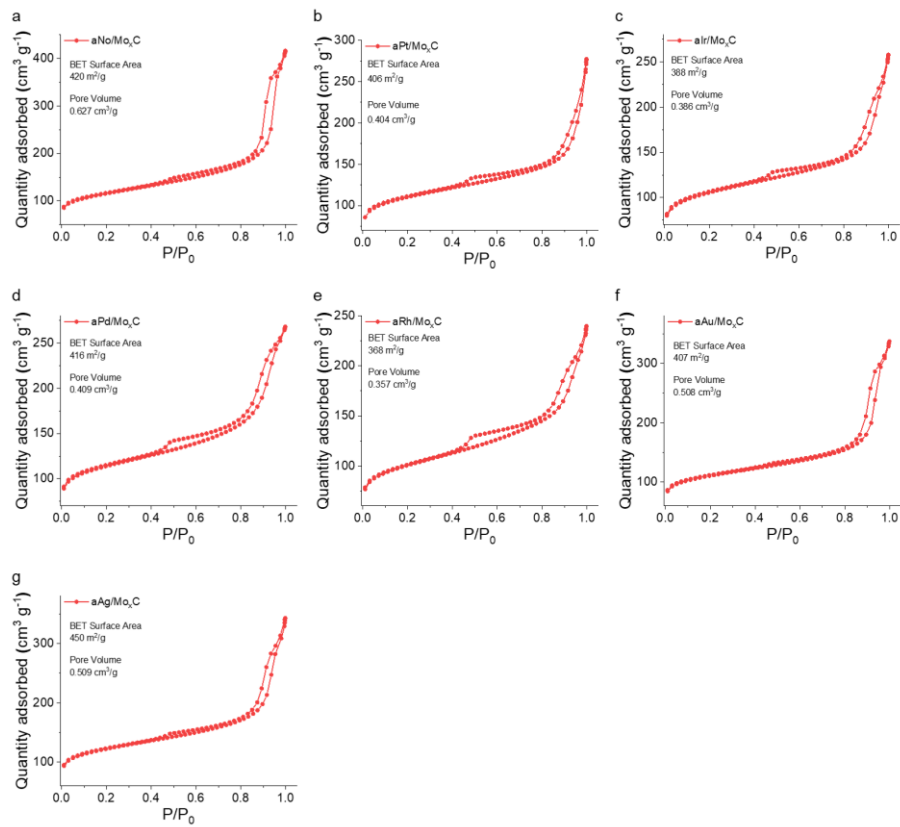


Fig. S15 N₂ physisorption for aNM/Mo_xC. N₂ adsorption-desorption isotherms of aNM/Mo_xC for (a) aNo/Mo_xC, (b) aPt/Mo_xC, (c) aIr/Mo_xC, (d) aPd/Mo_xC, (e) aRh/Mo_xC, (f) aAu/Mo_xC, and (g) aAg/Mo_xC with their BET surface area [m²·g⁻¹] and pore volume [cm³·g⁻¹].

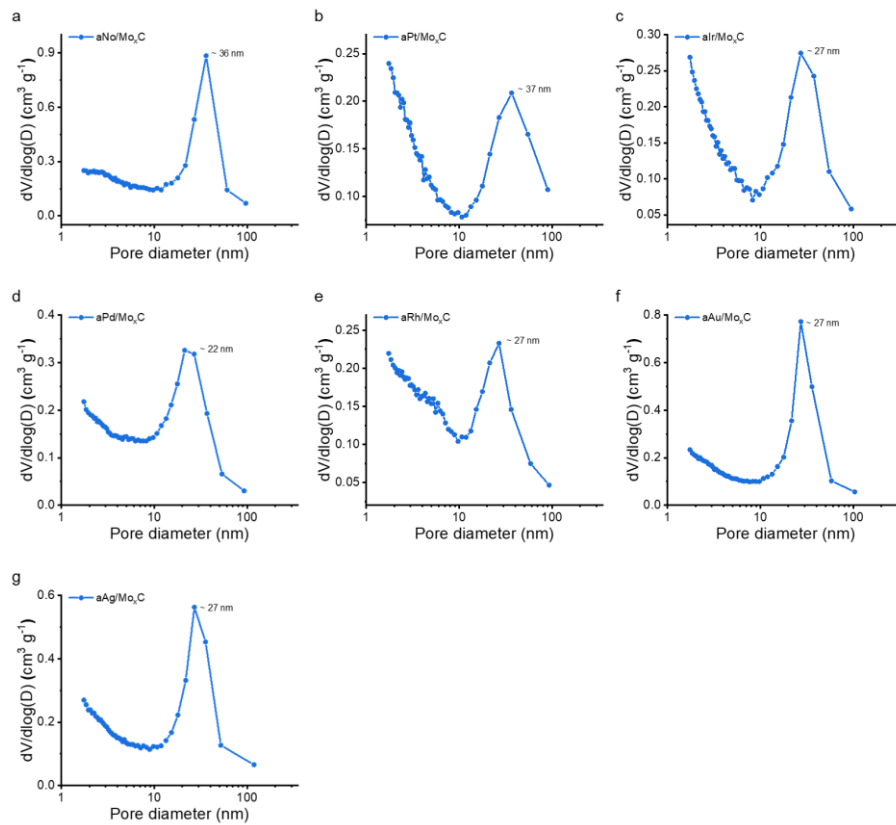


Fig. S16 Pore size distribution for aNM/Mo_xC. Pore size distribution from N₂ adsorption-desorption isotherms of aNM/Mo_xC for (a) aNo/Mo_xC, (b) aPt/Mo_xC, (c) aIr/Mo_xC, (d) aPd/Mo_xC, (e) aRh/Mo_xC, (f) aAu/Mo_xC, and (g) aAg/Mo_xC.

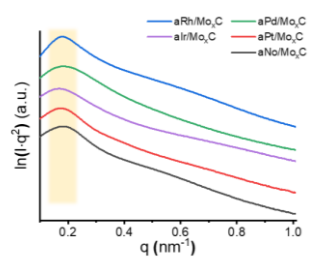


Fig. S17 Small-angle X-ray scattering (SAXS) patterns for aNM/Mo_xC. SAXS patterns of aNM/Mo_xC for aNo/Mo_xC aPt/Mo_xC, aIr/Mo_xC, aPd/Mo_xC, and aRh/Mo_xC.

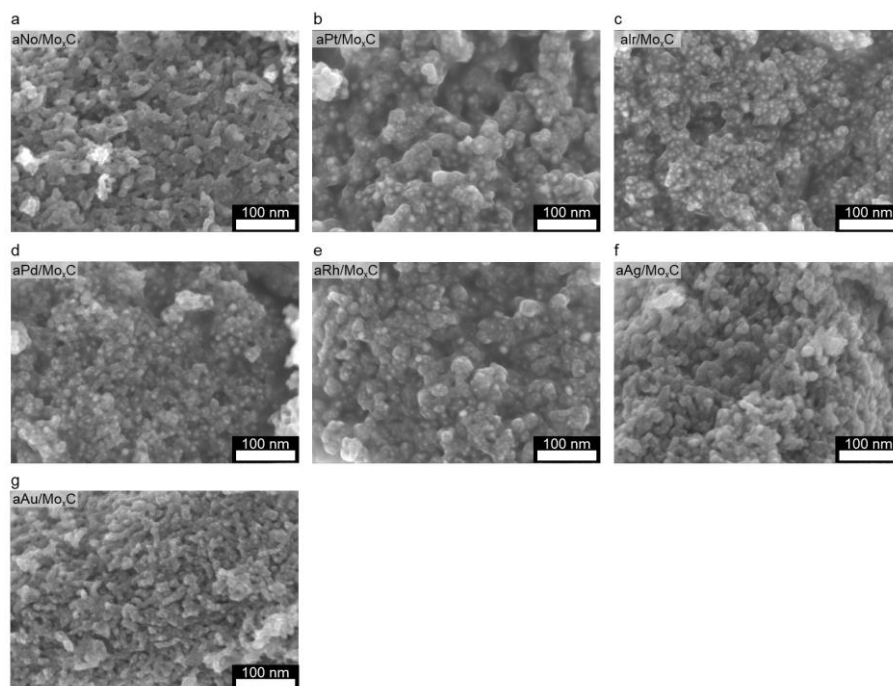


Fig. S18 Scanning electron microscopy (SEM) images of aNM/Mo_xC. SEM images of (a) aNo/Mo_xC, (b) aPt/Mo_xC, (c) aIr/Mo_xC, (d) aPd/Mo_xC, (e) aRh/Mo_xC, (f) aAg/Mo_xC, and (g) aAu/Mo_xC.

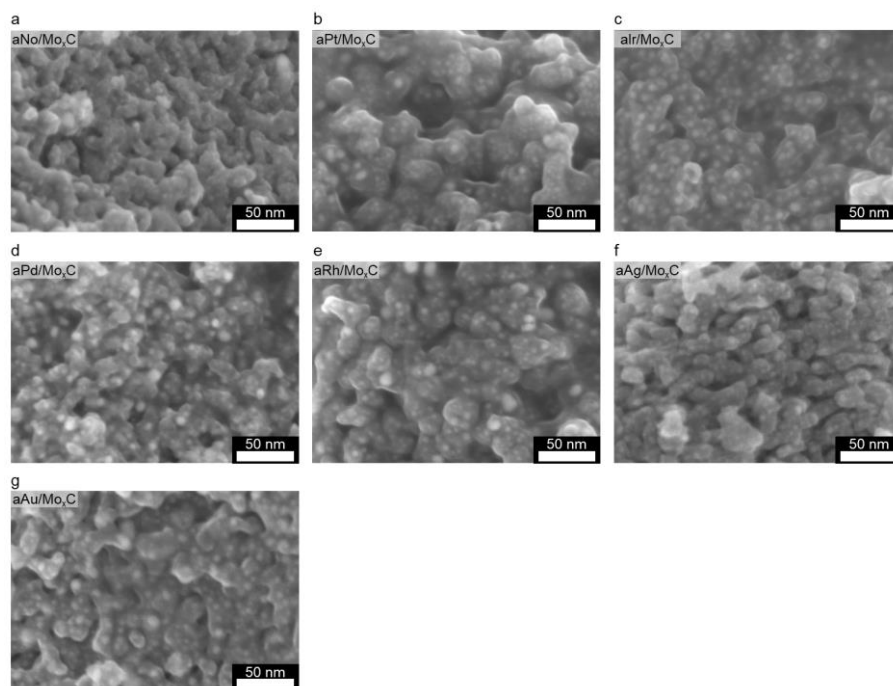


Fig. S19 Enlarged SEM images of aNM/Mo_xC. Enlarged SEM images of (a) aNo/Mo_xC, (b) aPt/Mo_xC, (c) aIr/Mo_xC, (d) aPd/Mo_xC, (e) aRh/Mo_xC, (f) aAg/Mo_xC, and (g) aAu/Mo_xC.

SEM images demonstrated that Mo_xC NPs were evenly dispersed at mesoporous heterostructured Mo_xC-C, regardless of type of NM precursor.

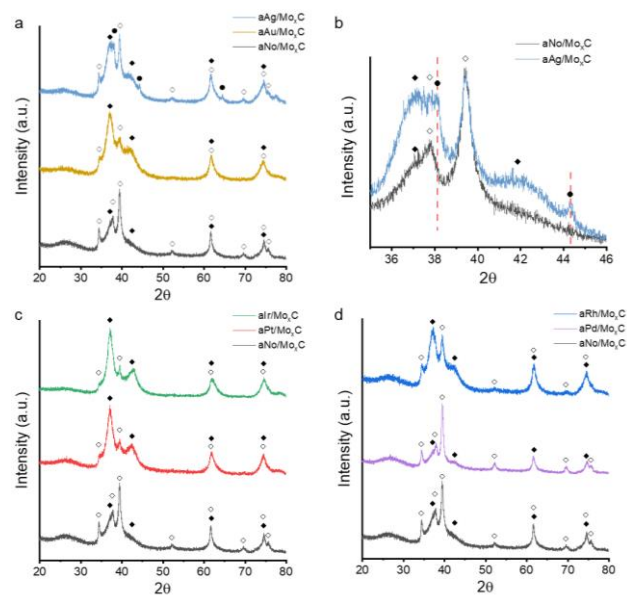


Fig. S20 XRD patterns for aNM/Mo_xC. XRD patterns for aNM/Mo_xC for (a) aAg/Mo_xC and aAu/Mo_xC, (c) aIr/Mo_xC and aPt/Mo_xC, and (d) aRh/Mo_xC and aPd/Mo_xC with enlarged XRD patterns for (b) aAg/Mo_xC to show the crystalline Ag peak. (◆: α-MoC [JCPDS 01-089-2868], ◇: β-Mo₂C [JCPDS 00-011-0608], ●: Ag [JCPDS 04-0783])

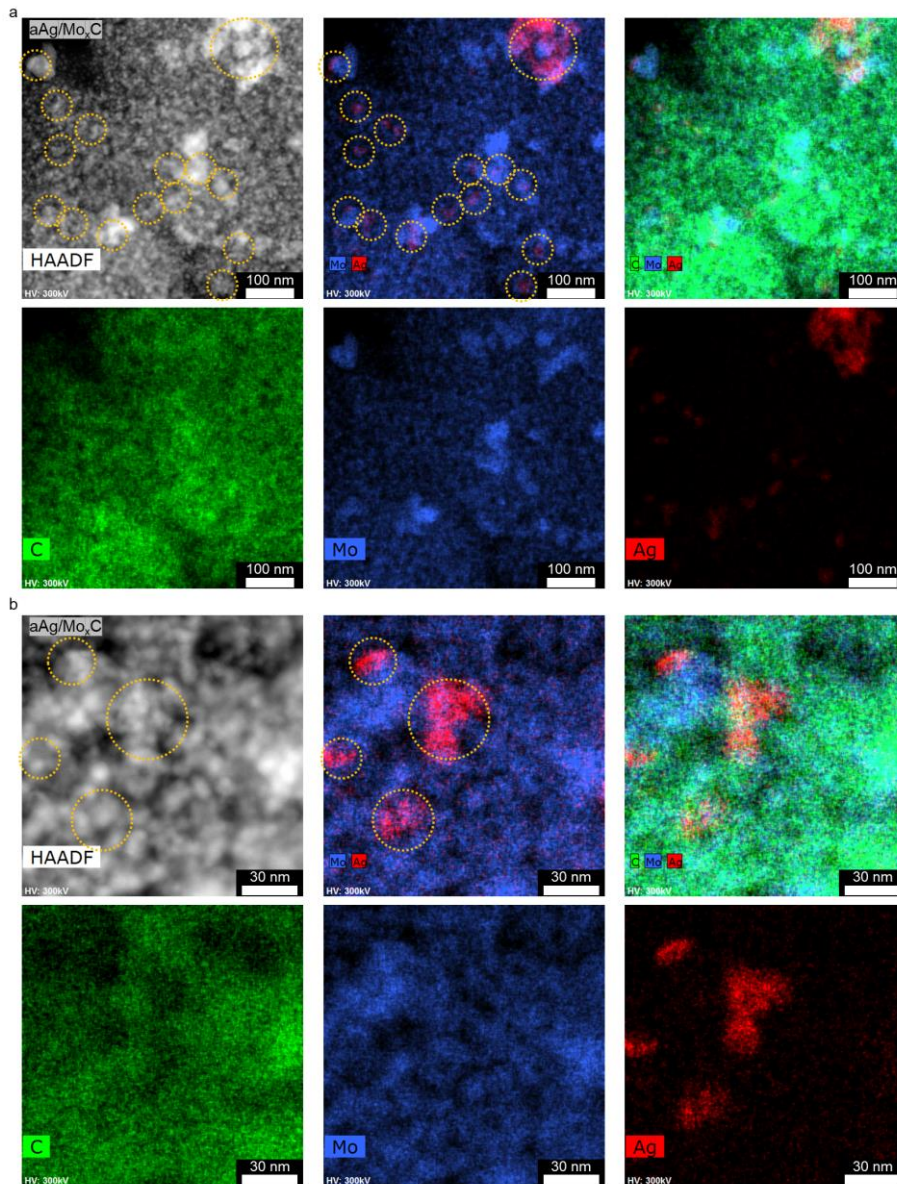


Fig. S21 STEM analysis for aAg/Mo_xC. (a) HAADF-STEM images and corresponding EDS mappings, and (b) enlarged HAADF-STEM images and corresponding EDS mappings of aAg/Mo_xC for C, Mo, Ag, and their overlap (red: Ag, blue: Mo, green: C, orange circles: Ag agglomerates),

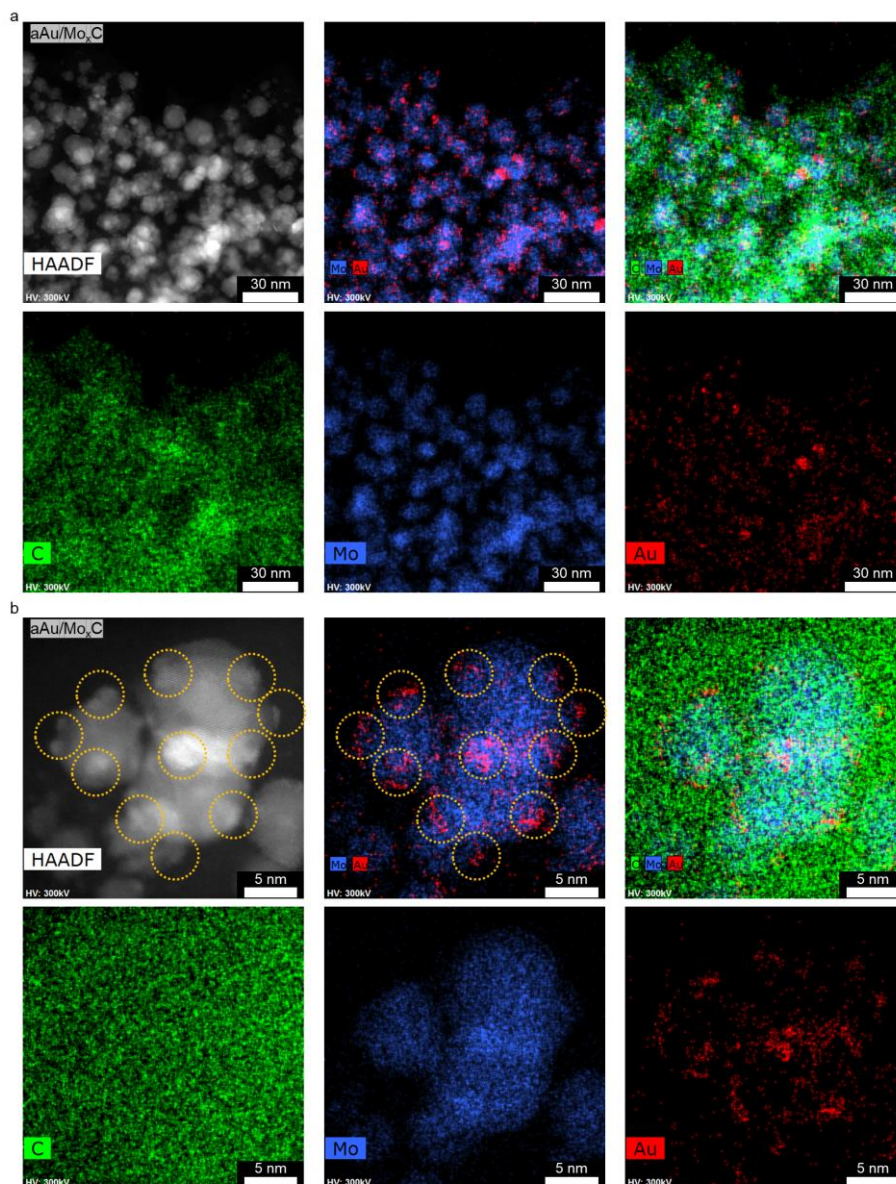


Fig. S22 STEM analysis for aAu/Mo_xC . (a) HAADF-STEM images and corresponding EDS mappings, and (b) enlarged HAADF-STEM images and corresponding EDS mappings of aAu/Mo_xC for C, Mo, Au, and their overlap (red: Au, blue: Mo, green: C, orange circles: Au hemispheres),

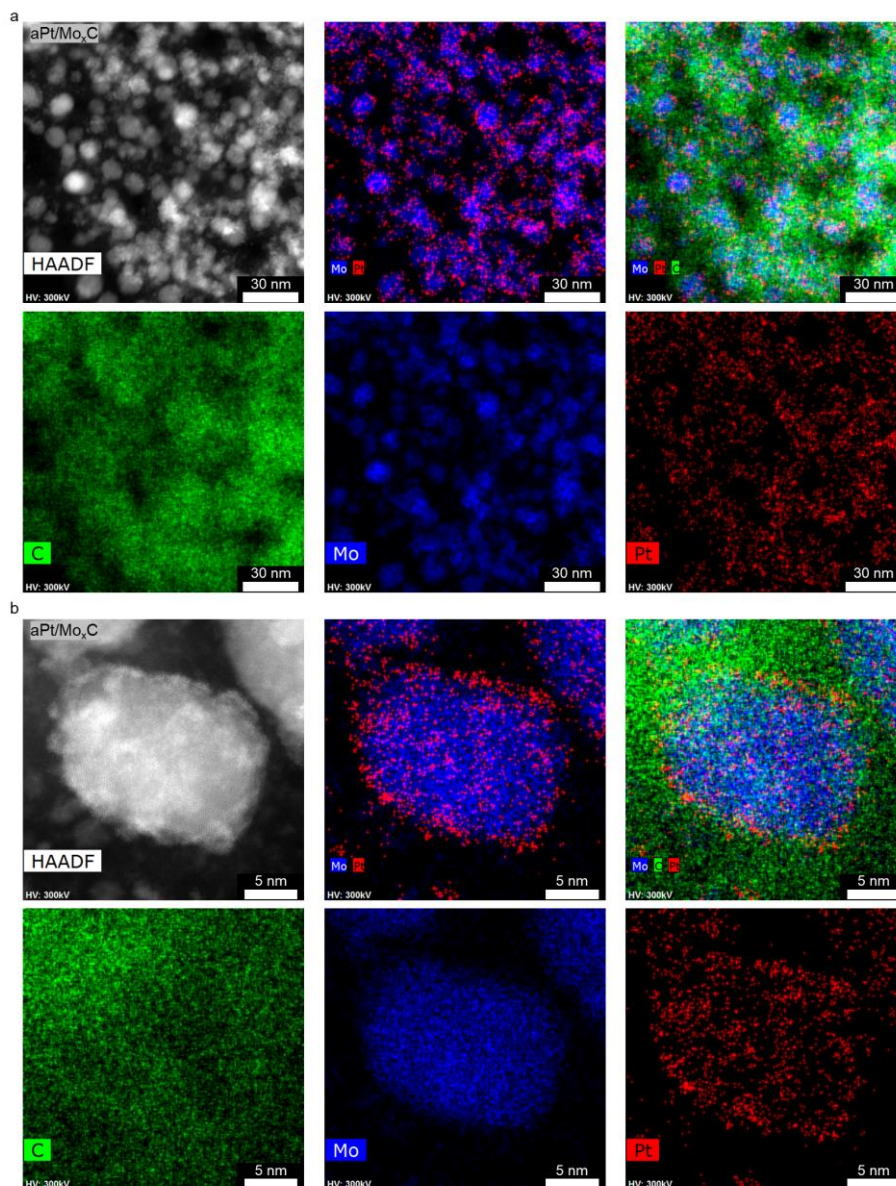


Fig. S23 STEM analysis for aPt/Mo_xC. (a) HAADF-STEM images and corresponding EDS mappings, and (b) enlarged HAADF-STEM images and corresponding EDS mappings of aPt/Mo_xC for C, Mo, Pt, and their overlap (red: Pt, blue: Mo, green: C),

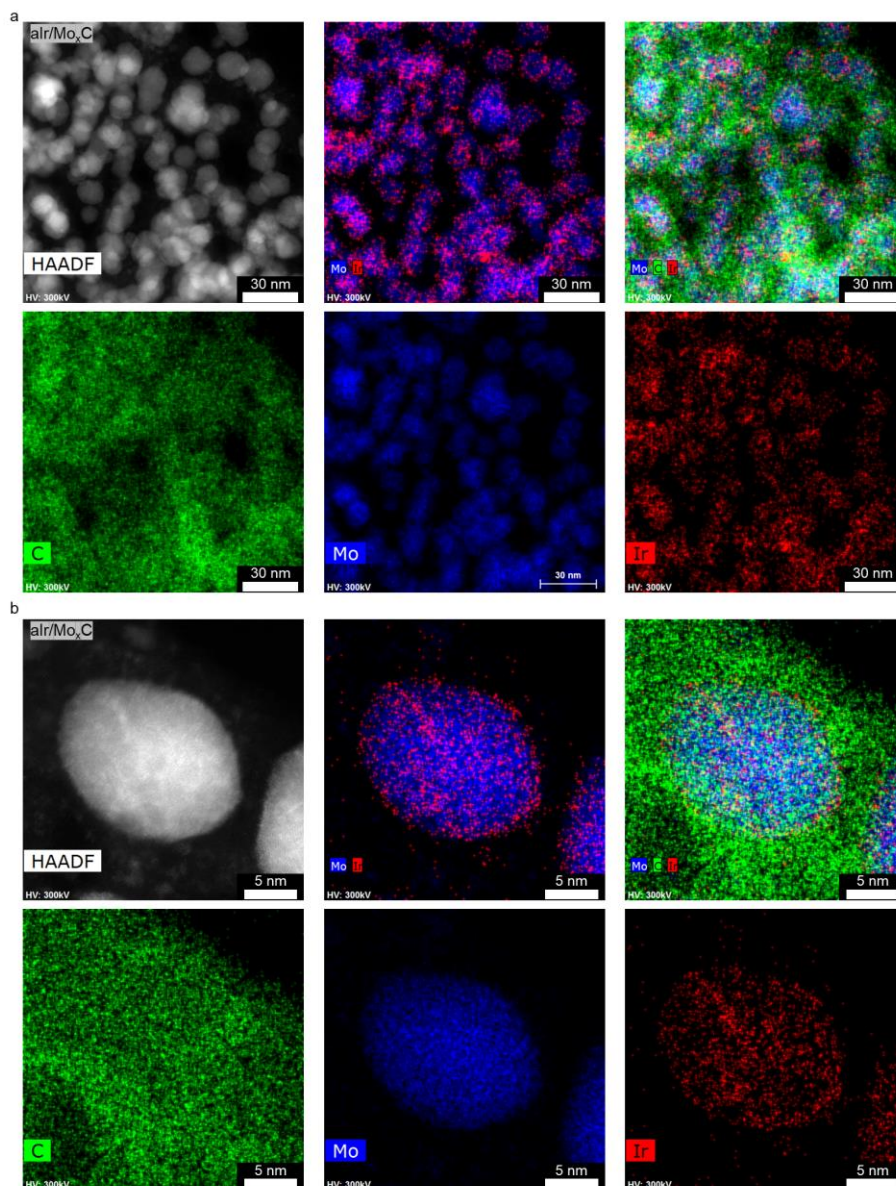


Fig. S24 Enlarged STEM analysis for $\text{alr/Mo}_x\text{C}$. (a) HAADF-STEM images and corresponding EDS mappings, and (b) enlarged HAADF-STEM images and corresponding EDS mappings of $\text{alr/Mo}_x\text{C}$ for C, Mo, Ir, and their overlap (red: Ir, blue: Mo, green: C),

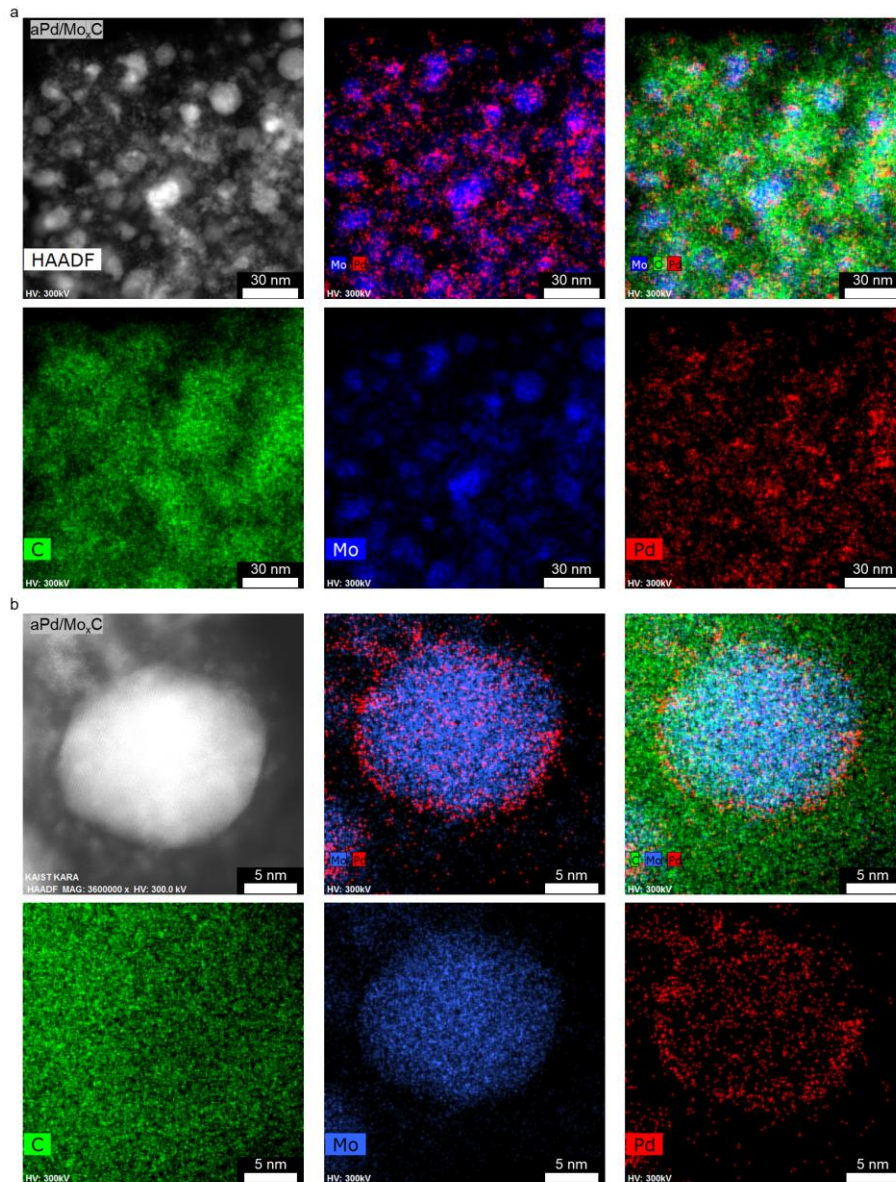


Fig. S25 STEM analysis for aPd/Mo_xC. (a) HAADF-STEM images and corresponding EDS mappings, and (b) enlarged HAADF-STEM images and corresponding EDS mappings of aPd/Mo_xC for C, Mo, Pd, and their overlap (red: Pd, blue: Mo, green: C),

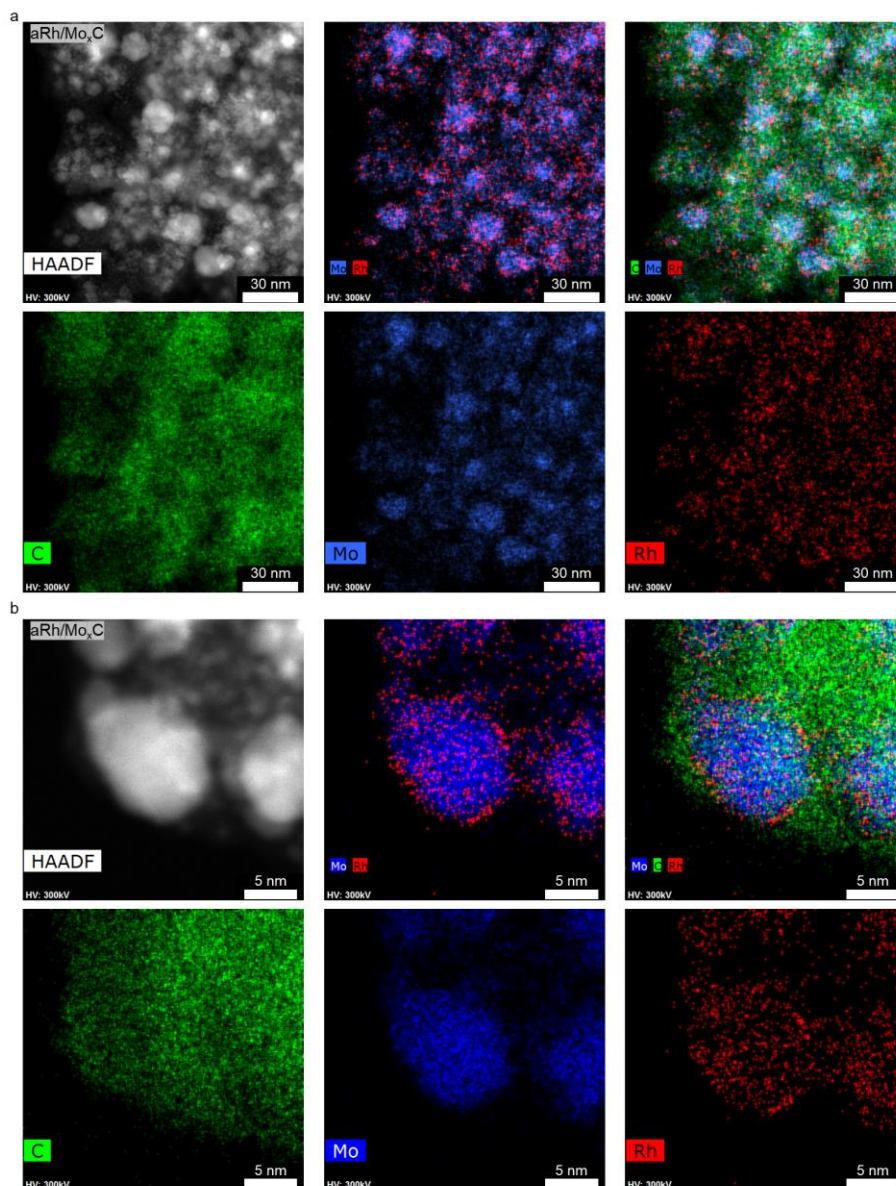


Fig. S26 STEM analysis for aRh/Mo_xC. (a) HAADF-STEM images and corresponding EDS mappings, and (b) enlarged HAADF-STEM images and corresponding EDS mappings of aRh/Mo_xC for C, Mo, Rh, and their overlap (red: Rh, blue: Mo, green: C),

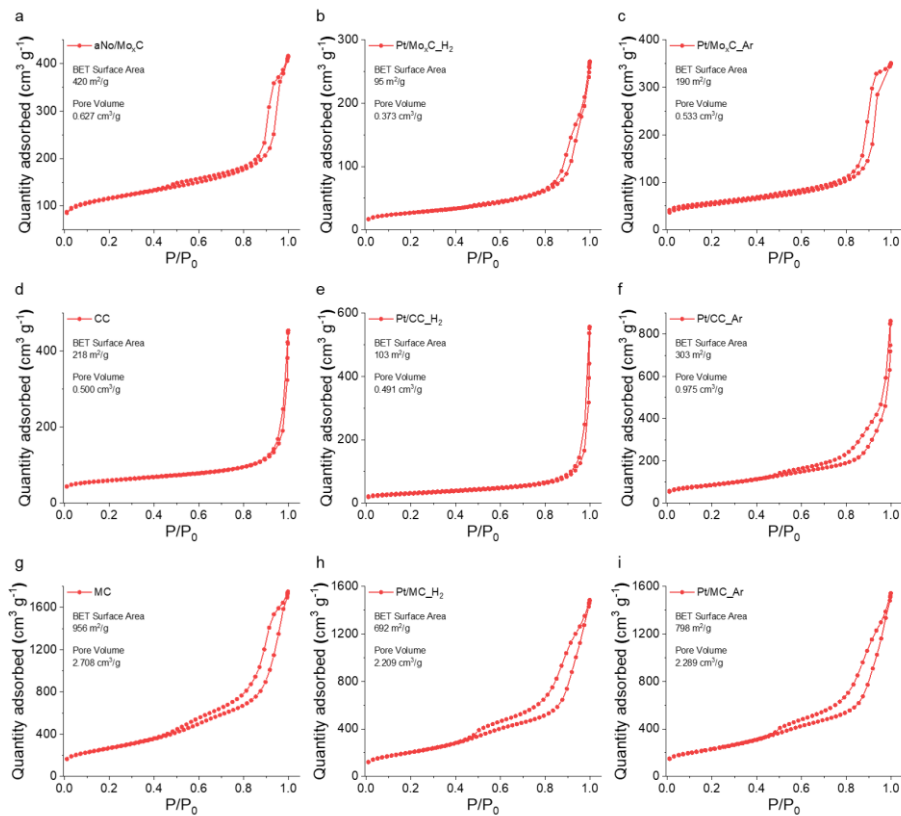


Fig. S27 N₂ physisorption for Pt on support with different synthesis strategy. N₂ adsorption-desorption isotherms of support (a, d, g) and Pt loaded support, with low-*T* (373 K, 10% H₂/Ar) reduction (b, e, h) and high-*T* (1,373 K, Ar) treatment (c, f, i) with BET surface area [m²·g⁻¹] and pore volume [cm³·g⁻¹]. (a) aNo/Mo_xC, (b) Pt/Mo_xC_H₂, (c) Pt/Mo_xC_Ar, (d) CC, (e) Pt/CC_H₂, (f) Pt/CC_Ar, (g) MC, (h) Pt/MC_H₂, and (i) Pt/MC_Ar.

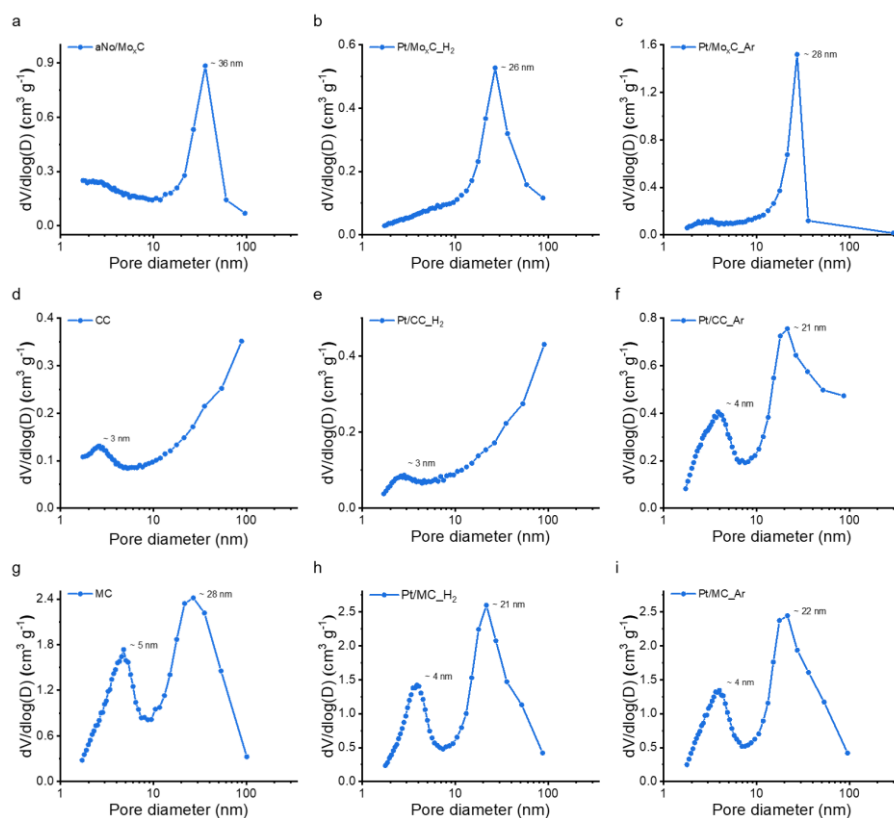


Fig. S28 Pore size distribution for Pt on support with different synthesis strategy. Pore size distribution from N_2 adsorption-desorption isotherms of support (a, d, g) and Pt loaded support, with low- T (373 K, 10% H_2/Ar) reduction (b, e, h) and high- T (1,373 K, Ar) treatment (c, f, i) with pore size (nm). (a) aNo/Mo_xC, (b) Pt/Mo_xC_{H₂}, (c) Pt/Mo_xC_{Ar}, (d) CC, (e) Pt/CC_{H₂}, (f) Pt/CC_{Ar}, (g) MC, (h) Pt/MC_{H₂}, and (i) Pt/MC_{Ar}.

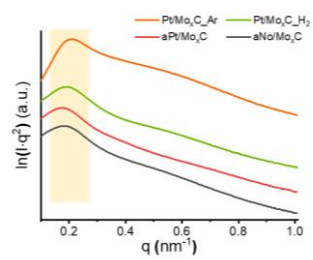


Fig. S29 Small-angle X-ray scattering patterns for Pt on Mo_xC-C with different synthesis strategy. SAXS patterns of aNo/Mo_xC, aPt/Mo_xC, Pt/Mo_xC_{H₂}, and Pt/Mo_xC_{Ar}.

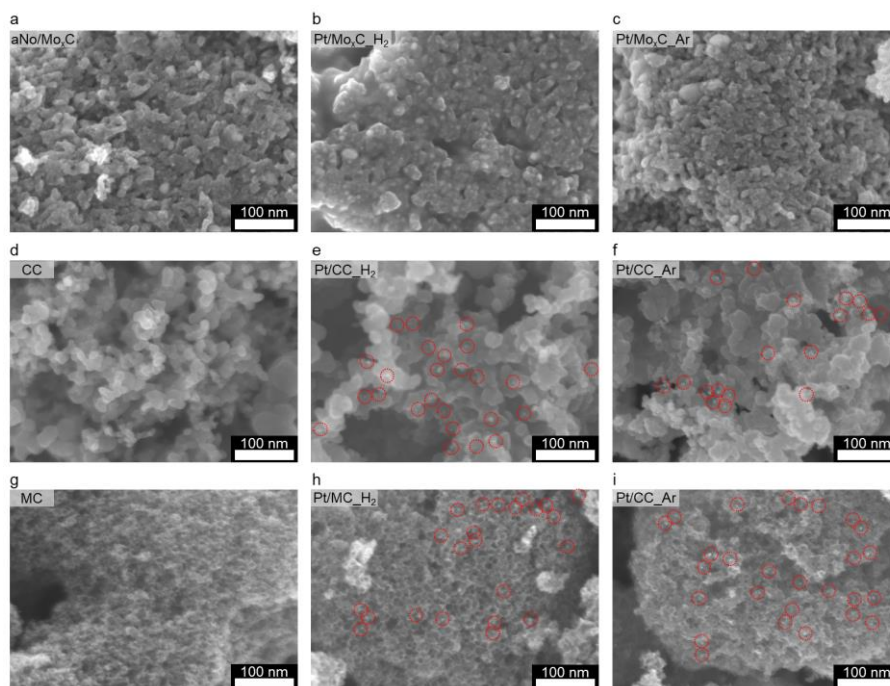


Fig. S30 SEM images of Pt on support with different synthesis strategy. SEM images of (a) aNo/Mo_xC, (b) Pt/Mo_xC_H₂, (c) Pt/Mo_xC_Ar, (d) CC, (e) Pt/CC_H₂, (f), Pt/CC_Ar, (g) MC, (h) Pt/MC_H₂, (i) Pt/MC_Ar (red circle: large Pt particles).

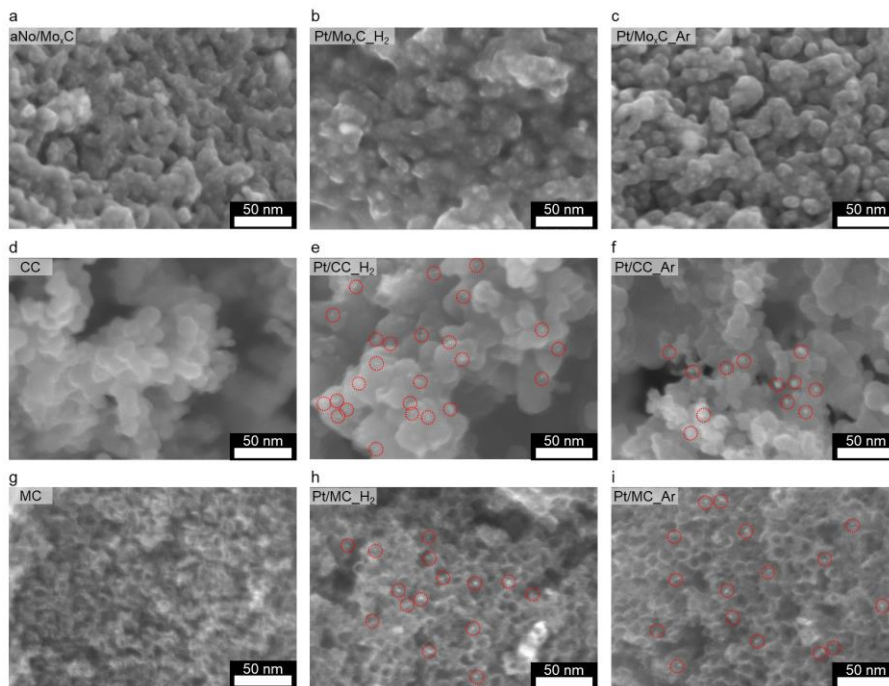


Fig. S31 Enlarged SEM images of Pt on support with different synthesis strategy. Enlarged SEM images of (a) aNo/Mo_xC, (b) Pt/Mo_xC_H₂, (c) Pt/Mo_xC_Ar, (d) CC, (e) Pt/CC_H₂, (f) Pt/CC_Ar, (g) MC, (h) Pt/MC_H₂, (i) Pt/MC_Ar (red circle: large Pt particles).

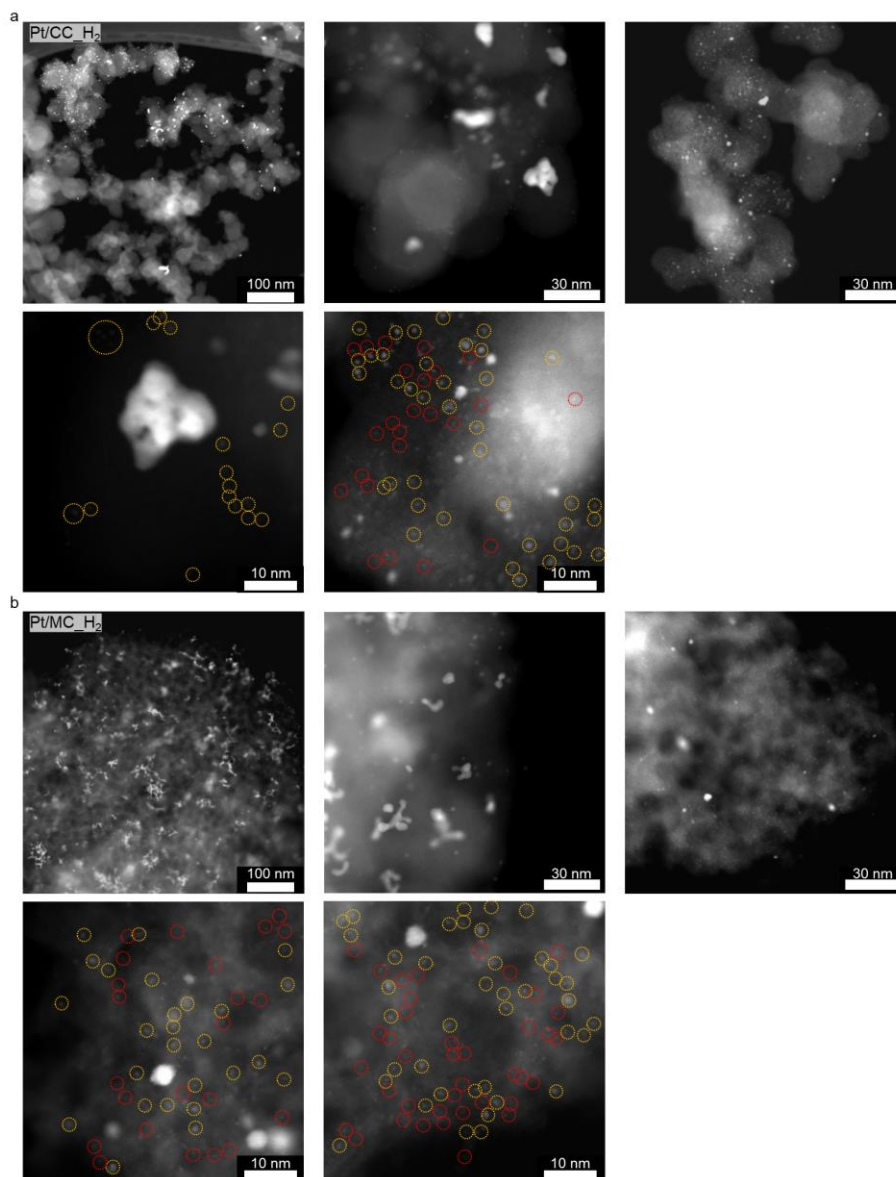


Fig. S32 STEM analysis of Pt/CC_H₂ and Pt/MC_H₂. STEM images of (a) Pt/CC_H₂ and (b) Pt/MC_H₂ at different magnifications (red circle: single-atom Pt, orange circle: Pt atomic cluster).

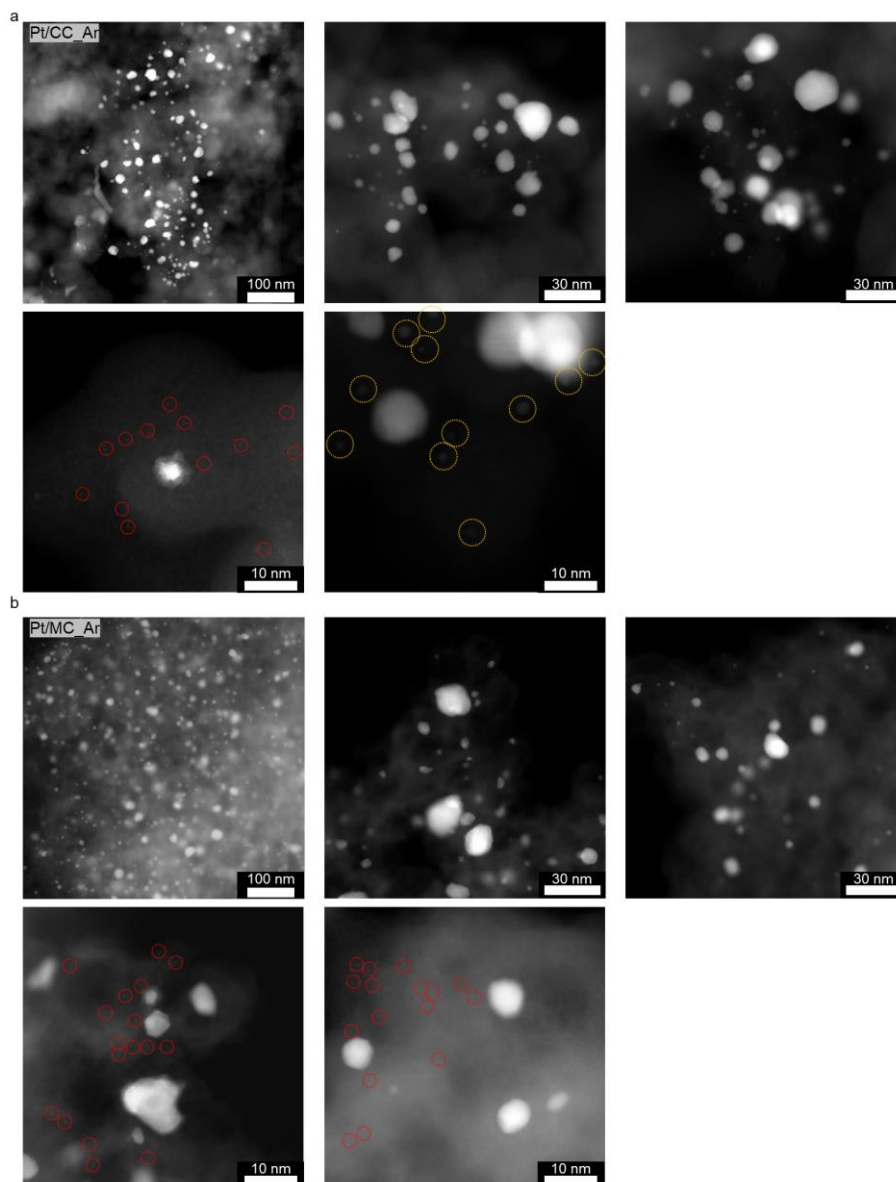


Fig. S33 STEM analysis of Pt/CC_Ar and Pt/MC_Ar. STEM images of (a) Pt/CC_Ar and (b) Pt/MC_Ar at different magnifications (red circle: single-atom Pt, orange circle: Pt atomic cluster).

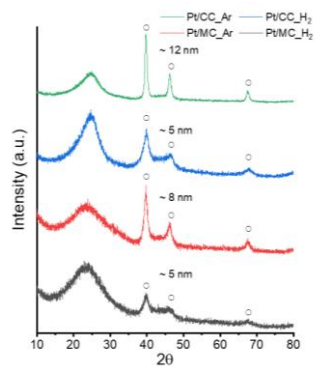


Fig. S34 XRD patterns of Pt on carbon support with different synthesis strategy. XRD patterns for Pt/CC_Ar (green), Pt/CC_H₂ (blue), Pt/MC_Ar (red), and Pt/MC_H₂ (black) with crystallite sizes calculated using the Scherrer equation. (○: Pt [JCPDS 04-0802])

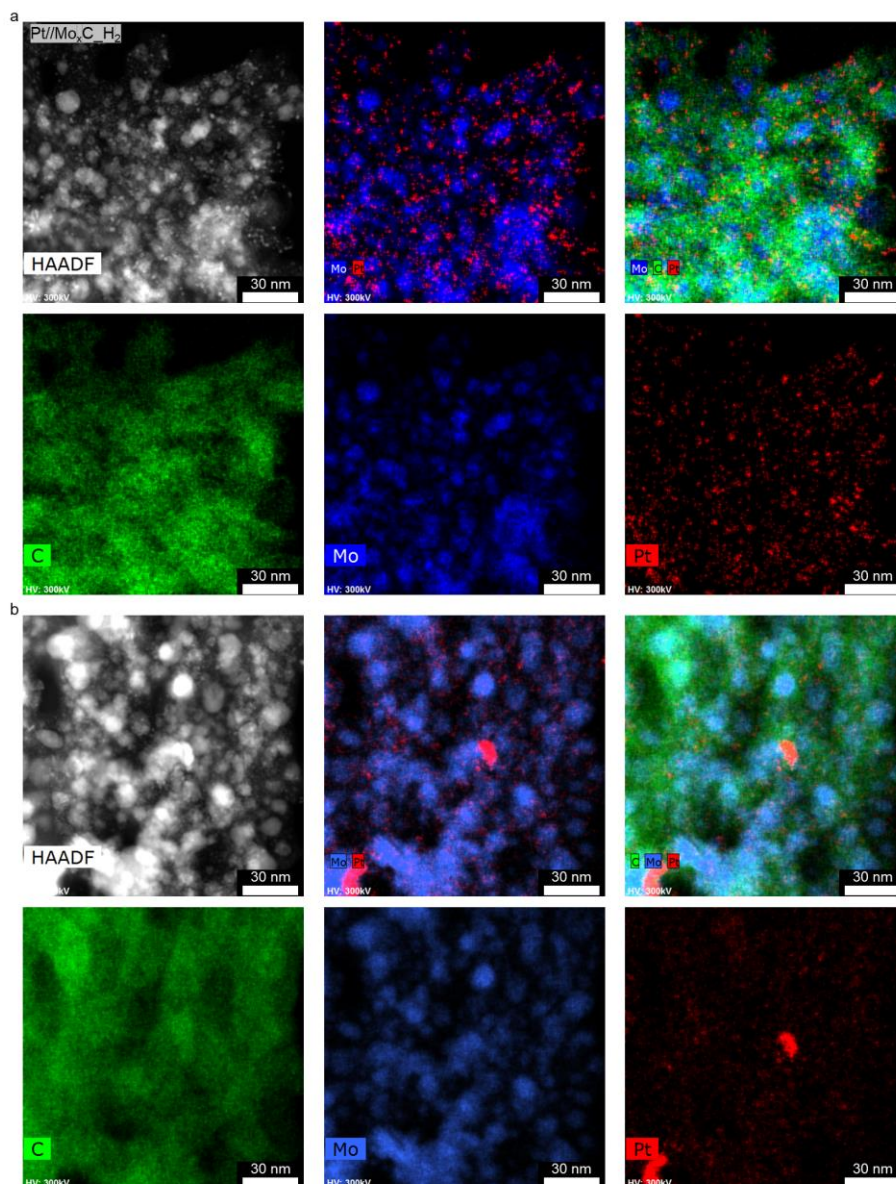


Fig. S35 STEM analysis of Pt/Mo_xC_{H₂}. STEM images and corresponding EDS mappings of Pt/Mo_xC_{H₂} (red: Pt, blue: Mo, green: C).

From the EDS mapping, Pt nanoclusters were mainly distributed on carbon (Fig. S35a), which is not overlapped on Mo, and some large Pt clusters were observed (Fig. S35b), which results from the uneven loading of Pt with wet impregnation.

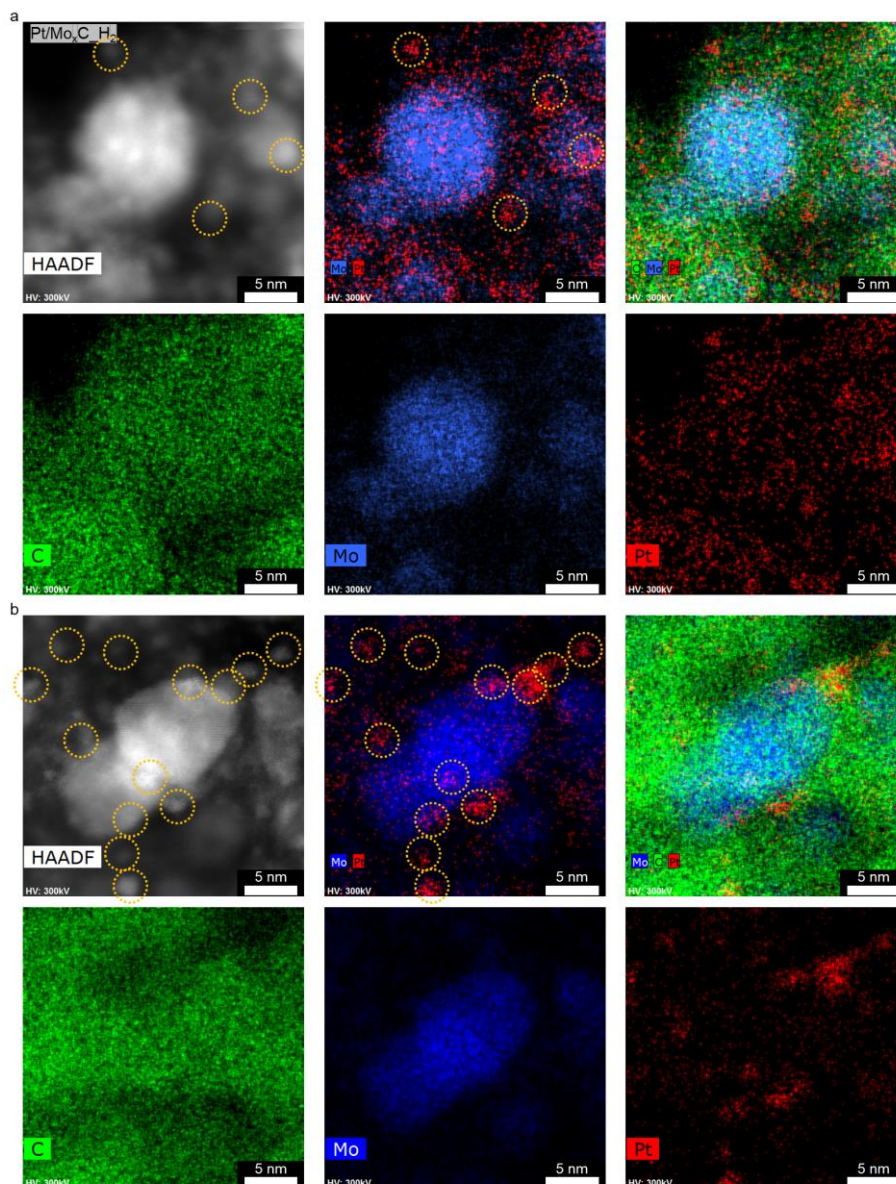


Fig. S36 Enlarged STEM analysis of Pt/Mo_xC_{1-x}H₂. Enlarged STEM images and corresponding EDS mappings of Pt/Mo_xC_{1-x}H₂ (red: Pt, blue: Mo, green: C, yellow circles: Pt clusters).

From the EDS mapping, Pt nanoclusters were mainly distributed on carbon (Fig. S36a), which is not overlapped on Mo, and Pt with atom-dimension structure were existed on carbon surface (Fig. S36b).

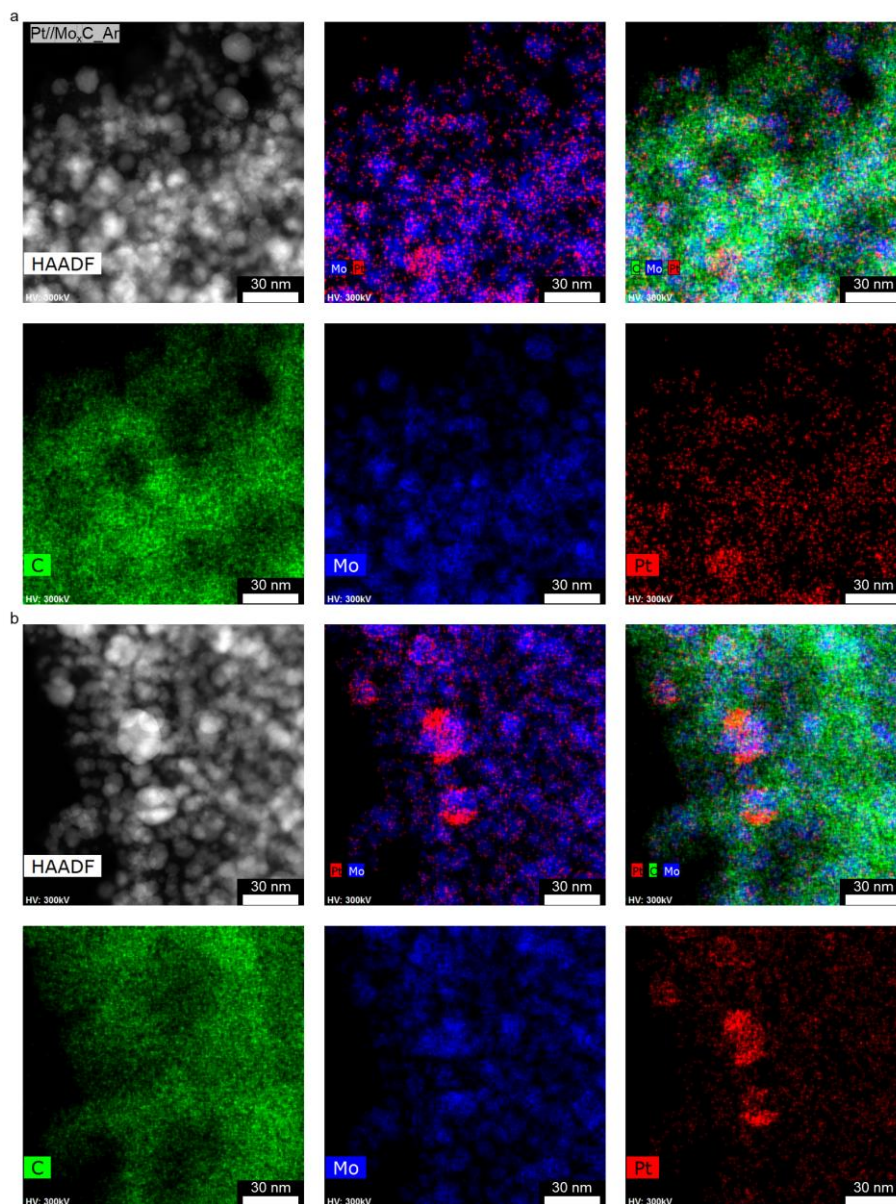


Fig. S37 STEM analysis of Pt/Mo_xC_Ar. STEM images and corresponding EDS mappings of Pt/Mo_xC_Ar (red: Pt, blue: Mo, green: C).

From the EDS mapping, Pt ADCs were distributed selectively on Mo_xC (Fig. S37a), and some large Pt clusters were observed (Fig. S37b), which results from the uneven loading of Pt with wet impregnation.

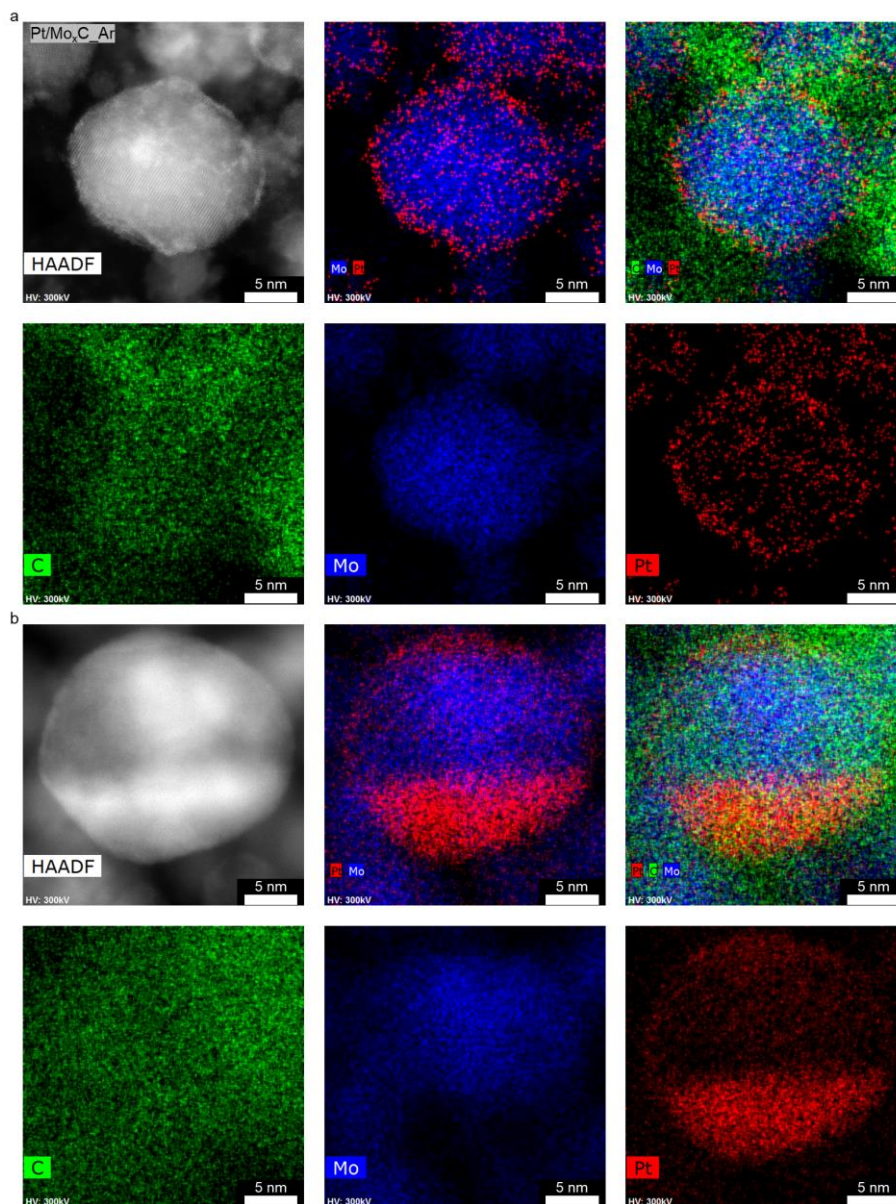


Fig. S38 Enlarged STEM analysis of Pt/Mo_xC_Ar. Enlarged STEM images and corresponding EDS mappings of Pt/Mo_xC_Ar (red: Pt, blue: Mo, green: C).

From the EDS mapping, crystalline Pt was segregated out on Mo_xC NPs (Fig. S38a), which results from the uneven loading of Pt with wet impregnation, and a shell-like Pt distribution on Mo_xC surface (Fig. S38b), which indicates that dynamic placement of Pt selectively on Mo_xC surface occurs.

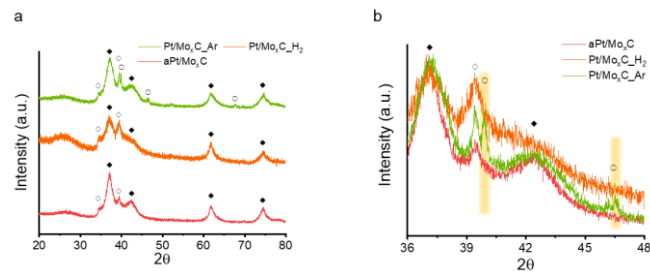


Fig. S39 XRD patterns of Pt/Mo_xC-C with different synthesis strategy. (a) XRD patterns for aPt/Mo_xC (red), Pt/Mo_xC_{H₂} (orange), and Pt/Mo_xC_{Ar} (yellow green), and (b) enlarged XRD patterns to distinguish the crystalline Pt species. (◆: α-MoC [JCPDS 01-089-2868], ◇: β-Mo₂C [JCPDS 00-011-0608], ○: Pt [JCPDS 04-0802])

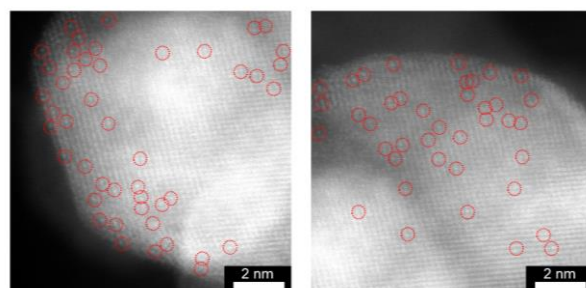


Fig. S40 Z-contrast images of Pt/Mo_xC_{Ar}. HAADF-STEM images of Pt/Mo_xC_{Ar} (red circle: single-atom Pt)

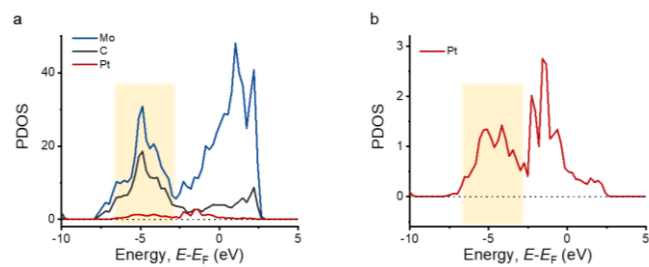


Fig. S41 Theoretical calculation of electronic structure for aPt/Mo_xC. Partial density of state (PDOS) of (a) aPt/Mo_xC for Pt (red), Mo (blue), and C (black), and (b) enlarged PDOS of aPt/Mo_xC for Pt (red) obtained using DFT calculation (yellow region: DOS from hybridized Mo and C states).

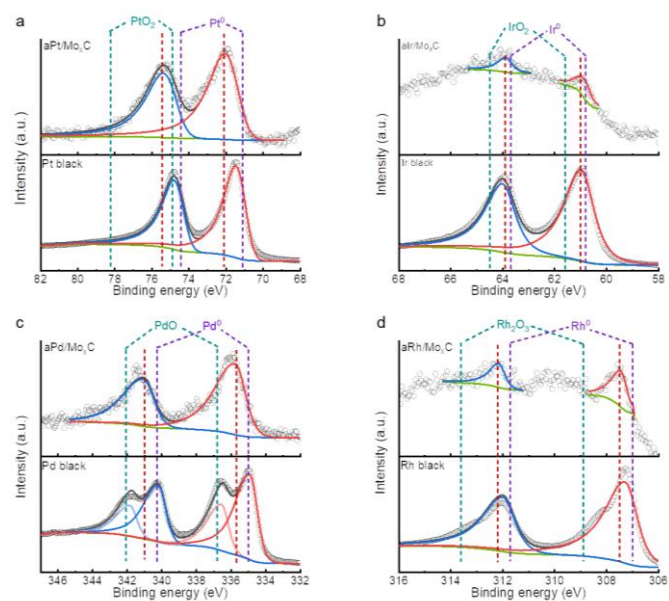


Fig. S42 X-ray photoelectron spectroscopy (XPS) of aNM/Mo_xC with NM black. XPS of (a) Pt 4f region for aPt/Mo_xC and Pt black, (b) Ir 4f region for aIr/Mo_xC and Ir black, (c) Pd 3d region for aPd/Mo_xC and Pd black, and (d) Rh 3d region for aRh/Mo_xC and Rh black.

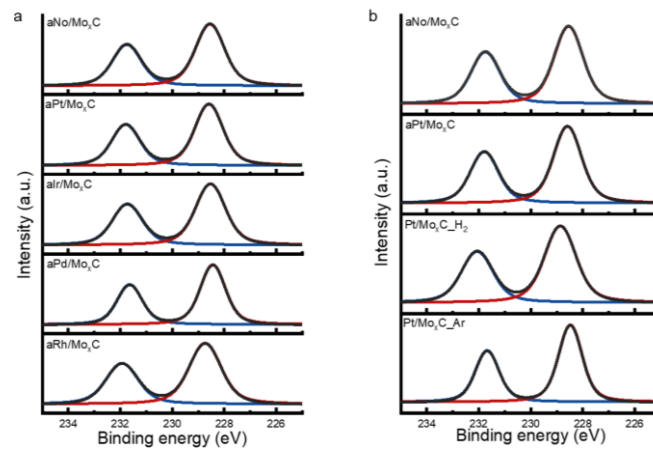


Fig. S43 XPS of aNM/Mo_xC for Mo 3d region. Extraction of Mo_xC spectrum in XPS of Mo 3d region according to (a) type of NM (aNo/Mo_xC, aPt/Mo_xC, aIr/Mo_xC, aPd/Mo_xC, and aRh/Mo_xC), and (b) synthesis strategy (aNo/Mo_xC, aPt/Mo_xC, Pt/Mo_xC_{H₂}, and Pt/Mo_xC_{Ar}).

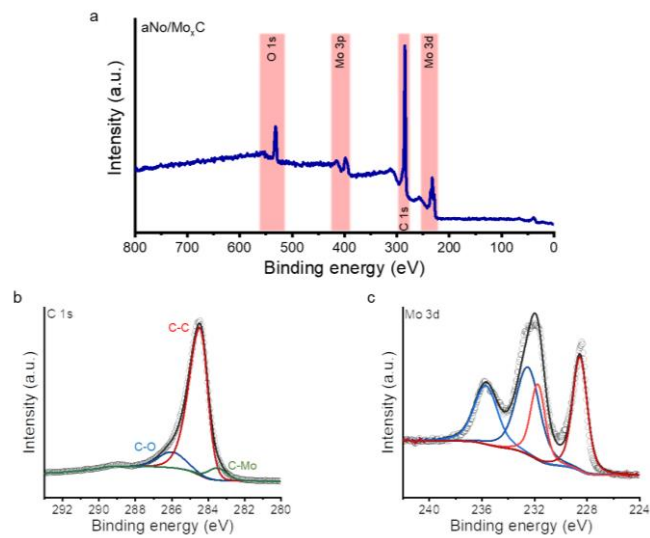


Fig. S44 XPS analysis of aNo/Mo_xC. XPS measurement of aNo/Mo_xC. (a) XPS survey spectrum, (b) C 1s region (green: C-Mo, red: C=C, blue: C-O), and (c) Mo 3d region of XPS (red: Mo_xC, blue: surface MoO_x due to naturally-formed oxide).

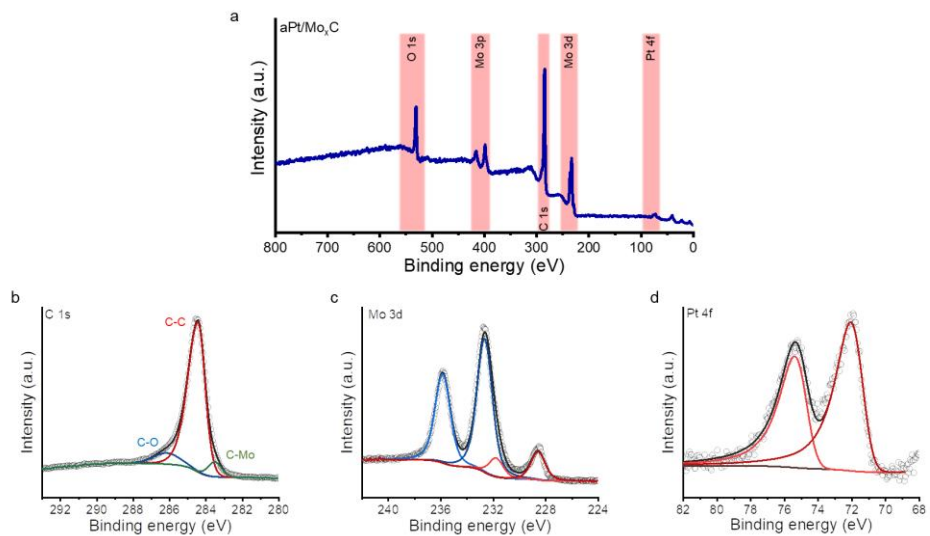


Fig. S45 XPS analysis of aPt/Mo_xC. XPS measurement of aPt/Mo_xC. (a) XPS survey spectrum, (b) C 1s region (green: C-Mo, red: C=C, blue: C-O), (c) Mo 3d region of XPS (red: Mo_xC, blue: surface MoO_x due to naturally formed oxide), and (d) Pt 4f region of XPS.

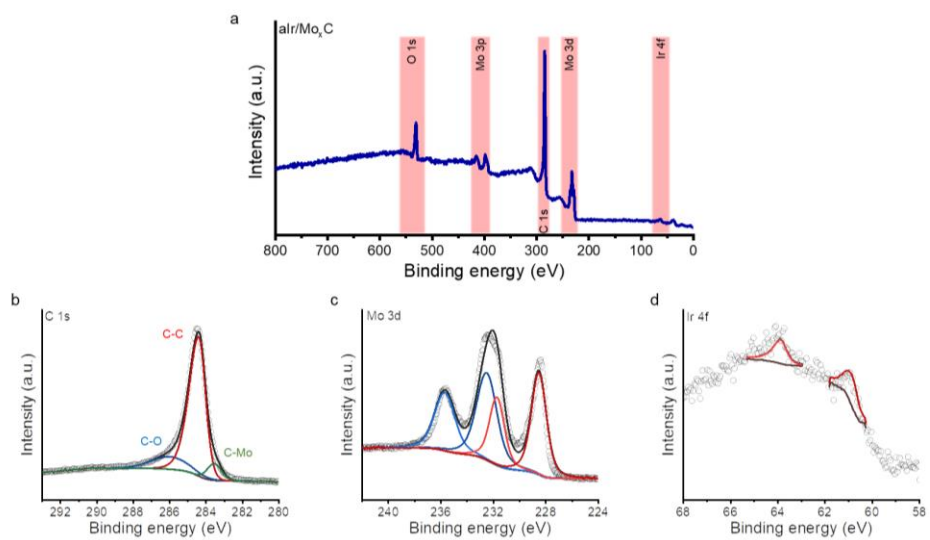


Fig. S46 XPS analysis of alr/Mo_xC. XPS measurement of alr/Mo_xC. (a) XPS survey spectrum, (b) C 1s region (green: C-Mo, red: C=C, blue: C-O), (c) Mo 3d region of XPS (red: Mo_xC, blue: surface MoO_x due to naturally-formed oxide), and (d) Ir 4f region of XPS.

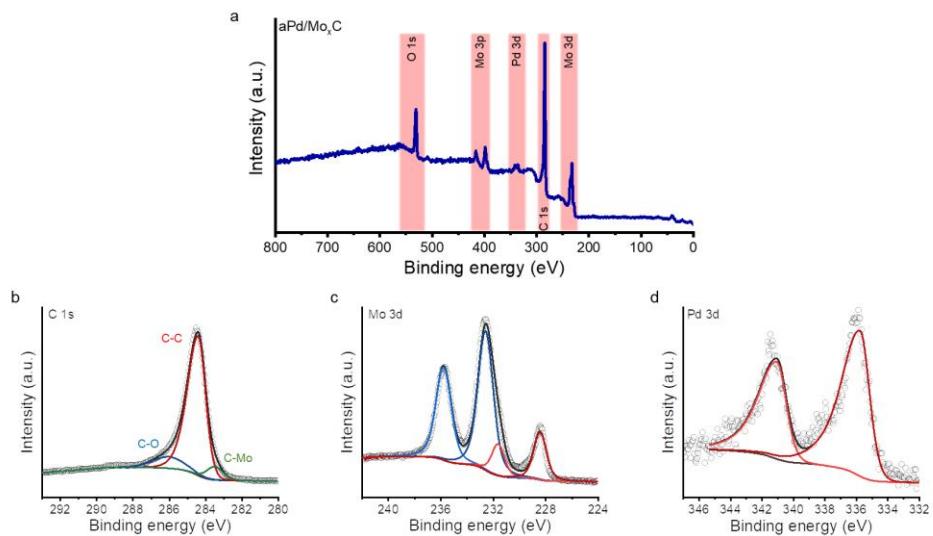


Fig. S47 XPS analysis of aPd/Mo_xC. XPS measurement of aPd/Mo_xC. (a) XPS survey spectrum, (b) C 1s region (green: C-Mo, red: C=C, blue: C-O), (c) Mo 3d region of XPS (red: Mo_xC, blue: surface MoO_x due to naturally formed oxide), and (d) Pd 3d region of XPS.

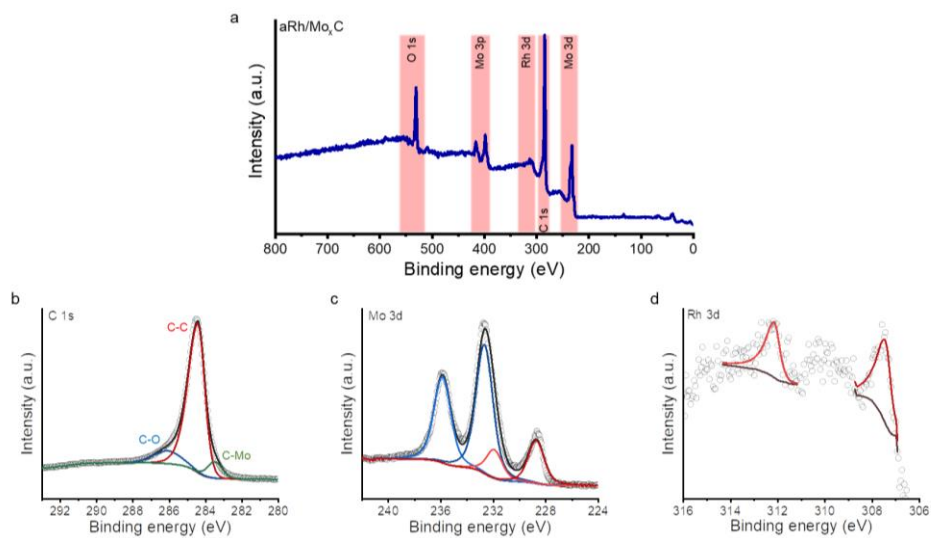


Fig. S48 XPS analysis of aRh/Mo_xC. XPS measurement of aRh/Mo_xC. (a) XPS survey spectrum, (b) C 1s region (green: C-Mo, red: C=C, blue: C-O), (c) Mo 3d region of XPS (red: Mo_xC, blue: surface MoO_x due to naturally-formed oxide), and (d) Rh 3d region of XPS.

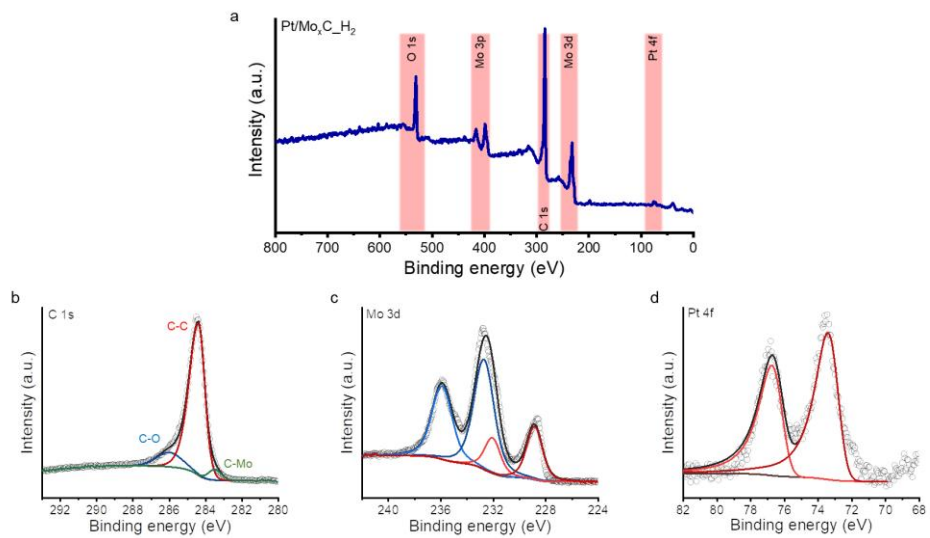


Fig. S49 XPS analysis of Pt/Mo_xC_{0.2}H₂. XPS measurement of Pt/Mo_xC_{0.2}H₂. (a) XPS survey spectrum, (b) C 1s region (green: C-Mo, red: C=C, blue: C-O), (c) Mo 3d region of XPS (red: Mo_xC, blue: surface MoO_x due to naturally-formed oxide), and (d) Pt 4f region of XPS.

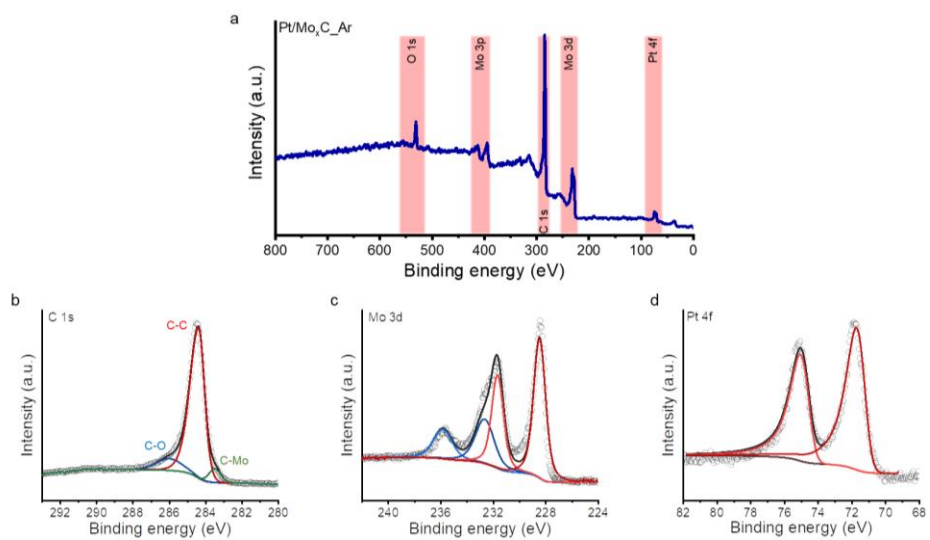


Fig. S50 XPS analysis of Pt/Mo_xC_yAr. XPS measurement of Pt/Mo_xC_yAr. (a) XPS survey spectrum, (b) C 1s region (green: C-Mo, red: C=C, blue: C-O), (c) Mo 3d region of XPS (red: Mo_xC, blue: surface MoO_x due to naturally-formed oxide), and (d) Pt 4f region of XPS.

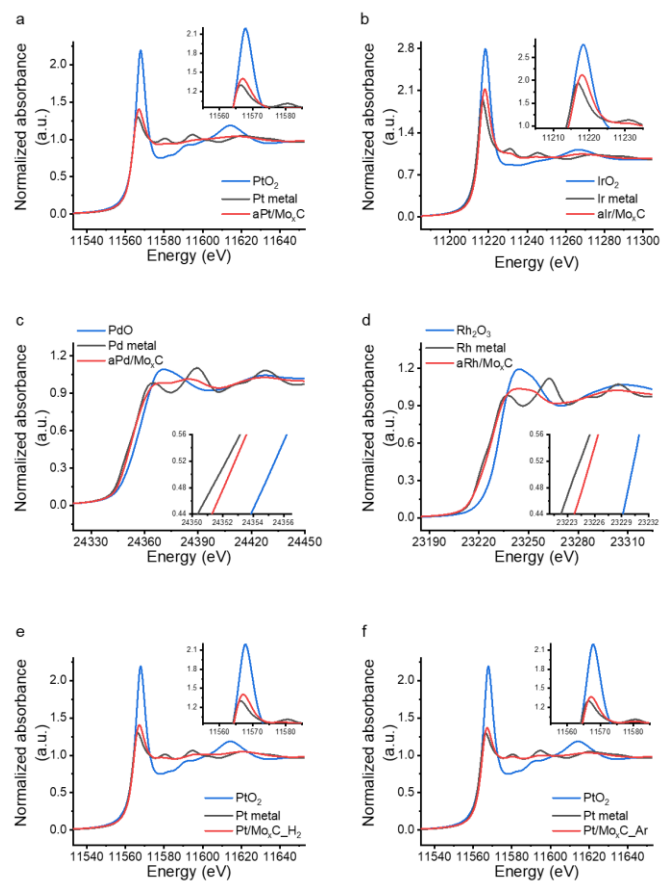


Fig. S51 X-ray absorption near-edge structure (XANES) spectra of the electrocatalysts. XANES spectra of (a-d) aNM/Mo_xC, (e) Pt/Mo_xC-H₂, and (f) Pt/Mo_xC-Ar at the (a, e, f) Pt L₃-edge, (b) Ir L₃-edge, (c) Pd K-edge, and (d) Rh K-edge for NM oxide (blue), NM foil (black), and aNM/Mo_xC (red).

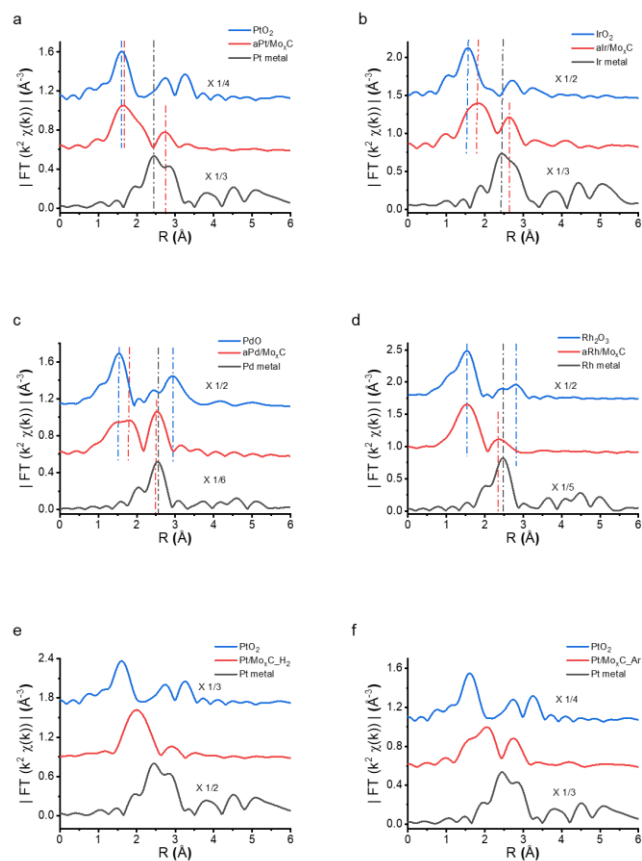


Fig. S52 k^2 -weighted extended X-ray absorption fine structure (EXAFS) Fourier-transform magnitude in the R space ($\chi(R)$) of aNM/Mo_xC. k^2 -weighted FT-EXAFS magnitude in the $\chi(R)$ of (a-d) aNM/Mo_xC, (e) Pt/Mo_xC-H₂, and (f) Pt/Mo_xC-Ar at the (a, e, f) Pt L₃-edge, (b) Ir L₃-edge, (c) Pd K-edge, and (d) Rh K-edge for NM oxide (blue), NM foil (black), and aNM/Mo_xC (red).

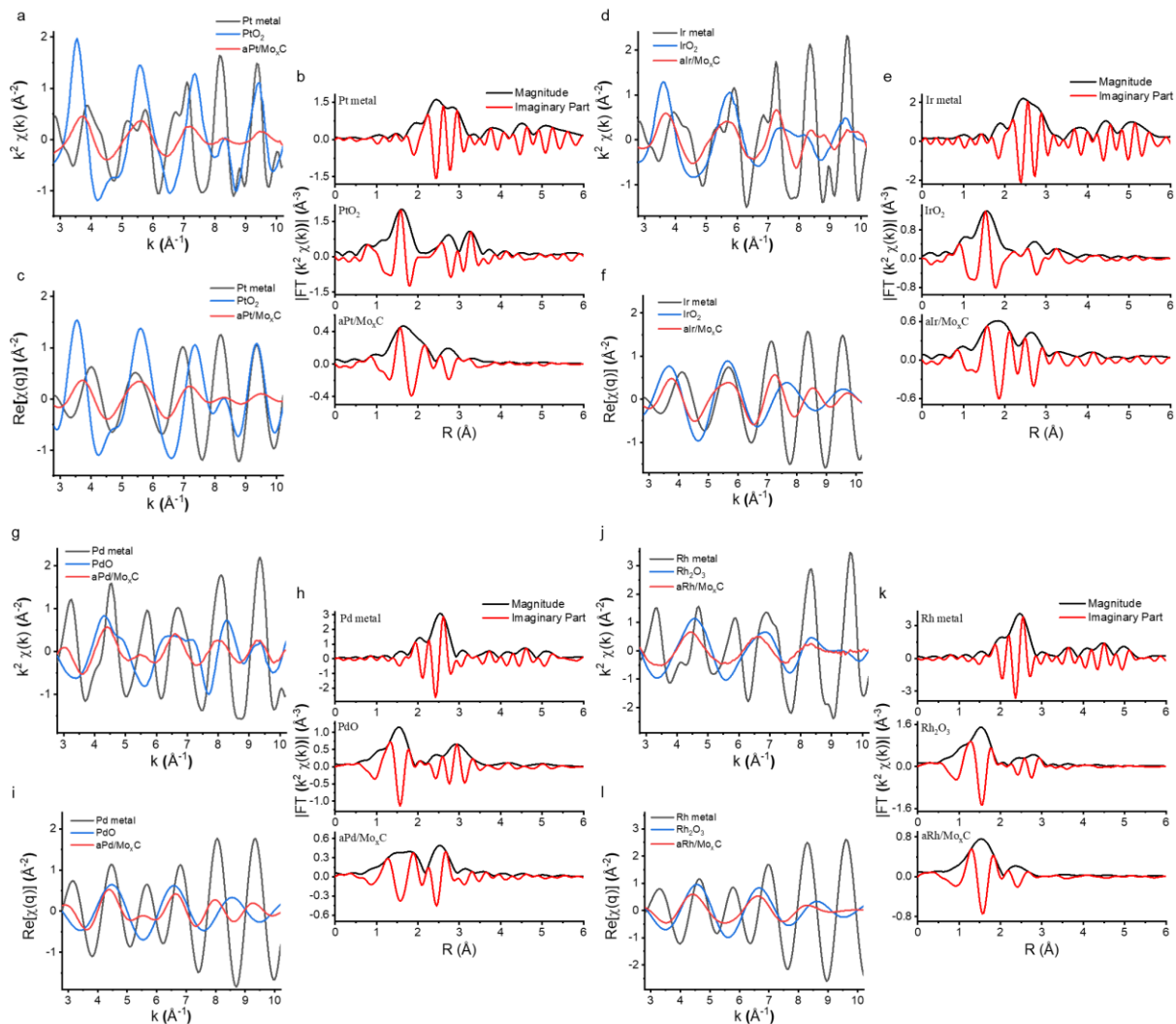


Fig. S53 EXAFS analysis results for NM, NM oxide, and aNM/Mo_xC. (a, d, g, j) $k^2\chi(k)$ oscillations, (b, f, h, k) k^2 -weighted $\chi(R)$, and (c, e, i, l) real part of the back Fourier-transform magnitude in the q space ($\text{Re}[\chi(q)]$) at the (a-c) Pt L₃-edge, (d-f) Ir L₃-edge, (g-i) Pd K-edge, and (j-l) Rh K-edge.

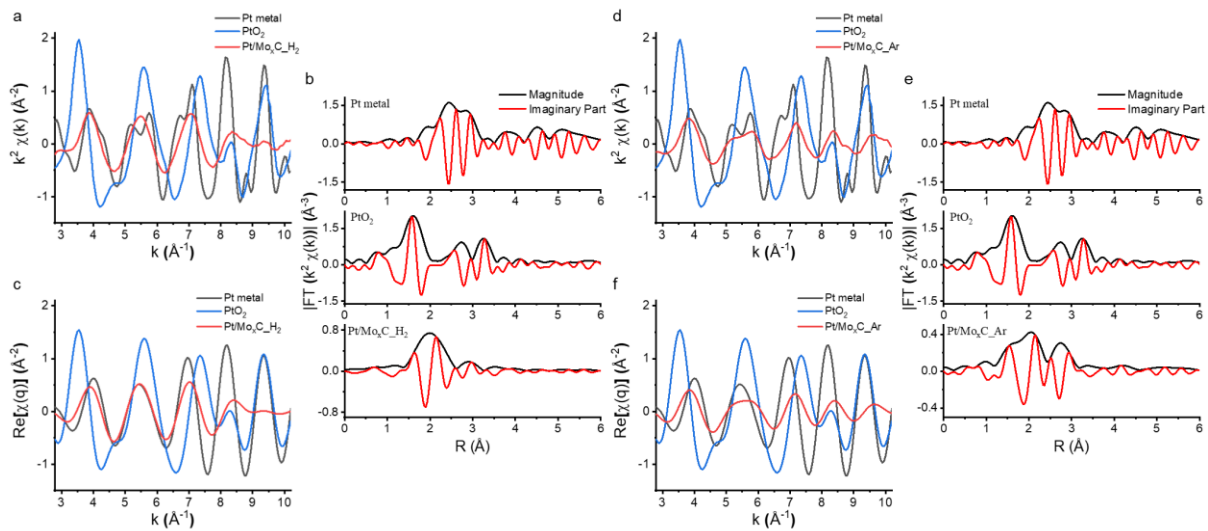


Fig. S54 EXAFS analysis of Pt metal, PtO₂, Pt/Mo_xC_{H₂}, and Pt/Mo_xC_{Ar}. (a, d) $k^2\chi(k)$ oscillations, (b, e) k^2 -weighted $\chi(R)$, and (c, f) real part of back Fourier transform magnitude in q space ($\text{Re}[\chi(q)]$) at Pt L₃-edge for (a-c) Pt/Mo_xC_{H₂}, and (d-f) Pt/Mo_xC_{Ar}.

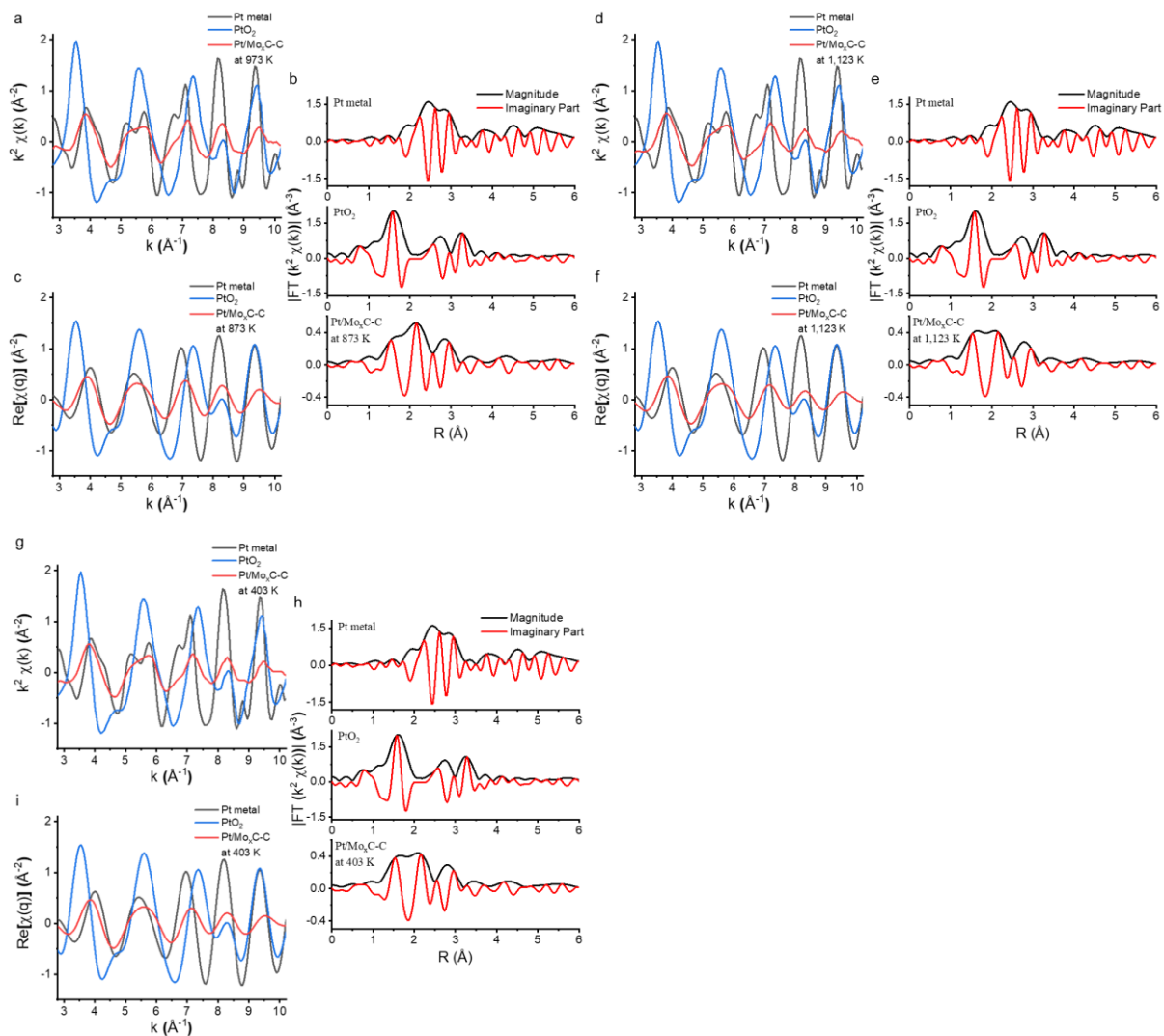


Fig. S55 EXAFS analysis of Pt metal, PtO₂, and Pt/Mo_xC-C at 873 K, 1,123 K, 403 K. (a, d, g) $k^2\chi(k)$ oscillations, (b, e, h) k^2 -weighted $\chi(R)$, and (c, f, i) real part of back Fourier transform magnitude in q space ($\text{Re}[\chi(q)]$) at Pt L₃-edge for (a-c) Pt/Mo_xC-C at 873 K, (d-f) Pt/Mo_xC-C at 1,123 K, and (g-i) Pt/Mo_xC-C at 403 K.

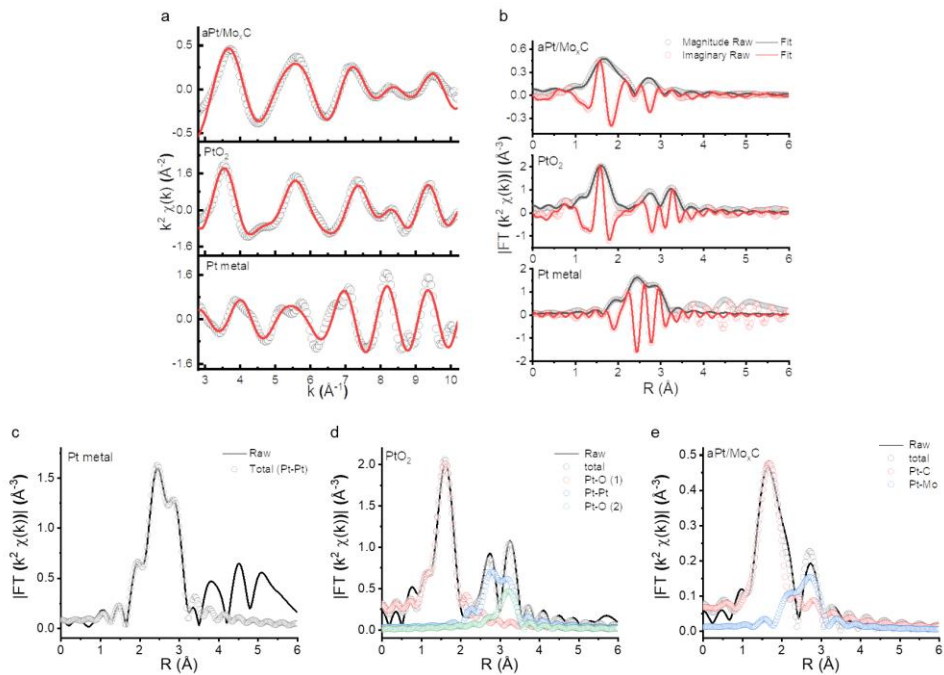


Fig. S56 EXAFS experimental and fitted data. Pt L₃-edge EXAFS experimental (dotted line) and fitted data (solid line) for aPt/Mo_xC, PtO₂, and Pt foil in (a) k space, and (b) R space. Also, raw (solid line) and deconvoluted path for fitted data (dotted line) for (c) Pt foil, (d) PtO₂, and (e) aPt/Mo_xC.

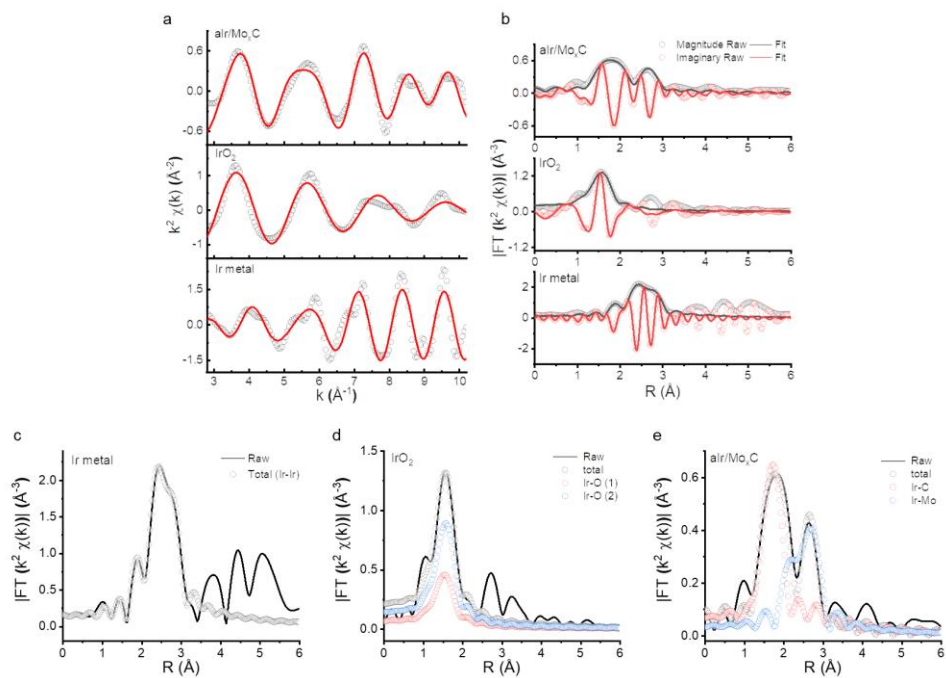


Fig. S57 EXAFS experimental and fitted data. Ir L_3 -edge EXAFS experimental (dotted line) and fitted data (solid line) for alr/Mo_xC , IrO_2 , and Ir foil in (a) k space, and (b) R space. Also, raw (solid line) and deconvoluted path for fitted data (dotted line) for (c) Ir foil, (d) IrO_2 , and (e) alr/Mo_xC .

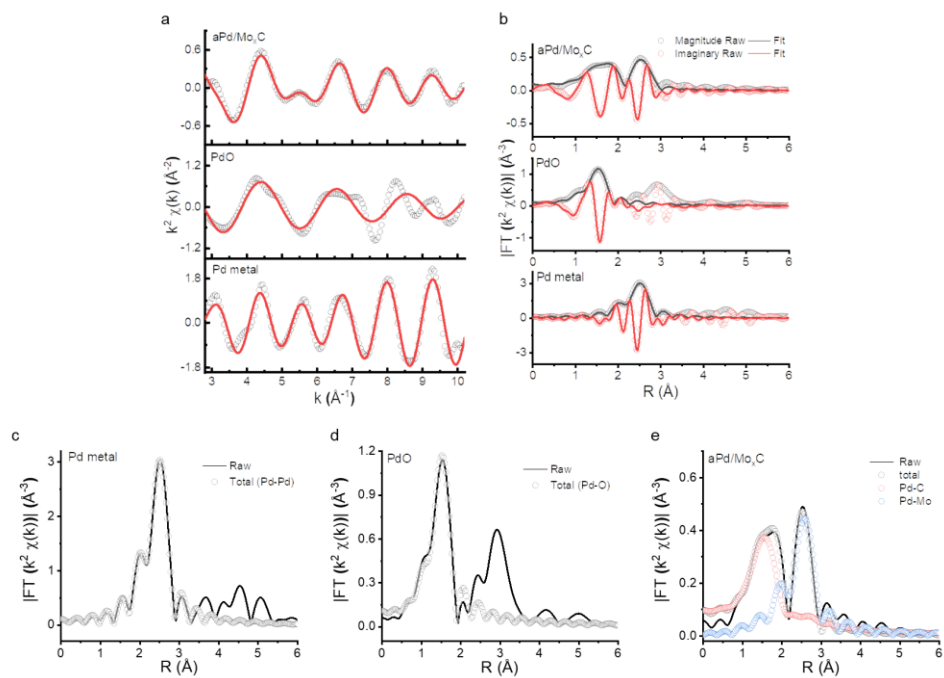


Fig. S58 EXAFS experimental and fitted data. Pd K-edge EXAFS experimental (dotted line) and fitted data (solid line) for aPd/Mo_xC, PdO, and Pd foil in (a) k space, and (b) R space. Also, raw (solid line) and deconvoluted path for fitted data (dotted line) for (c) Pd foil, (d) PdO, and (e) aPd/Mo_xC.

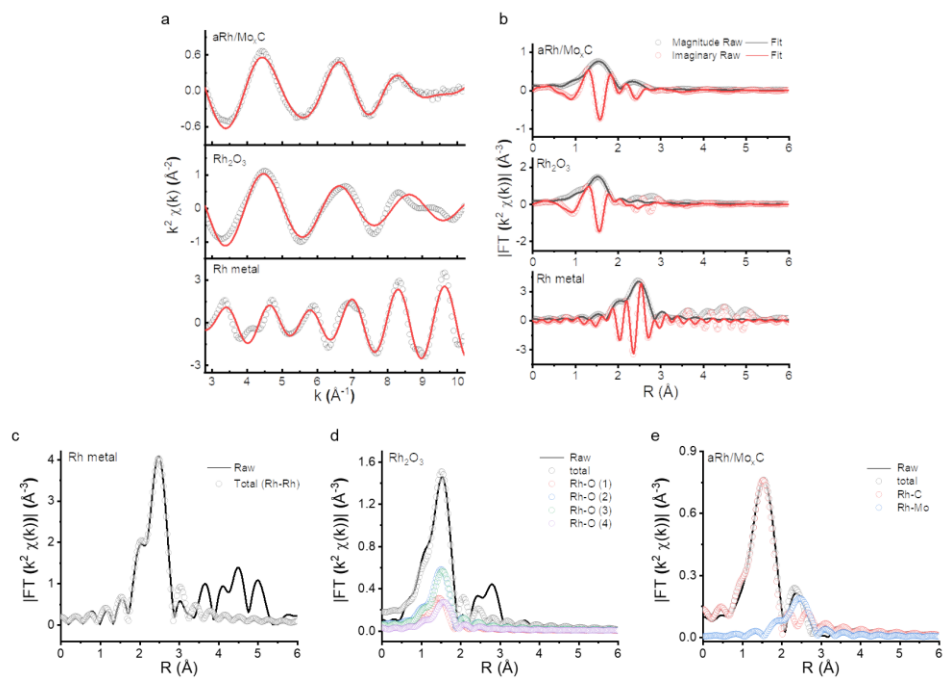


Fig. S59 EXAFS experimental and fitted data. Rh K-edge EXAFS experimental (dotted line) and fitted data (solid line) for aRh/Mo_xC, Rh₂O₃, and Rh foil in (a) k space, and (b) R space. Also, raw (solid line) and deconvoluted path for fitted data (dotted line) for (c) Rh foil, (d) Rh₂O₃, and (e) aRh/Mo_xC.

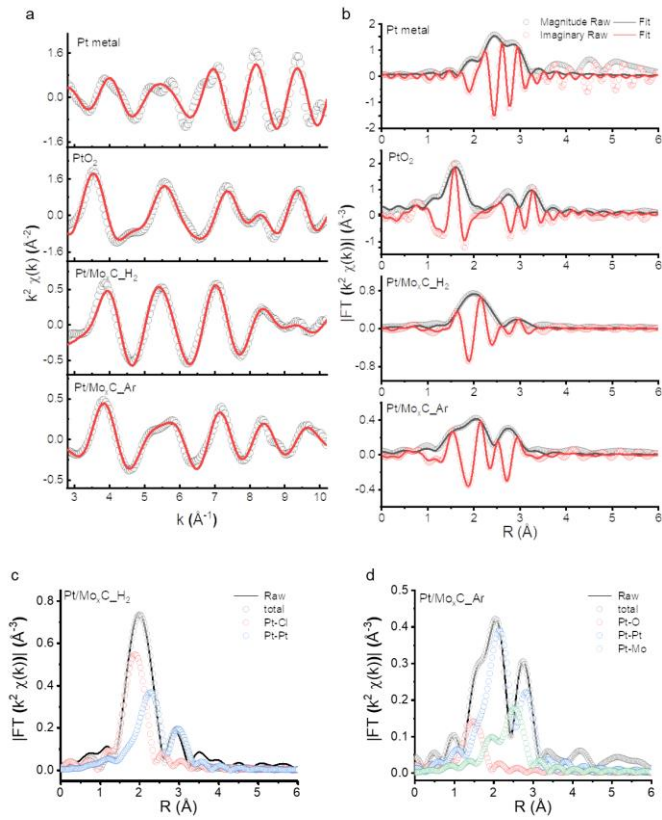


Fig. S60 EXAFS experimental and fitted data. Pt L₃-edge EXAFS experimental (dotted line) and fitted data (solid line) for Pt/Mo_xC_{H₂}, Pt/Mo_xC_{Ar}, PtO₂, and Pt foil in (a) k space, and (b) R space. Also, raw (solid line) and deconvoluted path for fitted data (dotted line) for (c) Pt/Mo_xC_{H₂}, and (d) Pt/MoC_{Ar}

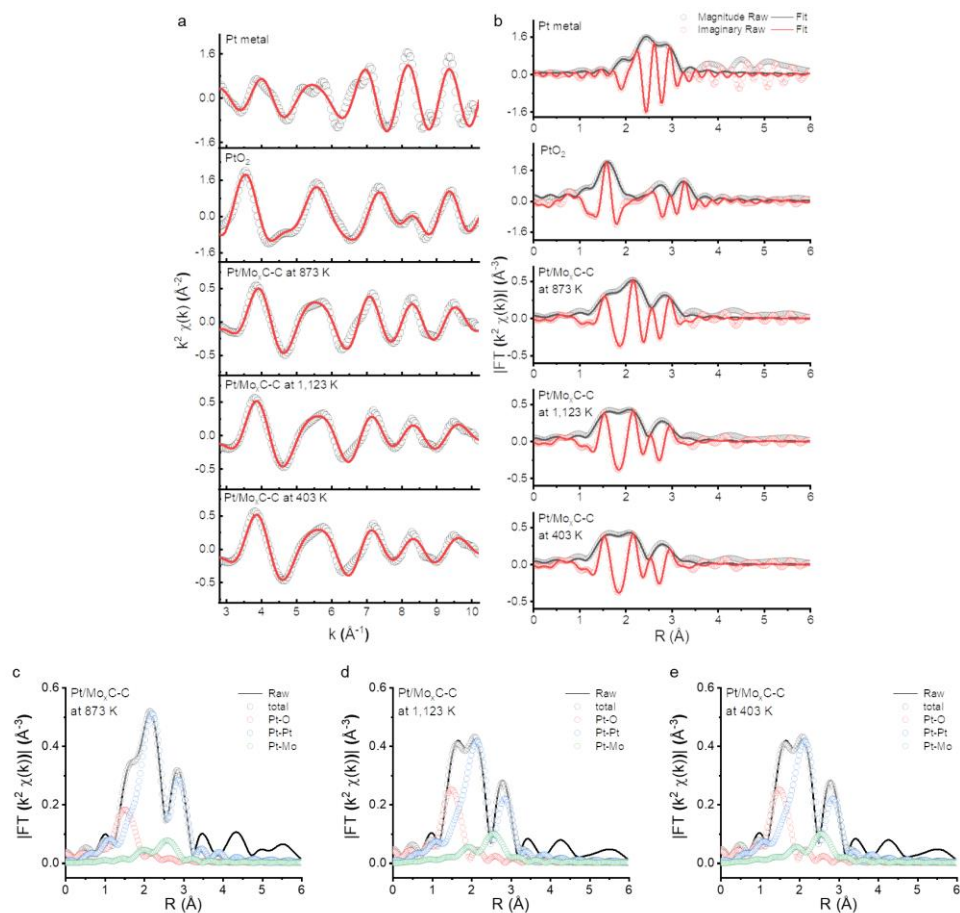


Fig. S61 EXAFS experimental and fitted data. Pt L₃-edge EXAFS experimental (dotted line) and fitted data (solid line) for Pt/Mo_xC-C at 873 K, Pt/Mo_xC-C at 1,123 K, Pt/Mo_xC-C at 403 K, PtO₂, and Pt foil in (a) k space, and (b) R space. Also, raw (solid line) and deconvoluted path for fitted data (dotted line) for (c) Pt/Mo_xC-C at 873 K, (d) Pt/Mo_xC-C at 1,123 K, and (e) Pt/Mo_xC-C at 403 K.

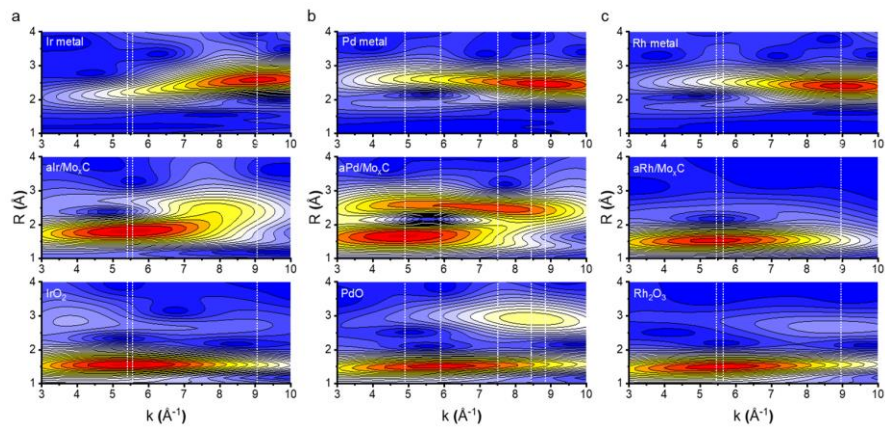


Fig. S62 Wavelet transformations of NM metal, aNM/Mo_xC, and NM oxide. Wavelet transforms for the k^2 -weighted EXAFS oscillations of (a) Ir L₃-edge (Ir foil, aIr/Mo_xC, IrO₂), (b) Pd K-edge (Pd foil, aPd/Mo_xC, PdO), and (c) Rh K-edge (Rh foil, aRh/Mo_xC, Rh₂O₃).

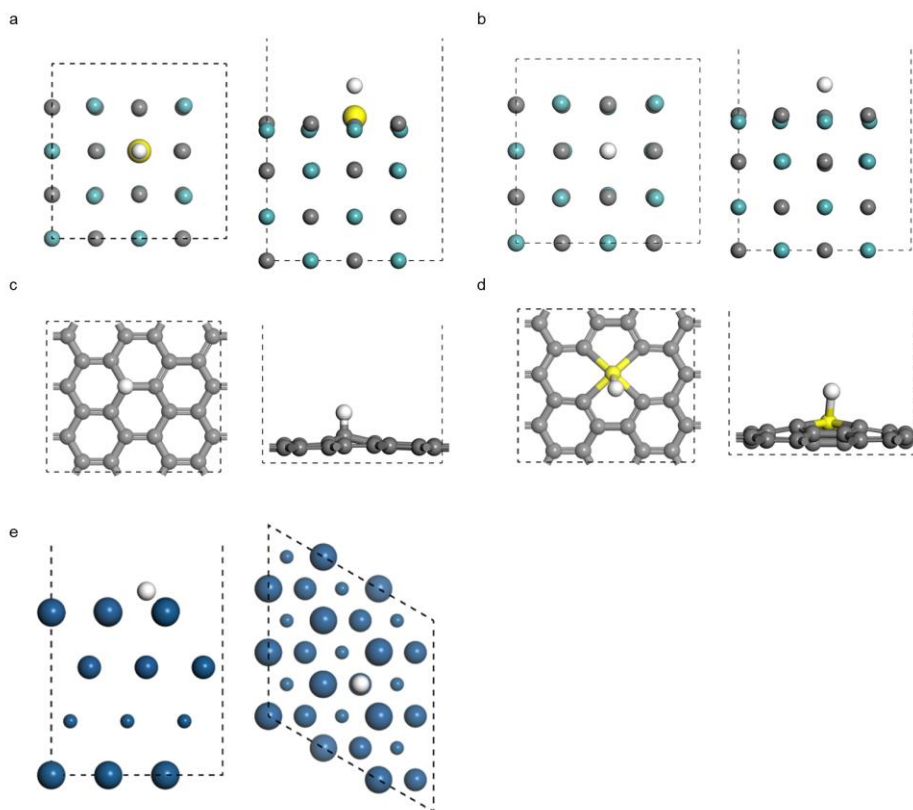


Fig. S63 DFT models for *H binding. DFT models for calculating the hydrogen binding energy on (a) Pt on α -MoC (100), (b) α -MoC (100), (c) graphene, (d) Pt on graphene, and (e) Pt (111).

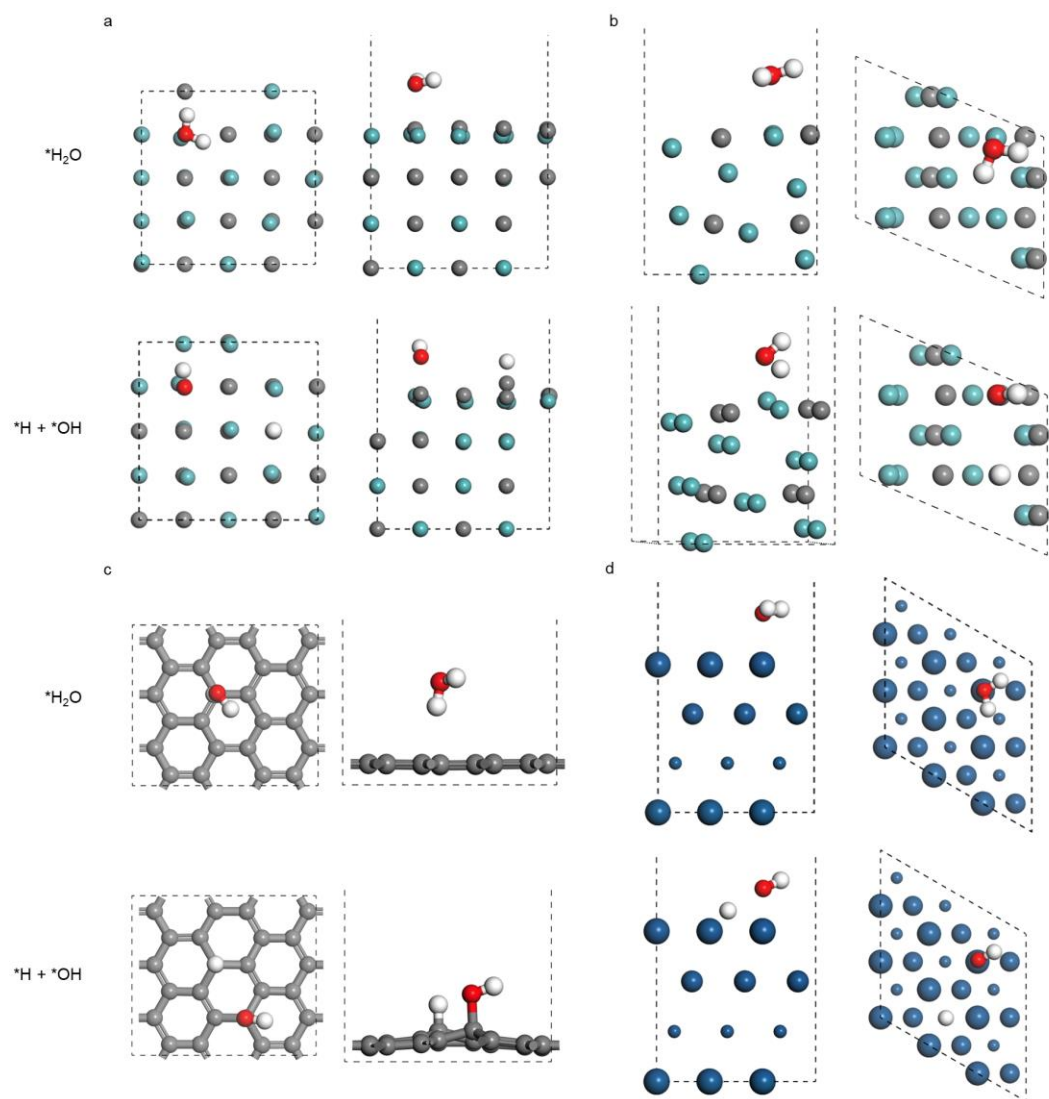


Fig. S64 DFT models *H_2O and $^*H + ^*OH$ binding. DFT models for calculating E_b of *H_2O , $^*H + ^*OH$, and water dissociation barrier on (a) α -MoC (100), (b) β -Mo₂C, (c) graphene, and (d) Pt (111).

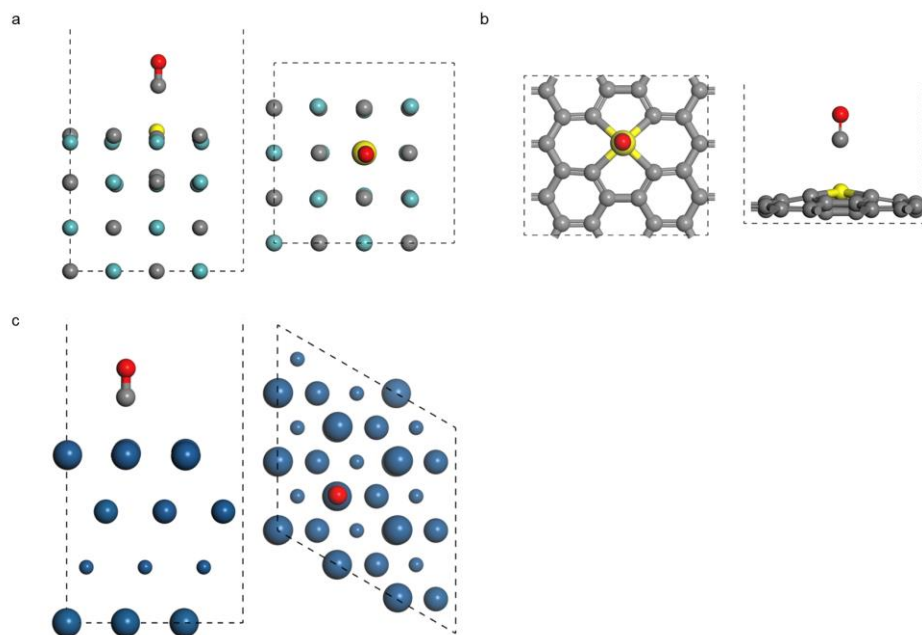


Fig. S65 DFT models for *CO binding. DFT models for calculating the CO binding energy on (a) Pt on α -MoC (100), (b) Pt on graphene, and (c) Pt (111).

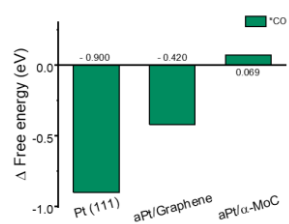


Fig. S66 CO binding energies. CO binding free energies to Pt (111), atomically dispersed Pt on graphene (aPt/Graphene), and atomically dispersed Pt on α -MoC (aPt/ α -MoC).

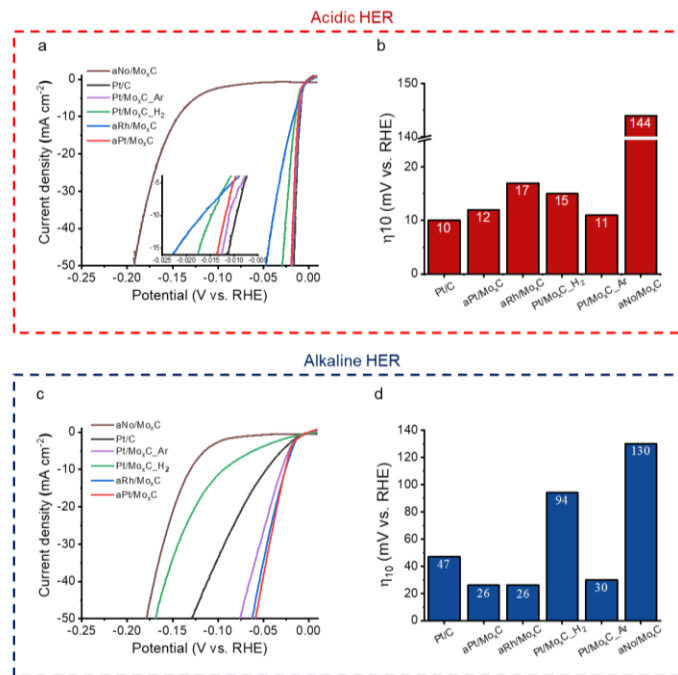


Fig. S67 HER activity of catalysts. (a) Linear sweep voltammetry (LSV) and (b) overpotential for $-10 \text{ mA}\cdot\text{cm}^{-2}$ (η_{10} , mV vs. RHE) for HER in H_2 -saturated $0.5 \text{ M H}_2\text{SO}_4$ solution. (c) LSV and (d) η_{10} for HER in H_2 -saturated 1 M KOH solution.

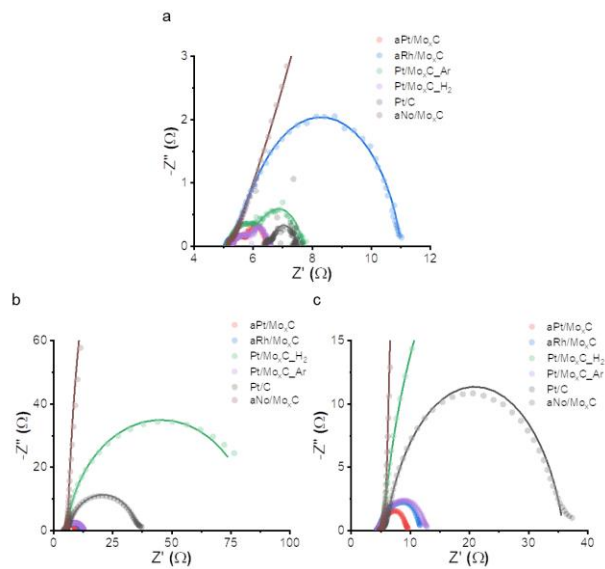


Fig. S68 Electrochemical impedance spectroscopy for HER. Electrochemical impedance spectroscopy (EIS) Nyquist plot at -40 mV in (a) H_2 -saturated $0.5\text{ M } H_2SO_4$ solution, and (b) 1 M KOH solution with (c) corresponding enlarged graph.

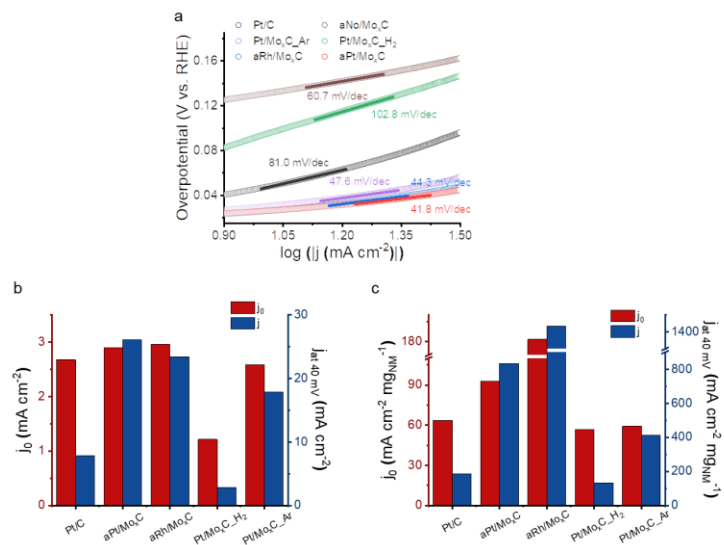


Fig. S69 Alkaline HER activity of catalysts. (a) Tafel plot, (b) exchange current density (j_0 , red) and current density at -40 mV (vs. RHE) (j_{40} , blue) and (c) j_0 (red) and j_{40} per milligram of NM (blue) for HER in H₂-saturated 1 M KOH solution.

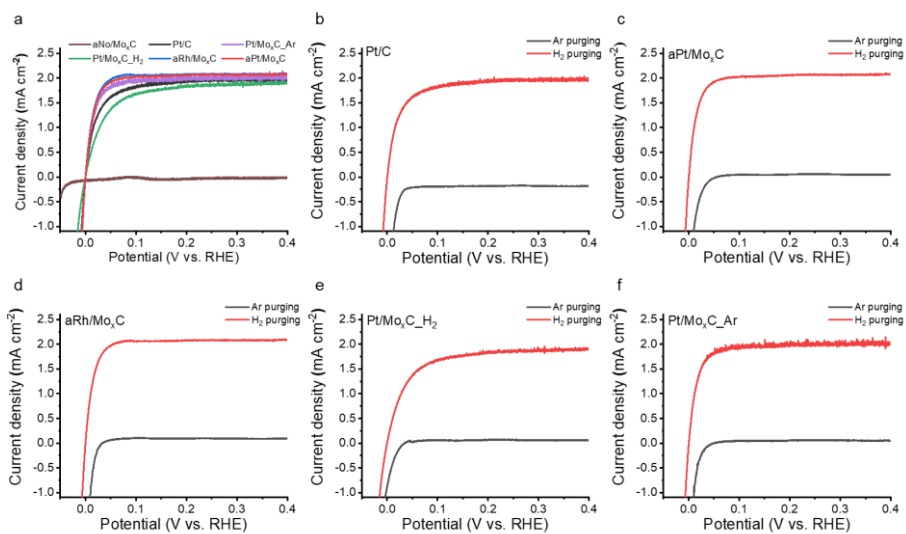


Fig. S70 Alkaline HOR activity of catalysts. (a) LSV in 1 M KOH solution with H₂-saturated condition for alkaline HOR, and (b-f) LSV curves in 1 M KOH solution with (red) H₂-saturated and (black) Ar-saturated condition for (b) commercial Pt/C, (c) aPt/Mo_xC, (d) aRh/Mo_xC, (e) Pt/Mo_xC_H₂, and (f) Pt/Mo_xC_Ar to distinguish the non-Faradaic current density of HOR.

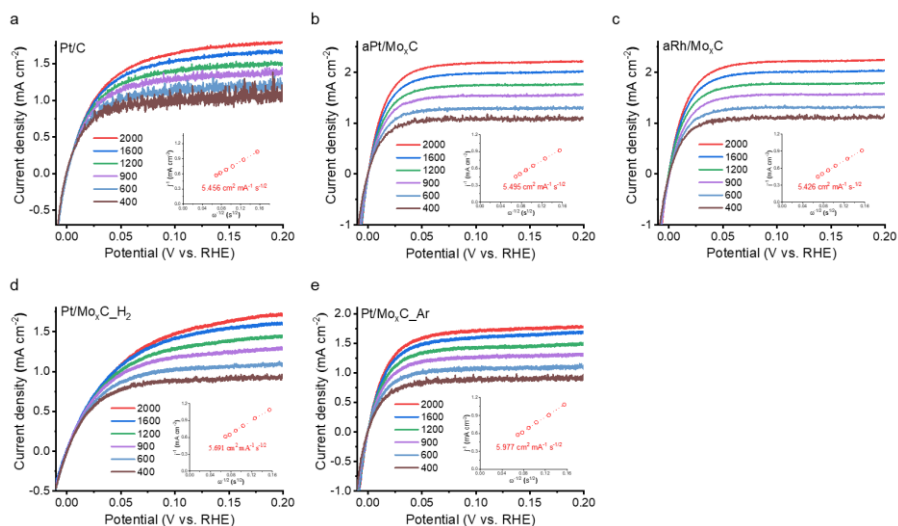


Fig. S71 Koutecky-Levich plot for alkaline HOR. LSV curves at different rotation rates, and (inlet) corresponding Koutecky-Levich plot at 150 mV (vs. RHE) in H₂-saturated 1 M KOH solution for (a) commercial Pt/C, (b) aPt/Mo_xC, (c) aRh/Mo_xC, (d) Pt/Mo_xC_H₂, and (e) Pt/Mo_xC_Ar.

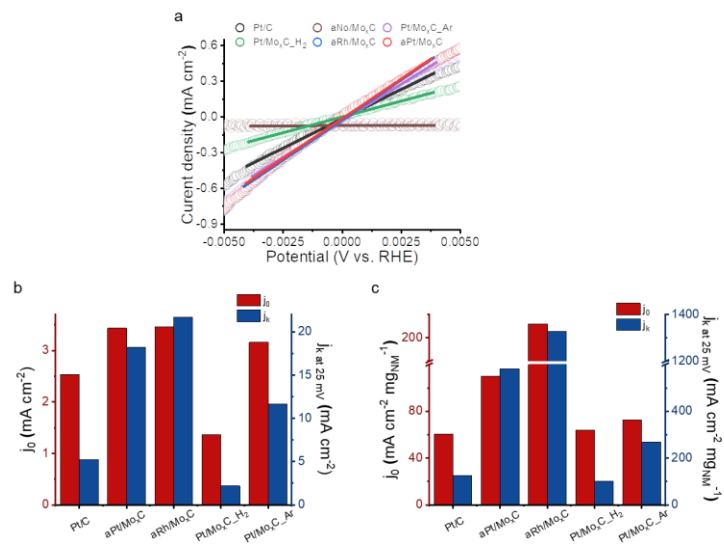


Fig. S72 Alkaline HOR activity of catalysts. (a) LSV curves of micropolarization region (-5 to +5 mV vs. RHE) in H₂-saturated 1 M KOH solution. (b) j_0 (red) and kinetic current density at 25 mV (vs. RHE) (j_k at 25 mV, blue), and (c) j_0 (red) and j_k at 25 mV per milligram of NM (blue).

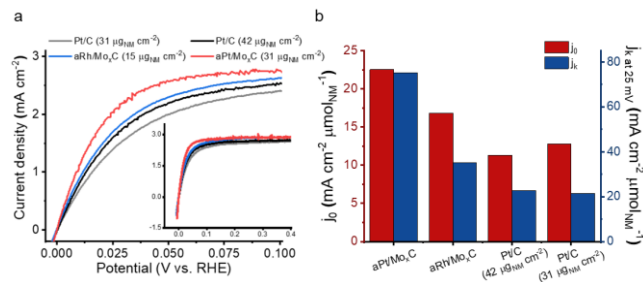


Fig. S73 Alkaline HOR activity of the catalysts. (a) LSV curves, (b) exchange current density (j_0 , red), and kinetic current density at 25 mV ($j_{k, \text{at } 25 \text{ mV}}$, blue) in a 0.1 M KOH solution saturated with H_2 for the alkaline HOR.

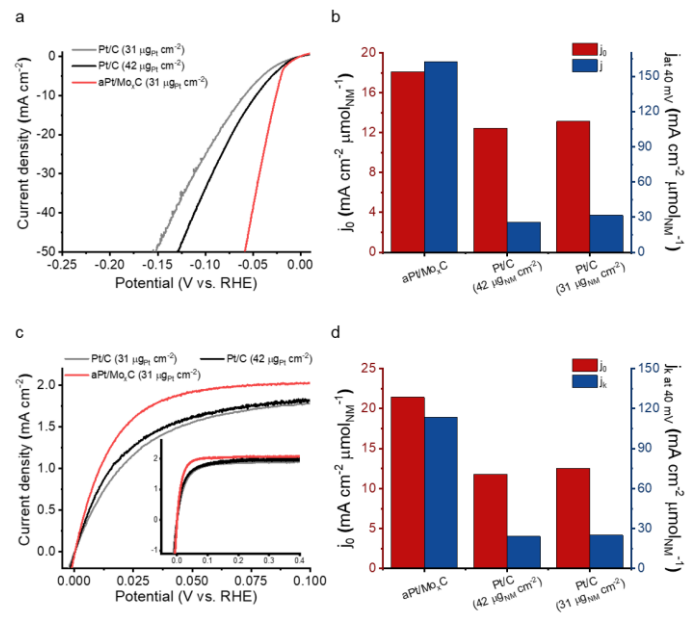


Fig. S74 Alkaline HER and HOR activities of the catalysts with similar Pt loadings. (a, c) LSV curves, (b) exchange current density (j_0 , red) and current density at 25 mV ($j_{at 25mV}$, blue), and (d) j_0 (red) and kinetic current density at 25 mV (j_k at 25 mV, blue) in a 1 M KOH solution saturated with H_2 for the alkaline HER and HOR.

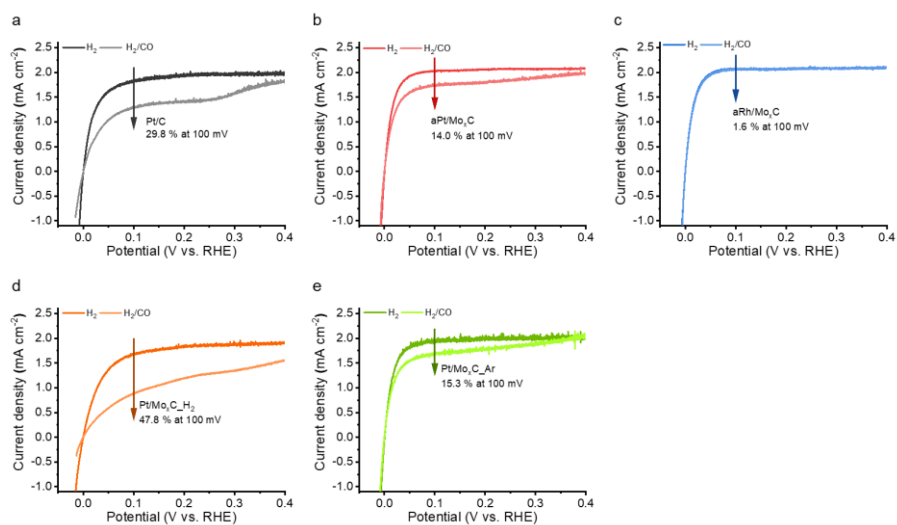


Fig. S75 The effect of CO poisoning in alkaline HOR activity. LSV curves for HOR in 1 M KOH solution with H₂-saturated (deep color) and 1,000 ppm CO/H₂-saturated condition (light color) for (a) aPt/Mo_xC, (b) aRh/Mo_xC, (c) Pt/Mo_xC_{H₂}, (d) Pt/Mo_xC_{Ar}, and (e) commercial Pt/C with percent current density decrease with the presence of 1,000 ppm CO.

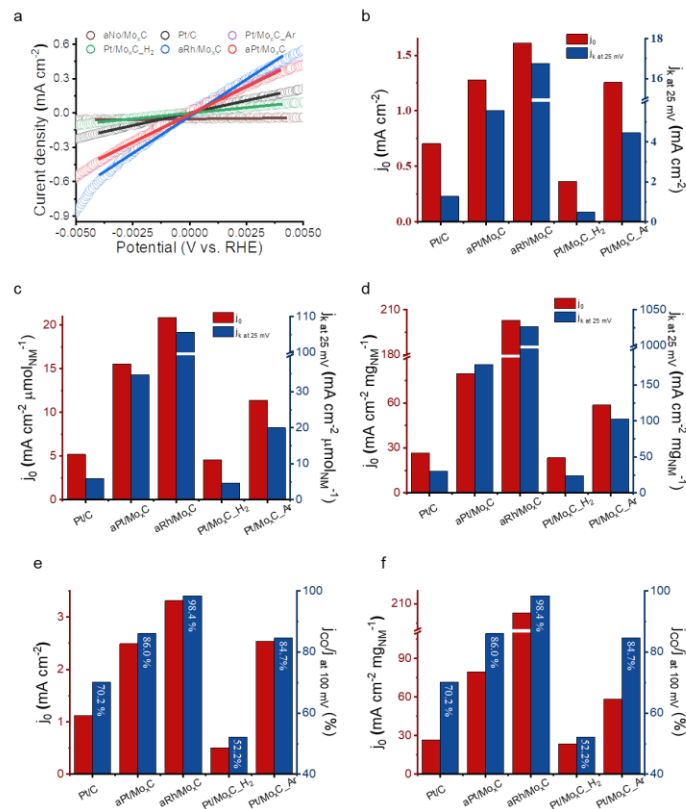


Fig. S76 Alkaline HOR activity with the presence of CO poisoning. (a) LSV curves of micropolarization region (-5 to +5 mV vs. RHE) in 1,000 ppm CO/H₂-saturated 1 M KOH solution. (b) j_0 (red) and j_k at 25 mV (blue), (c) those per micromole of NM, and (d) those per milligram of NM. (e) j_0 (red) with presence of CO, and current density with CO as a percentage (blue) of that without CO at 100 mV (vs. RHE) ($j_{CO}/j_{at\ 100\ mV}$), and (f) those per milligram of NM.

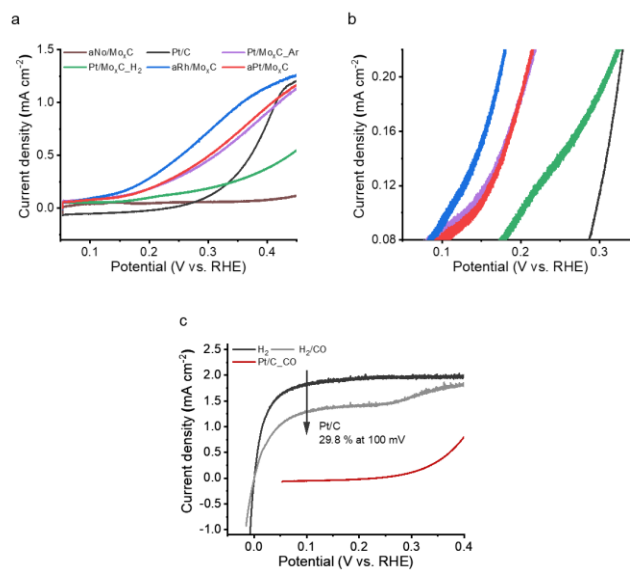


Fig. S77 Electrochemical CO oxidation activity of catalysts. (a) LSV curves for CO oxidation in CO-saturated 1 M KOH solution, and (b) corresponding enlarged graph to verify the onset potential. (c) LSV curves of commercial Pt/C in 1 M KOH solution with H₂-saturated (black), 1,000 ppm CO/H₂-saturated, and CO-saturated condition to identify the effect of CO removal by electrochemical CO oxidation.

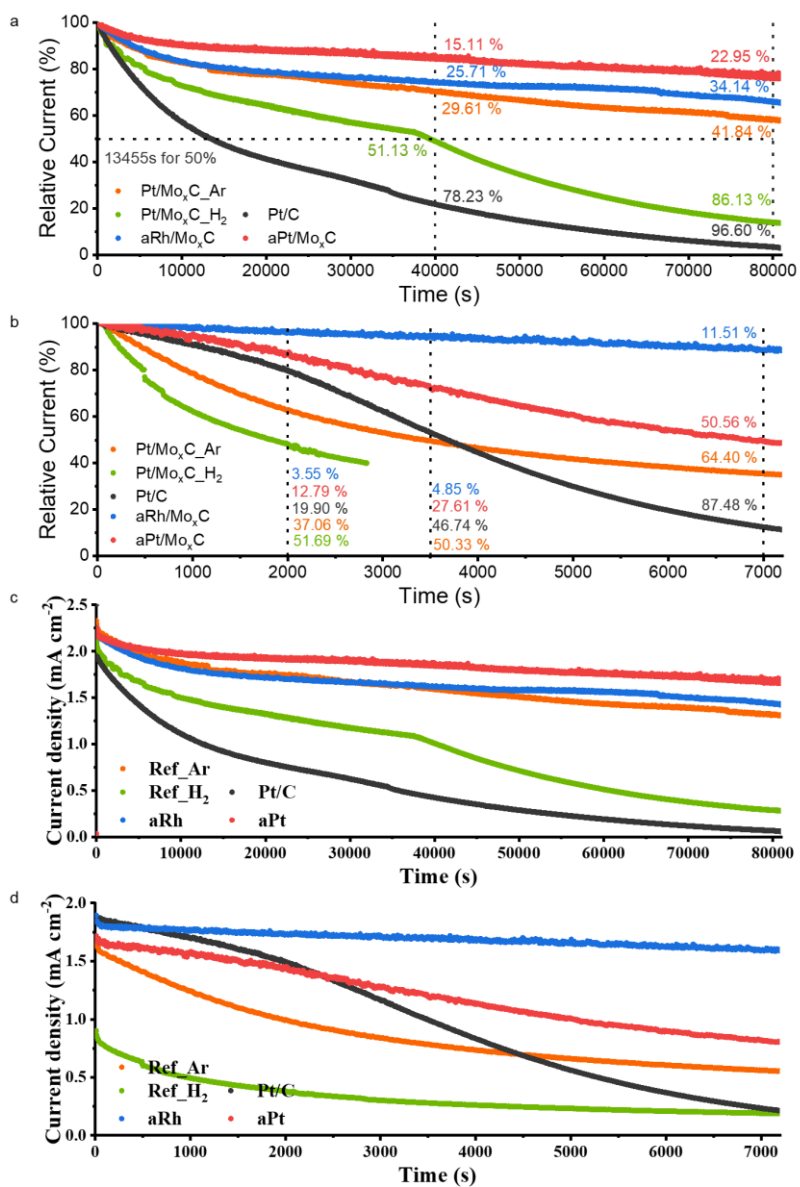


Fig. S78 Electrochemical HOR stability and CO tolerance of the catalysts. Relative current density (%) during chronoamperometry at 100 mV (vs. RHE) in H₂-saturated 1 M KOH solution (a) without and (b) with 1,000 ppm CO. Corresponding current density in the H₂-saturated 1 M KOH solution (c) without and (d) with 1,000 ppm CO.

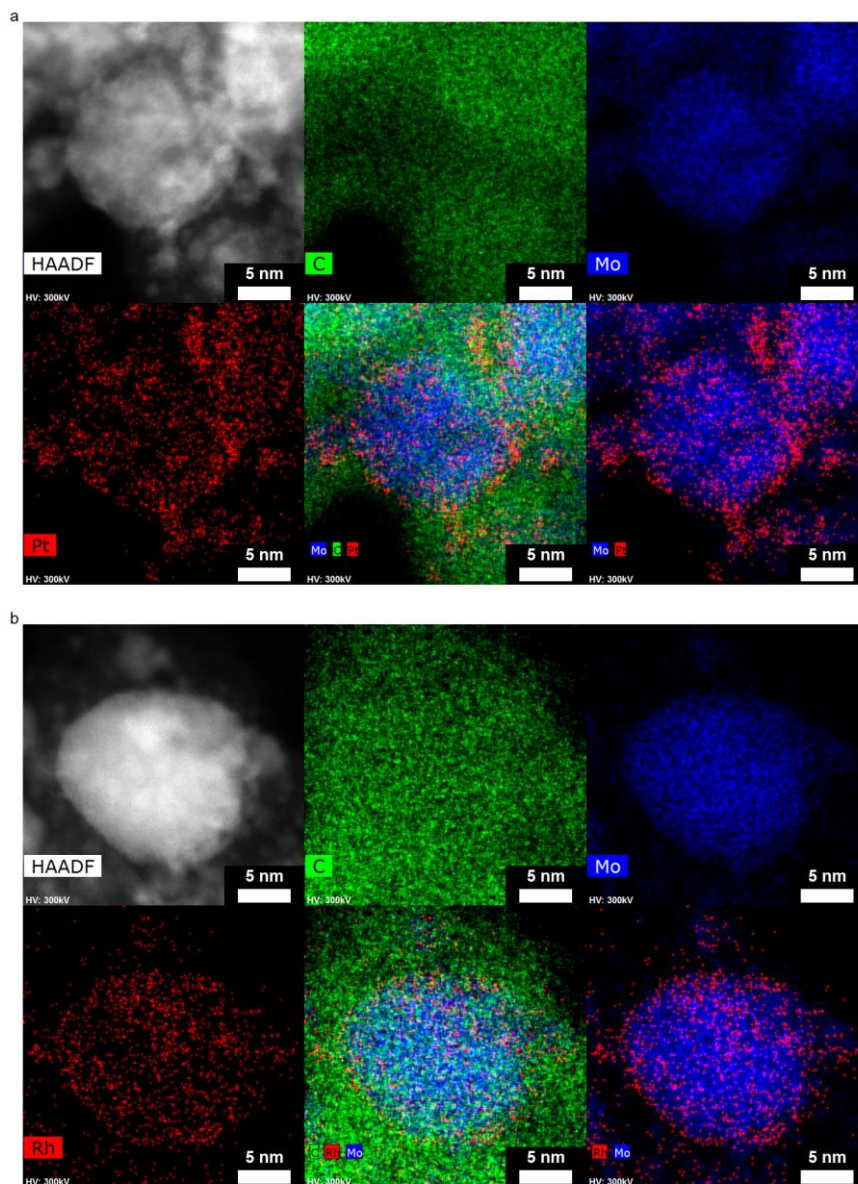


Fig. S79 STEM results for aNM/Mo_xC after the stability tests in RDE experiments. HAADF-STEM images and corresponding EDS mappings for (a) aPt/Mo_xC and (b) aRh/Mo_xC displaying C, Mo, Pt, or Rh and their overlap (red: Pt or Rh, blue: Mo, and green: C).

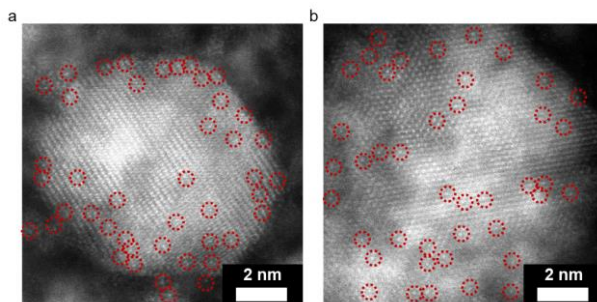


Fig. S80 Z-contrast images of aNM/Mo_xC post-stability tests in RDE experiments. HAADF-STEM images of (a) aPt/Mo_xC and (b) aRh/Mo_xC (red circle: NM ADCs).

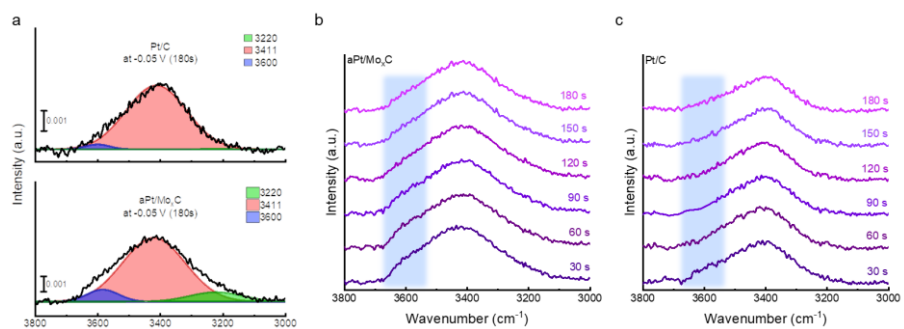


Fig. S81 *In situ* ATR-SEIRAS results, coupled with chronoamperometry. *In situ* ATR-SEIRAS results, coupled with chronoamperometry (a) at -0.05 V (vs. RHE) after 180 s, or at 30 to 180 s for (b) aPt/Mo_xC, and (c) Pt/C.

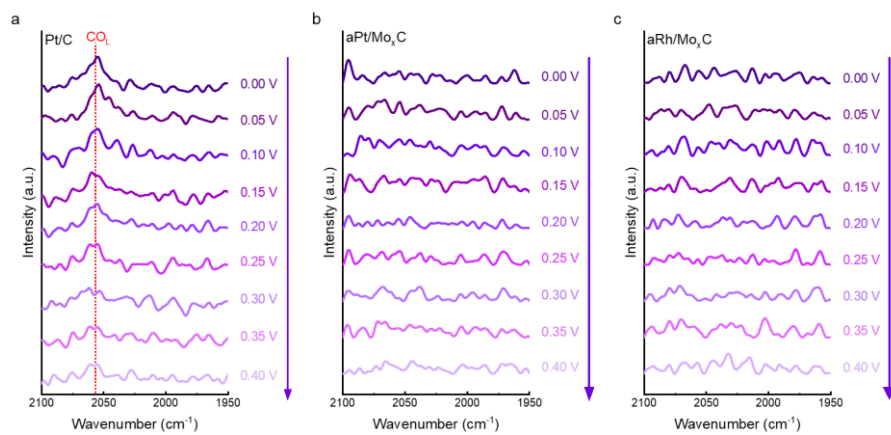


Fig. S82 *In situ* ATR-SEIRAS results, coupled with LSV. *In situ* ATR-SEIRAS results, coupled with LSV at potential of 0.00 to 0.40 V (vs. RHE) in CO-saturated condition for (a) Pt/C, (b) aPt/Mo_xC, (c) aRh/Mo_xC.

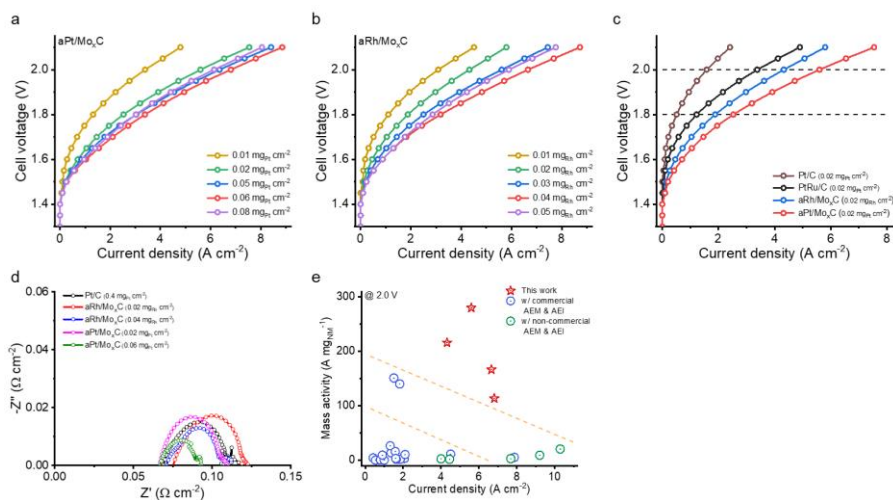


Fig. S83 AEMWE performances. Polarization curves with different NM loading at cathode for (a) aPt/Mo_xC, and (b) aRh/Mo_xC. (c) Polarization curves of commercial and synthesized catalysts with same Pt loading (0.020 mg_{Pt} cm⁻²). (d) EIS Nyquist plot of AEMWEs at 1.8 V_{cell}. (e) Comparison of current density and mass activity for NM of AEMWEs at 2.0 V_{cell}.

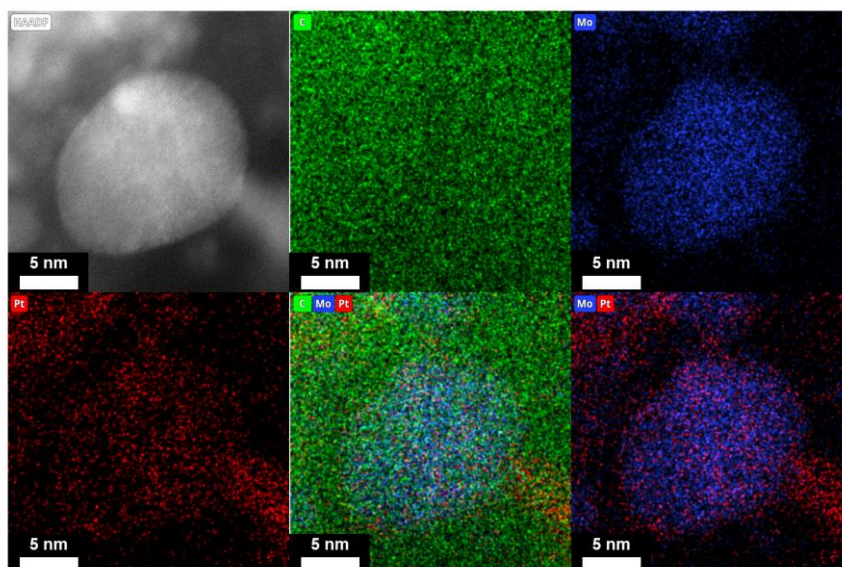


Fig. S84 STEM results for aPt/Mo_xC after performing stability tests in single-cell experiments. HAADF-STEM images and corresponding EDS mappings for aPt/Mo_xC displaying C, Mo, Pt, and their overlap (red: Pt, blue: Mo, and green: C).

Supplementary Tables

Table S1 Metal contents before and after high-*T* carburization. Inductively-coupled plasma mass spectroscopy (ICP-MS results of the Pt and Mo metal weight compositions and ratios for (a) Pt/Mo_xC-C at 403 K and (b) aPt/Mo_xC.

Catalysts	Pt/Mo _x C-C at 403 K	aPt/Mo _x C
Pt (wt%)	3.942	5.071
Mo (wt%)	44.05	54.56
Molar ratio of Pt to Mo (%)	5.502	5.715

Table S2 Relative binding energy of various NM according to type of supports. Relative binding energy E_b of various NMs (Pd, Rh, Pt, Ir, Au, and Ag) with respect to their cohesive energies on Mo_xC (α -MoC, defective α -MoC, β -Mo₂C, and defective β -Mo₂C) and graphite surfaces.

Support	Metal species					
	Pd	Rh	Pt	Ir	Au	Ag
α -MoC	0.974	0.915	0.918	0.822	0.718	0.650
defective α -MoC	1.070	1.061	0.998	0.969	0.971	0.837
β -Mo ₂ C	1.204	1.164	1.062	1.061	0.927	1.006
defective β -Mo ₂ C	1.497	1.369	1.332	1.241	1.183	1.151
Graphite	0.341	0.321	0.391	0.293	0.163	0.144

Table S3 Diffusion barrier of NM ADCs into lattices of Mo_xC support. Diffusion barrier (eV) of NM (Pt, Ir, Rh, and Pd) from topmost surface to bottom layers of Mo_xC (α : α -MoC, β : β -Mo₂C). (see Fig. S12 for DFT models employed).

phase	Metal species							
	Pt		Rh		Pd		Ir	
	α	β	α	β	α	β	α	β
1 st	1.88	3.95	1.31	4.00	2.53	4.41	0.44	3.68
2 nd	5.42	5.36	4.27	4.82	5.72	5.55	3.97	4.57

Table S4 Metal contents for each sample. Metal weight composition using inductively-coupled plasma mass spectroscopy (ICP-MS) of aNM/Mo_xC, Pt/Mo_xC_H₂, and Pt/Mo_xC_Ar.

NM Contents	Catalysts					
	aPt/Mo _x C	alr/Mo _x C	aPd/Mo _x C	aRh/Mo _x C	Pt/Mo _x C_H ₂	Pt/Mo _x C_Ar
wt %	5.21	4.27	3.56	2.72	3.57	7.23

Table S5 Variation of structural parameters of aNM/Mo_xC by dynamic placement. Structural parameters extracted from the Pt L₃-edge, Ir L₃-edge, Pd K-edge, and Rh K-edge EXAFS fitting results. CN: coordination number, R: interatomic distance, σ^2 : Debye-Waller factor (a measure of the static and thermal disorder in absorber-scatterer distances), R-factor is related to the goodness of fit (lower value means goodness). (weighting: k^2)

Sample	Shell	CN	R (Å)	$\sigma^2(10^{-3} \text{ \AA}^2)$	R-factor
Pt	Pt-Pt	12*	2.76 ± 0.00	4.18	0.002
aPt/Mo _x C	Pt-C	3.09 ± 0.30	2.11 ± 0.01	5.82	0.013
	Pt-Mo	0.66 ± 0.18	2.84 ± 0.02	2.50	
PtO ₂	Pt-O	6*	2.01 ± 0.00	2.68	0.008
	Pt-Pt	6*	3.11 ± 0.01	3.25	
	Pt-O	7*	3.67 ± 0.02	2.15	
Ir	Ir-Ir	12*	2.70 ± 0.00	2.34	0.004
aIr/Mo _x C	Ir-C	3.27 ± 0.38	2.13 ± 0.01	2.29	0.013
	Ir-Mo	1.82 ± 0.29	2.81 ± 0.01	3.12	
IrO ₂	Ir-O	2*	1.98 ± 0.00	5.78	0.005
	Ir-O	4*	2.02 ± 0.00		
Pd	Pd-Pd	12*	2.73 ± 0.00	4.94	0.008
aPd/Mo _x C	Pd-C	4.56 ± 0.46	2.15 ± 0.01	13.9	0.008
	Pd-Mo	3.84 ± 0.38	2.79 ± 0.01	10.1	
PdO	Pd-O	4*	2.02 ± 0.01	1.03	0.005
Rh	Rh-Rh	12*	2.68 ± 0.00	2.56	0.004
aRh/Mo _x C	Rh-C	5.08 ± 0.46	2.10 ± 0.01	4.22	0.012
	Rh-Mo	1.00 ± 0.36	2.73 ± 0.02	6.40	
Rh ₂ O ₃	Rh-O	1*	1.95 ± 0.01	1.77	0.008
	Rh-O	2*	2.00 ± 0.01		
	Rh-O	2*	2.04 ± 0.01		
	Rh-O	1*	2.07 ± 0.01		

Structural parameters extracted from the EXAFS fitting of reference metal foil. CN is the coordination number; R is the interatomic distance; σ^2 is the Debye-Waller factor (a measure of the static and thermal disorder in absorber-scatterer distance); ΔE_0 is edge energy shift (the zero kinetic energy difference between experiment and theoretical model); R-factor value is related with the goodness of the fitting.

* Value was assigned in curving fitting based on standard structure

R_{bkg} was set to 1.0 in background removal to remove the noise oscillation below 1 Å in R-space

S_0^2 value was calculated from the fitting of metal foil with standard metal structure

Table S6 Variation of structural parameters of comparison groups by dynamic placement. Structural parameters extracted from the Pt L₃-edge EXAFS fitting results. CN: coordination number, R: interatomic distance, σ^2 : Debye-Waller factor (a measure of the static and thermal disorder in absorber-scatterer distances), R-factor is related to the goodness of fit (lower value means goodness). (weighting: k^2)

Sample	Shell	CN	R (Å)	$\sigma^2 (10^{-3} \text{Å}^2)$	R-factor
Pt	Pt-Pt	12*	2.76 ± 0.00	4.18	0.002
aPt/Mo _x C	Pt-C	3.09 ± 0.30	2.11 ± 0.01	5.82	0.013
	Pt-Mo	0.66 ± 0.18	2.84 ± 0.02	2.50	
PtO ₂	Pt-O	6*	2.01 ± 0.00	2.68	0.008
	Pt-Pt	6*	3.11 ± 0.01	3.25	
	Pt-O	7*	3.67 ± 0.02	2.15	
Pt/Mo _x C_H ₂	Pt-Cl	1.73 ± 0.12	2.31 ± 0.01	6.07	0.004
	Pt-Pt	6.14 ± 0.61	2.75 ± 0.01	12.17	
Pt/Mo _x C_Ar	Pt-O	0.38 ± 0.05	1.94 ± 0.01	0.78	0.002
	Pt-Pt	6.35 ± 0.27	2.68 ± 0.00	11.60	
	Pt-Mo	1.82 ± 0.18	2.70 ± 0.00		
Pt/Mo _x C-C at 873 K	Pt-O	0.61 ± 0.04	1.96 ± 0.01	3.10	0.001
	Pt-Pt	8.05 ± 0.17	2.71 ± 0.02	11.2	
	Pt-Mo	0.77 ± 0.11	2.73 ± 0.02		
Pt/Mo _x C-C at 1,123 K	Pt-O	0.69 ± 0.06	1.94 ± 0.01	0.82	0.002
	Pt-Pt	8.49 ± 0.35	2.69 ± 0.00	14.48	
	Pt-Mo	1.35 ± 0.15	2.71 ± 0.00		
Pt/Mo _x C-C at 423 K	Pt-O	0.78 ± 0.06	1.95 ± 0.01	0.23	0.002
	Pt-Pt	8.01 ± 0.30	2.70 ± 0.00	13.42	
	Pt-Mo	1.32 ± 0.20	2.72 ± 0.00		

Structural parameters extracted from the EXAFS fitting of reference metal foil. CN is the coordination number; R is the interatomic distance; σ^2 is the Debye-Waller factor (a measure of the static and thermal disorder in absorber-scatterer distance); ΔE_0 is edge energy shift (the zero kinetic energy difference between experiment and theoretical model); R-factor value is related with the goodness of the fitting.

* Value was assigned in curving fitting based on standard structure

R_{bkg} was set to 1.0 in background removal to remove the noise oscillation below 1 Å in R-space
 S_0^2 value was calculated from the fitting of metal foil with standard metal structure

Table S7 Adsorbate binding energy for each support. DFT binding energies (eV) of *H₂O, and a pair of hydrogen + hydroxyl group (*H + *OH) on various supports.

	DFT binding energy (eV)	
	*H ₂ O	*H + *OH
Graphene	0.09	2.93
Pt (111)	0.04	1.04
α -MoC (001)	-0.35	-0.24
β -Mo ₂ C (101)	-0.29	-0.35

Table S8 Noble metal loading of the various catalysts for electrochemical RDE experiments.

	Pt/C	aPt/Mo _x C	Pt/Mo _x C_Ar	Pt/Mo _x C_H ₂	aRh/Mo _x C	aNo/Mo _x C
Catalyst mass loading (mg cm ⁻²)	0.210	0.600	0.600	0.600	0.600	0.600
Noble metal mass loading (μg _{NM} cm ⁻²)	42.00	31.26	43.38	21.42	16.32	-
Noble metal molar loading (μmol cm ⁻²)	0.215	0.160	0.222	0.110	0.159	-

Table S9 Charge transfer resistance for each catalyst. Charge transfer resistance (R_{ct}) calculated with EIS measurement at -40 mV (vs. RHE) under acidic and alkaline condition at -40 mV (vs. RHE)

	Catalysts					
	Pt/C	aPt/Mo _x C	aRh/Mo _x C	Pt/Mo _x C_H ₂	Pt/Mo _x C_Ar	aNo/Mo _x C
R_{ct} ($\Omega \cdot \text{cm}^{-2}$) alkaline at 40 mV	30.10	4.864	7.251	79.42	8.05	1125
R_{ct} ($\Omega \cdot \text{cm}^{-2}$) acidic at 40 mV	0.8615	0.7258	5.309	1.484	0.7197	1003

Table S10 Electrochemical performance for the alkaline HER. Electrochemical responses for the HER in H₂-saturated 1 M KOH solution.

Catalysts	η_{10} (mV)	Tafel slope (mV·dec ⁻¹)	J_0 (mA·cm ⁻²)	$J_{at\ 40\ mV}$ (mA·cm ⁻²)
Pt/C	47	81.0	2.675	7.802
Pt/C (31 μg_{Pt} cm ⁻²)	59	86.1	2.085	5.012
aPt/Mo _x C	26	41.8	2.897	26.061
aRh/Mo _x C	26	44.3	2.963	23.373
Pt/Mo _x C_H ₂	94	102.8	1.214	2.835
Pt/Mo _x C_Ar	30	47.6	2.568	17.876
aNo/Mo _x C	130	60.7	-	-

Catalysts	J_0 per NM mol (mA·cm ⁻² · μmol^{-1})	J_0 per NM mass (mA·cm ⁻² ·mg ⁻¹)	$J_{at\ 40mV}$, per NM mol (mA·cm ⁻² · μmol^{-1})	$J_{at\ 40mV}$, per NM mass (mA·cm ⁻² ·mg ⁻¹)
Pt/C	12.425	63.690	36.238	185.762
Pt/C (31 μg_{Pt} cm ⁻²)	13.121	67.258	31.540	161.677
aPt/Mo _x C	18.079	92.674	162.635	833.685
aRh/Mo _x C	18.684	181.556	147.385	1432.169
Pt/Mo _x C_H ₂	11.056	56.676	25.819	132.353
Pt/Mo _x C_Ar	11.548	59.198	80.388	412.079

Table S11 Electrochemical performance in the alkaline HOR. Electrochemical responses for the HOR in H₂-saturated 1 M KOH solution.

Catalysts	$j_{\text{at } 25 \text{ mV}}$ (mA·cm ⁻²)	j_0 (mA·cm ⁻²)	j_k at 25 mV (mA·cm ⁻²)
Pt/C	1.289	2.533	5.227
Pt/C (31 μg _{Pt} cm ⁻²)	1.160	1.992	3.980
aPt/Mo _x C	1.602	3.431	18.175
aRh/Mo _x C	1.646	3.458	21.653
Pt/Mo _x C_H ₂	0.938	1.366	2.180
Pt/Mo _x C_Ar	1.509	3.158	11.630

Catalysts	$j_{\text{at } 25 \text{ mV per NM mol}}$ (mA·cm ⁻² ·μmol ⁻¹)	$j_{\text{at } 25 \text{ mV per NM mass}}$ (mA·cm ⁻² ·mg ⁻¹)	j_0 per NM mol (mA·cm ⁻² ·μmol ⁻¹)	j_0 per NM mass (mA·cm ⁻² ·mg ⁻¹)	j_k at 25 mV, per NM mol (mA·cm ⁻² ·μmol ⁻¹)	j_k at 25 mV, per NM mass (mA·cm ⁻² ·mg ⁻¹)
Pt/C	5.987	30.690	11.765	60.310	24.278	124.452
Pt/C (31 μg _{Pt} cm ⁻²)	7.299	37.414	12.538	64.271	25.043	128.375
aPt/Mo _x C	9.997	51.248	21.411	109.757	113.422	581.414
aRh/Mo _x C	10.379	100.858	21.805	211.887	136.539	1326.777
Pt/Mo _x C_H ₂	8.543	43.791	12.441	63.772	19.854	101.774
Pt/Mo _x C_Ar	6.786	34.786	14.202	72.799	52.300	268.096

Table S12 Electrochemical performance in the alkaline HOR. Electrochemical responses for the HOR in H₂-saturated 0.1 M KOH solution.

Catalysts	$j_{\text{at } 25 \text{ mV}}$ (mA·cm ⁻²)	j_0 (mA·cm ⁻²)	$j_{\text{k at } 25 \text{ mV}}$ (mA·cm ⁻²)
aPt/Mo _x C	2.032	3.611	12.040
aRh/Mo _x C	1.692	2.665	5.552
Pt/C (42 μg _{NM} cm ⁻²)	1.598	2.438	4.881
Pt/C (31 μg _{NM} cm ⁻²)	1.386	2.032	3.418

Catalysts	$j_{\text{at } 25 \text{ mV per NM mol}}$ (mA·cm ⁻² ·μmol ⁻¹)	$j_{\text{at } 25 \text{ mV per NM mass}}$ (mA·cm ⁻² ·mg ⁻¹)	$j_0 \text{ per NM mol}$ (mA·cm ⁻² ·μmol ⁻¹)	$j_0 \text{ per NM mass}$ (mA·cm ⁻² ·mg ⁻¹)	$j_{\text{k at } 25 \text{ mV, per NM mol}}$ (mA·cm ⁻² ·μmol ⁻¹)	$j_{\text{k at } 25 \text{ mV, per NM mass}}$ (mA·cm ⁻² ·mg ⁻¹)
aPt/Mo _x C	12.681	65.003	22.537	115.528	75.138	385.163
aRh/Mo _x C	10.669	103.677	16.806	163.309	35.008	340.183
Pt/C (42 μg _{NM} cm ⁻²)	7.422	38.048	11.323	58.043	22.672	116.218
Pt/C (31 μg _{NM} cm ⁻²)	8.722	44.710	12.790	65.561	21.511	110.265

Table S13 Electrochemical performances in alkaline HOR with the presence of CO poisoner. Electrochemical responses for HOR in the presence of CO (1,000 ppm CO/H₂-saturated 1 M KOH solution).

Catalysts	$j_{\text{at 25 mV}}$ (mA·cm ⁻²)	j_0 (mA·cm ⁻²)	j_k at 25 mV (mA·cm ⁻²)	$(j_{\text{H}_2} - j_{\text{H}_2/\text{CO}}) / j_{\text{H}_2}$ at 100 mV (%)
Pt/C	0.706	1.117	1.274	29.8
aPt/Mo _x C	1.279	2.489	5.565	14.0
aRh/Mo _x C	1.609	3.313	16.749	1.6
Pt/Mo _x C_H ₂	0.363	0.504	0.506	47.8
Pt/Mo _x C_Ar	1.256	2.539	4.453	15.3

Catalysts	$j_{\text{at 25 mV per NM mol}}$ (mA·cm ⁻² ·μmol ⁻¹)	$j_{\text{at 25 mV per NM mass}}$ (mA·cm ⁻² ·mg ⁻¹)	j_0 per NM mol (mA·cm ⁻² ·μmol ⁻¹)	j_0 per NM mass (mA·cm ⁻² ·mg ⁻¹)	j_k at 25 mV, per NM mol (mA·cm ⁻² ·μmol ⁻¹)	j_k at 25 mV, per NM mass (mA·cm ⁻² ·mg ⁻¹)
Pt/C	3.279	16.810	5.188	26.595	5.917	30.333
aPt/Mo _x C	7.981	40.915	15.533	79.623	34.729	178.023
aRh/Mo _x C	10.146	98.591	20.891	203.003	105.615	1026.287
Pt/Mo _x C_H ₂	3.306	16.947	4.590	23.529	4.608	23.623
Pt/Mo _x C_Ar	5.648	28.953	11.418	58.529	20.025	102.651

Table S14 Lennard-Jones FF parameters optimized to simulate α -MoC (100).²⁹

FF parameter	Value
σ (C-C) [Å]	2.2
ϵ (C-C) [eV]	0.095
σ (Mo-Mo) [Å]	2.2
ϵ (Mo-Mo) [eV]	0.095
σ (Mo-C) [Å]	2.2
ϵ (Mo-C) [eV]	0.095

Table S15 Atomic charges of Mo and C assigned for simulating α -MoC (100).³⁰

Species	Charge value
Mo	1.28
C	-1.28

Table S16 Lennard-Jones FF parameters optimized to simulate Pt binding on α -MoC (100) and that on graphene.³¹

FF parameter	Value
α -MoC ~ Pt	
σ (Pt-C) [\AA]	2.273
ϵ (Pt-C) [eV]	0.820
σ (Pt-Mo) [\AA]	2.273
ϵ (Pt-Mo) [eV]	0.820
Graphite ~ Pt	
σ (Pt-C) [\AA]	2.0
ϵ (Pt-C) [eV]	0.300

Table S17 Comparison of the synthesized catalysts with other state-of-the-art catalysts for AEMWEs (marked in yellow: the developed anion-exchange membrane (AEM) and anion-exchange ionomer (AEI) that were used; shaded area: studies that achieved the US DOE's 2026 performance target for PEMWEs (3.0 A cm^{-2} @ $1.8 \text{ V}_{\text{cell}}$)).

Cathode	Membrane electrode assembly (MEA)				Current density (A cm^{-2})		Cell voltage (V_{cell})		Reference
	NM loading ($\text{mg}_{\text{NM}} \text{cm}^{-2}$)	Membrane	Anode	NM loading ($\text{mg}_{\text{NM}} \text{cm}^{-2}$)	@ 1.8 V	@ 2.0 V	@ 1 A cm^{-2}	@ 2 A cm^{-2}	
aPt/Mo _x C	0.06			-	3.38	6.81	1.596	1.691	This work
aRh/Mo _x C	0.04			-	3.18	6.66	1.614	1.715	
aPt/Mo _x C	0.02	PiperION	NiFe alloy	-	2.53	5.60	1.642	1.754	
aRh/Mo _x C	0.02			-	1.88	4.32	1.694	1.812	
Pt-Ni nanowires	0.1	NREL Gen2	Co NPs	-	0.73	1.36	1.888	-	ACS Catal., 10, 9953-9966 (2020)
Pt/C /MPL-CP	0.4	FAA-3-50	NiFeOOH	-	2.52	4.51	1.624	1.743	ACS Catal., 12, 135-145 (2022)
Pt/C /CP	1.0	FAA-3-50	CoSb ₂ O ₆	-	0.53	-	1.978	-	ACS Energy Lett., 6, 364-370 (2021)
Pt-Ni/C /CP	1.2	-	Fe ₁₀ Ni ₄₅ Co ₄₅	-	0.37	0.75	-	-	Adv. Energy Mater., 14, 2303350 (2024)
Ru/P-MoB	0.11	Sustainion X37-50	RuO ₂	1	1.22	-	1.779	-	Adv. Energy Mater., 14, 2303384 (2024)
Pt/C	0.6	DURAION	Ni ₃ Fe LDH	-	1.10	2.07	1.780	1.990	Adv. Funct. Mater., 32, 2203520 (2022)
Ru/Zn-N-C	0.1	FAA-3-PK-130	NiFe-LDH	-	0.09	0.42	-	-	Adv. Mater., 36, 2308798 (2024)
Pt/C	0.8	Sustainion X37-50	Nei-Ir ₁ /CoGaO OH	0.244	0.46	0.61	2.110	2.700	Angew. Chem. Int. Ed., 63, e202404418 (2024)
Pt/C	1.0	Sustainion X37-50	CuCo-oxide	-	1.36	-	1.745	1.875	Appl. Catal. B-Environ., 278, 119276 (2020)
Pt/C	1.0	Sustainion X37-50	CoFeCe _{0.5}	-	2.15	-	1.657	1.783	Appl. Catal. B-Environ., 318, 121824 (2022)
Pt/C	1.0	Sustainion X37-50	Ni _{0.5} Co _{0.5} MoO ₄ ·nH ₂ O	-	0.95	1.85	1.810	2.034	Appl. Catal. B-Environ., 328, 123504 (2023)
aPt/pNi-NOMC	0.5	Sustainion X37-50	Co ₃ O ₄	-	0.62	-	1.912	-	Appl. Catal. B-Environ., 343, 123568 (2024)
Ru ₂ P nanofiber	1.0	Sustainion X37-	IrO ₂	No mention	0.97	1.64	1.805	2.120	Chem. Eng. J., 420, 130491 (2021)
Pt/C	0.6	PBPA AEM	IrO ₂	1.0	2.00	4.00	1.691	1.800	Chem. Eng. J., 467, 143442 (2023)
Pt/C	0.4	QPC-TMA	IrO ₂	2.0	2.55	4.45	1.622	1.738	Energy Environ. Sci., 13, 3633 (2020)
Pt/C	0.5	PFTP-13	IrO ₂	2.0	3.89	7.68	1.602	1.679	Energy Environ. Sci., 14, 6338 (2021)

Membrane electrode assembly (MEA)					Current density (A cm ⁻²)		Cell voltage (V _{cell})		Reference
Cathode	NM loading (mg _{NM} cm ⁻²)	Membrane	Anode	NM loading (mg _{NM} cm ⁻²)	@ 1.8 V	@ 2.0 V	@ 1 A cm ⁻²	@ 2 A cm ⁻²	
aPt/Mo _x C	0.06	PiperION	NiFe alloy	-	3.38	6.81	1.596	1.691	This work
aRh/Mo _x C	0.04			-	3.18	6.66	1.614	1.715	
Pt/C	3.0	Sustainion X37-50	NiCoFe-NDA	-	0.33	0.54	-	-	Energy Environ. Sci., 14, 6546 (2021)
Pt/C	1.0	Sustainion X37-50	La ₂ NiO ₄ @Ni-Fe	-	0.45	0.80	2.100	-	Energy Environ. Sci., 16, 3331 (2023)
Pt-MoAl _{1-x} B/C	0.027	Sustainion X37-50	RuO ₂	5.0	0.38	1.00	2.000	2.356	Energy Environ. Sci., 16, 4093 (2023)
PtRu/C	0.5	PDTP	FeNiCo LDH /HPCC	-	4.07	10.29	1.648	1.708	Energy Environ. Sci., 16, 5019 (2023)
NA-Ru ₃ Ni/C	0.01344	Sustainion X37-50	NA-Ru ₃ Ni/C	0.01344	0.47	0.90	2.048	2.430	Energy Environ. Sci., 16, 285 (2023)
Ru ₁ -Mo ₂ C	0.013	Sustainion X37-50	NiFe LDH	-	0.88	1.82	1.830	2.030	Energy Environ. Sci., 17, 1397 (2024)
Pt-AC/Cr-N-C	0.05	Sustainion X37-50	NiFe LDH	-	0.65	1.32	1.908	2.177	J. Am. Chem. Soc., 145, 21432 (2023)
Ir-Ni/Mo ₃ Ne	0.1	Sustainion X37-50	Ir-Ni/Mo ₃ Ne	0.1	1.10	2.10	1.777	1.980	J. Colloid Interf. Sci., 628, 306 (2022)
Pt/C	1.0	Sustainion X37-50	Cu-Co oxide	-	1.30	-	1.747	-	J. Mater. Chem. A, 8, 4290 (2020)
PtRu/C	1.5	Sustainion X37-50	W/FeNiOOH/C	-	4.84	7.87	1.540	1.615	Joule, 7, 1902 (2023)
Pt/C	1.0	Tokuyama A901	CoFe _{0.25} Al _{1.75} O ₄ /KB	-	0.63	-	1.958	-	Nat. Catal., 2, 763 (2019)
Pt/C	0.1	AF2HLF 8-25X	Li ₂ Mn _{1-x} Ru _x O ₃	0.246	0.75	1.59	1.856	2.118	Nat. Catal., 7, 546 (2024)
Pt ₁ /CoHPO/KB	0.0114	Alklymer	Pt ₁ /CoHPO/KB	0.0171	0.99	-	1.801	1.930	Nat. Commun., 13, 3822 (2022)
Cl-Pt/NiFe-LDH	0.01	Sustainion X37-50	NiFe-LDN	-	0.74	1.51	1.874	2.103	Nat. Commun., 13, 6875 (2022)
PtRu/C	1.0	MTCP-50	NiFe	-	5.40	9.21	1.510	1.583	Nat. Commun., 14, 2732 (2023)
Pt-Ru/RuO ₂	0.5	AEMION	NiFe-LDH	-	0.49	1.61	1.900	2.074	Nat. Commun., 15, 1447 (2024)
PtRu/C	3.0	HTMA-DAPP	NiFe	-	5.12	-	1.580	1.639	Nat. Energy 5, 378 (2020)
Ru SS /FeNiPi PHSs	0.081	Sustainion X37-50	Ru SS /FeNiPi PHSs	0.081	2.09	-	1.640	1.780	Nat. Synth. 3, 576 (2023)

Captions for Supplementary Movies

Movie S1 0.5 ns trajectory of 13 atoms of Pt cluster on α -MoC (100) at 300 K.

Movie S2 0.5 ns trajectory of 13 atoms of Pt cluster on graphite at 300 K.

Movie S3 0.5 ns trajectory of 13 atoms of Pt cluster on α -MoC (100) at 1,300 K.

Movie S4 0.5 ns trajectory of 13 atoms of Pt cluster on graphite at 1,300 K.

Supplementary References

- 1 S. Hu and W.-X. Li, *Science*, 2021, **374**, 1360-1365.
- 2 S. Kim, J. Park, J. Hwang and J. Lee, *EnergyChem*, 2021, **3**, 100054.
- 3 T. W. Hansen, A. T. DeLaRiva, S. R. Challa and A. K. Datye, *Acc. Chem. Res.*, 2013, **46**, 1720-1730.
- 4 P. Buffat and J. P. Borel, *Phys. Rev. A*, 1976, **13**, 2287.
- 5 S. Kim, C. Choi, J. Hwang, J. Park, J. Jeong, H. Jun, S. Lee, S.-K. Kim, J. H. Jang and Y. Jung, *ACS Nano*, 2020, **14**, 4988-4999.
- 6 J. Jones, H. Xiong, A. T. DeLaRiva, E. J. Peterson, H. Pham, S. R. Challa, G. Qi, S. Oh, M. H. Wiebenga, X. I. Pereira Hernandez, Y. Wang and A. K. Datye, *Science*, 2016, **353**, 150-154.
- 7 Z. Zhuang, Y. Li, R. Yu, L. Xia, J. Yang, Z. Lang, J. Zhu, J. Huang, J. Wang, Y. Wang, L. Fan, J. Wu, Y. Zhao, D. Wang and Y. Li, *Nat. Catal.*, 2022, **5**, 300-310.
- 8 R. Sellin, J.-M. Clacens and C. Coutanceau, *Carbon*, 2010, **48**, 2244-2254.
- 9 K. A. Cychosz, R. Guillet-Nicolas, J. Garcia-Martinez and M. Thommes, *Chem. Soc. Rev.*, 2017, **46**, 389-414.
- 10 L. A. Solovyov, *Chem. Soc. Rev.*, 2013, **42**, 3708-3720.
- 11 K. T. Jung, W. B. Kim, C. H. Rhee and J. S. Lee, *Chem. Mater.*, 2004, **16**, 307-314.
- 12 A. Zitolo, V. Goellner, V. Armel, M.-T. Sougrati, T. Mineva, L. Stievano, E. Fonda and F. Jaouen, *Nat. Mater.*, 2015, **14**, 937-942.
- 13 P. Kuang, Y. Wang, B. Zhu, F. Xia, C. W. Tung, J. Wu, H. M. Chen and J. Yu, *Adv. Mater.*, 2021, **33**, e2008599.
- 14 Z. Zhang, J. Liu, J. Wang, Q. Wang, Y. Wang, K. Wang, Z. Wang, M. Gu, Z. Tang and J. Lim, *Nat. Commun.*, 2021, **12**, 5235.
- 15 P. J. Dietrich, R. J. Lobo-Lapidus, T. Wu, A. Sumer, M. C. Akatay, B. R. Fingland, N. Guo, J. A. Dumesic, C. L. Marshall and E. Stach, *Top. Catal.*, 2012, **55**, 53-69.
- 16 S. Alayoglu, P. Zavalij, B. Eichhorn, Q. Wang, A. I. Frenkel and P. Chupas, *ACS Nano*, 2009, **3**, 3127-3137.
- 17 H. Funke, A. Scheinost and M. Chukalina, *Phys. Rev. B*, 2005, **71**, 094110.
- 18 D. Koningsberger, J. Martens, R. Prins, D. Short and D. Sayers, *J. Phys. Chem.*, 1986, **90**, 3047-3050.
- 19 F. Duivenvoorden, D. Koningsberger, Y. Uh and B. Gates, *J. Am. Chem. Soc.*, 1986, **108**, 6254-6262.
- 20 S. Yang, J. Kim, Y. J. Tak, A. Soon and H. Lee, *Angew. Chem. Int. Ed.*, 2016, **55**, 2058-2062.
- 21 S. K. Sahoo, Y. Ye, S. Lee, J. Park, H. Lee, J. Lee and J. W. Han, *ACS Energy Lett.*, 2018, **4**, 126-132.
- 22 P. Rheinländer, S. Henning, J. Herranz and H. A. Gasteiger, *ECS Trans.*, 2013, **50**, 2163.
- 23 M. R. Hibbs, M. A. Hickner, T. M. Alam, S. K. McIntyre, C. H. Fujimoto and C. J. Cornelius, *Chem. Mater.*, 2008, **20**, 2566-2573.
- 24 W. E. Mustain, M. Chatenet, M. Page and Y. S. Kim, *Energy Environ. Sci.*, 2020, **13**, 2805-2838.
- 25 M. S. Cha, J. E. Park, S. Kim, S.-H. Han, S.-H. Shin, S. H. Yang, T.-H. Kim, D. M. Yu, S. So and Y. T. Hong, *Energy Environ. Sci.*, 2020, **13**, 3633-3645.
- 26 J. Hyun and H.-T. Kim, *Energy Environ. Sci.*, 2023, **16**, 5633-5662.
- 27 J. Xu and J. T. Yates Jr, *J. Chem. Phys.*, 1993, **99**, 725-732.
- 28 R. Subbaraman, D. Tripkovic, K. C. Chang, D. Strmcnik, A. P. Paulikas, P. Hirunsit, M. Chan, J. Greeley, V. Stamenkovic and N. M. Markovic, *Nat. Mater.*, 2012, **11**, 550-557.
- 29 A. F. Guillermet, J. Häglund and G. Grimvall, *Phys. Rev. B*, 1992, **45**, 11557.
- 30 G. Henkelman, A. Arnaldsson and H. Jónsson, *Comput. Mater. Sci.*, 2006, **36**, 354-360.
- 31 J.-L. Tsai and J.-F. Tu, *Mater. Des.*, 2010, **31**, 194-199.